Alma Mater Studiorum – Università di Bologna

DOTTORATO DI RICERCA IN

CHIMICA

Ciclo XXVII

Settore Concorsuale di afferenza: 03/C1

Settore Scientifico disciplinare: CHIM/06

TAILORING, SYNTHESIS AND STRUCTURE-PROPERTY RELATIONSHIPS OF 2,3-THIENOIMIDE BASED MOLECULAR MATERIALS

Presentata da: **Margherita Durso**

Coordinatore Dottorato

Prof. Aldo Roda

Relatore

Prof. Marco Bandini

Correlatore

Dott. Manuela Melucci

Esame finale anno 2015

“Most ‘impossible’ materials that one can imagine
seem impossible because they have not been made,
not because there is a sound theoretical reason
that they cannot be made”

G. M. Whitesides

Contents

List of acronyms, abbreviations and symbols

AcOH	Acetic acid
Bu	Butyl
CV	Cyclic Voltammetry
D-A	Donor-Acceptor
DFT	Density Functional Theory
DPPA	Diphenyl Phosphoryl Azide
DSC	Differential Scanning Calorimetry
EDG	Electron Donating Group
EL	Electroluminescence
EQE	External Quantum Efficiency
EWG	Electron Withdrawing Group
FMO	Frontier Molecular Orbital
I_{DS}	Source-Drain Current
$I_{ON/OFF}$	Current on/off ratio
i-PrOH	*i*-Propanol
ITO	Indium Tin Oxide
LC	Liquid Crystal
LCW	Litographically Controlled Wetting
LDA	Lithium diisopropylamide
LSCM	Laser Confocal Scanning Microscopy
M.p.	Melting point
MS	Mass Spectrometry
MW	Microwave
NBS	N-Bromosuccinimide
n-BuLi	*n*-Butyllithium
NMR	Nuclear Magnetic Resonance
NDI	Naphthalene Diimide
OFET	Organic Field-Effect Transistor
OLED	Organic Light Emitting Diode
OLET	Organic Light Emitting Transistor
OPV	Organic Photovoltaic
OSC	Organic Semiconductor
PDI	Perylene Diimide
pivOH	Pivalic acid
PL	Photoluminescence
PMMA	Poly(methyl methacrylate)
POM	Polarized Optical Microscopy
p-TsOH	*p*-Toluenesulfonic acid
Pyr	Pyridine
rt	Room Temperature

SCE Saturated Calomel Electrode
SM Starting Material
t-BuOH *t*-Butanol
TBI Thieno(bis)imide
TEA Triethylamine
TFA Trifluoroacetic acid
THF Tetrahydrofuran
TI Thienoimide
TM Target Material
TMEDA Tetramethylethylenediamine
TPD thieno[3,4-c]pyrrole-4,6-dione
TTI Time-Temperature Integrator
V_{GS} Gate Voltage
V_{DS} Drain-Source Voltage
V_T Threshold Voltage
XRD X-Ray Diffraction

μ_h Hole mobility
μ_e Electron mobility

Chapter 1

Introduction

Organic π-conjugated materials are subject of intense research from both academia and industry for their crucial role as key components of next generation electronic devices such as displays, thin-film transistors, solar cells, sensors, and flexible logic circuits (figure 1).[1] The increasing interest for organic materials assisted in the last decades, is prompted by their *intrinsic versatility* with respect to conventional inorganic ones, enabling for example the fine tailoring of their functional properties by chemical design.[2] Organic materials are in fact characterized by an extended π-conjugated core, mainly constituted by (hetero)aromatic building blocks, which can be synthesized and tailored by conventional organic reactions. Their structure can be chemically modified in order to tune and optimize their characteristic properties, like optical, electronic, morphological ones and thus their behaviour in devices. Absorption/emission and charge transport properties, as well as morphology and self-assembly capability on surfaces, are some parameters highly governable by tailoring the materials molecular structure, this giving organic chemists unprecedented degrees of flexibility in materials design.

Another advantage of organic materials with respect to inorganic ones, is represented by their *easy processability*. In fact, most inorganic based devices exploit high-purity substrates at high temperatures and generally require expensive fabrication procedures. In contrast organic materials, especially when processed from solution, allow the fabrication of devices by facile and cheap methods like ink-jet printing and spin-coating deposition. These procedures are compatible

also with cost effective roll-to-roll fabrication techniques, allowing the integration of devices on low-cost substrates such as glass, plastics, metal foils and even paper, this allowing also the development of *flexible electronics*.[3]

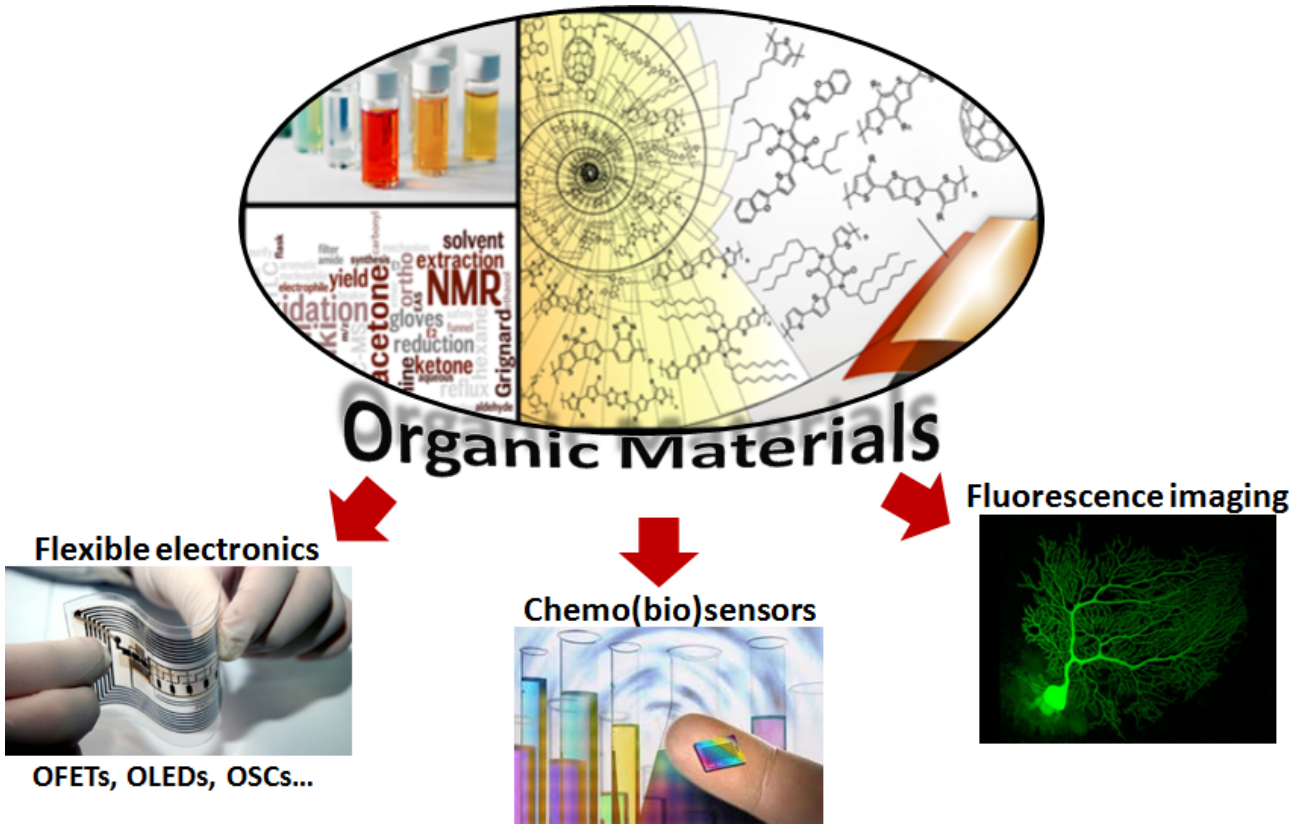

Figure 1. Chemical tailoring of organic materials enables a wide range of next-generation and cost effective devices applications.

Depending on their molecular size, organic materials can be divided into two main categories, i.e. *small molecules* and *polymers*. While polymeric materials generally exhibit higher processability and surface area properties, small molecules present the advantages of defined structures, higher control of the level of purity by exploiting conventional purification techniques, and batch to batch reproducibility. Moreover, given their exactly defined molecular structure which can be finely tailored, they constitute the ideal substrates for structure-properties relationship studies.

Both of polymeric and molecular materials have been widely studied and exploited as active layers in organic devices, ranging from light emitting diodes (OLEDs),[4] field-effect transistors (OFETs),[5] light emitting transistors (OLETs)[6] and photovoltaic cells (OPVs)[7] among the others. Some of the most known classes of π-conjugated organic materials are herein reported (molecular structures depicted in chart 1).

For example, poly(3,4-ethylenedioxythiophene) doped with poly(styrene sulphonate) (PEDOT:PSS), one of the most extensively studied conjugated polymeric systems, is a transparent conductive compound with high ductility for different applications. It is commonly exploited as electroactive material in organic transistors working as transducers for printable logic circuits, electrochromic displays and biosensors.[8]

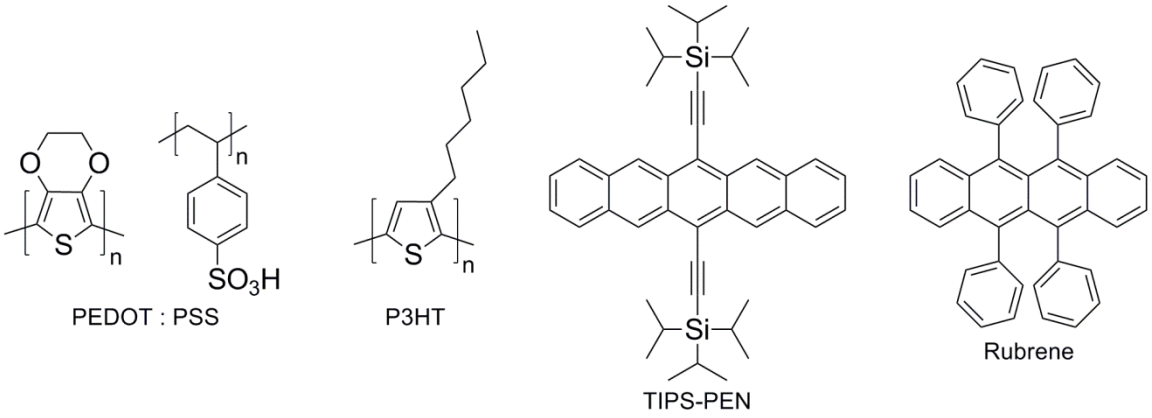

Chart 1. Some π-conjugated materials commonly used in electronic applications.

Polythiophenes, other widely investigated polymeric materials, have been regarded as the most suitable polymeric semiconductors exhibiting high charge-carrier mobilities. Among them, poly(3-hexylthiophene) (P3HT), represents a milestone, especially in OPVs field.[9] It shows excellent solubility in a variety of organic solvents, affording easy fabrication of devices by solution-processable techniques, including spin-coating, ink-jet and screen printing and it has inspired the design of new always more performant thiophene based polymers.

Among low molecular weight organic materials, acenes represent a class of molecules generally used for OFETs and OLEDs applications. Pentacene derivatives and rubrene have been extensively studied.[10] One example, reported by Bao's group, is represented by 6,13-bis(triisopropylsilylethynyl)pentacene (TIPS-PEN) showing high mobilities reached by modifying the molecular packing through a solution shearing process.[11]

These are just few examples but the organic materials field is huge and in a continuous development, since the possibilities of 'playing' with organic π-conjugated systems are nearly innumerable. Indeed, as G. Whitesides writes in his recent 'Reinventing Chemistry' essay, "*Most 'impossible' materials that one can imagine seem impossible because they have not been made, not because there is a sound theoretical reason that they cannot be made*".[12] Thus organic chemistry plays a central role, being it able of *reintroducing the idea of exploratory synthesis*[13]–the invention of new materials and processes– into the current materials science scenario, which

covers interdisciplinary skills, spanning from chemistry to physics and electronics, highly interconnected among each other.

The development of always newer structures represents therefore a great challenge for synthetic chemists to afford by molecular design and chemical tailoring innovative multifunctional materials suitable for a wide range of applications in the optoelectronic field.

In particular, this thesis work is focused on the synthesis of a class of molecular π-conjugated materials, *thienoimide* based materials, mainly used as active layers in field effect transistors and light emitting transistors.

Thus, an overview on OFET and OLET devices and on the state-of-the-art π-conjugated materials for such applications, as well as on the strategies currently available for their property engineering and synthesis is first given, before a special focus on the imide based materials scenario in literature.

1.1 Organic semiconductors, state of the art

1.1.1 Targeted applications: Organic Field Effect Transistors (OFETs) and Light Emitting Transistors (OLETs)

Basically, FETs consist in electronic devices that amplify and switch electrical signals, and metal-oxide-semiconductor FETs (MOS-FETs) based on silicon are known from more than 50 years.

The invention of the first organic field-effect transistor (OFET) in 1986 by Tsumura and co-workers[14] based on an electrochemically grown polythiophene film, claimed high interest in university and industrial research due to the potential applications in integrated circuits for a new generation of flexible, printable and low-cost electronics. To date, significant progresses have been reached in the performance of OFETs, which exploit organic semiconductors (OSCs), sometimes achieving and surpassing the one of silicon-based MOS-FETs.

Conversely, organic light emitting transistors (OLETs), allow to combine the electrical switching characteristics of OFETs with the light-emitting properties of organic light emitting diodes (OLEDs) and provide new potential device architectures for a range of applications in displays, lighting and integrated optoelectronic devices.[6] Historically, the first demonstrated OLET was described by Hepp's group in 2003: they reported a transistors made by tetracene as organic layer, fabricated on Si/SiO_2 substrates and by using with gold electrodes.[15]

A schematic of both OFET and OLET devices and working mechanism is depicted in figure 2.

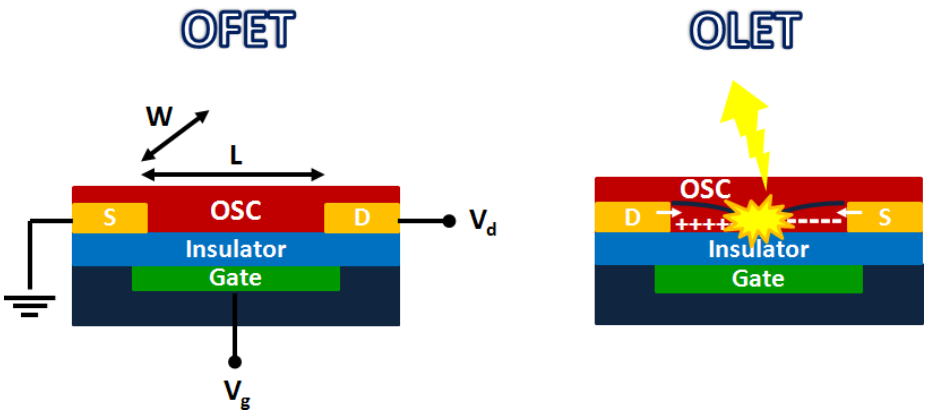

Figure 2. Scheme of generic single layer OFET (left) and (OLET) right.

A typical OFET/OLET is composed by an OSC (or by a combination of OSCs) as active layer, a dielectric layer, source-drain electrodes (S-D) of width *W* (channel width) separated by a distance *L* (channel length) and a gate electrode (figure 2).[5]

The semiconducting layer can be deposited on the substrate by different methods, i.e. vacuum sublimation, spin-coating, or drop-casting, depending on the material used and its processability. A metal or also a conducting polymer can be used as gate electrode; often gates are made of indium tin oxide (ITO). The dielectric layer usually consists in an inorganic insulator such as SiO_2 or a polymeric insulator such as poly(methylmethacrylate) (PMMA), depending on the device structure. The source and drain electrodes, which inject charges into the semiconductor, are instead high work function metals such as gold and silver. Electrodes with appropriate work functions should be selected to enable efficient electron injection into the lowest unoccupied molecular orbital (LUMO) and hole injection into the highest occupied molecular orbital (HOMO) of the OSC.

A given voltage is applied at the gate (V_G) and the drain (V_D) electrodes, while the source electrode is normally grounded (V_S=0). The potential difference between source and gate is called gate voltage (V_{GS}), while the one between source and drain is defined source-drain voltage (V_{DS}). The current flowing between source and drain electrodes (I_{DS}) is modulated by V_{GS}. With hole transporting (called also *p-type*) materials, an electric field perpendicular to the layers is induced when a voltage $V_G < 0$ is applied at the gate, and enrichment in positive charges occurs at the interface between the semiconductor and the dielectric layer as consequence (vice-versa with electron transporting semiconductors, called also *n-type* materials: V_G is > 0 and resulting enrichment in negative charges occurs). The increased charge density induces the opening of a conductive channel between source and drain, and if at the same time a voltage V_D is applied, holes (vice-versa electrons) can be transported through the channel from the source to the drain, thus recording a certain *mobility* (μ). This latter (values usually expressed in $cm^2/V{\cdot}s$) represents the capability of a semiconductor to transport holes (μ_h), electrons (μ_e), or both, and is defined as the ratio between the velocity (v) of the charges and the amplitude of the applied electric field (E):[16]

$$\mu = v/E$$

This conducting state is called “on” state and by applying a V_G below a *threshold voltage* (V_T), i.e. the minimum gate voltage required to turn the transistor on, the OFET switches to the “off” state. Excellent device performances require high charge carrier mobilities and low threshold voltages.

Another important parameter is the *current on/off ratio* (I_{ON}/I_{OFF}), i.e. the ratio between the maximum on-state current and the minimum off-state current: the greatest possible ratio is thus fundamental for a clear switching behaviour.

The output current in OFETs is measured at the drain terminal and the typical plot of I_{DS} vs. V_{DS} for a constant gate potential is called *output characteristics* (figure 3). Similarly, for a constant drain potential, I_{DS} vs. V_{GS} curve is obtained, named *transfer characteristics*. These curves constitute the two major electrical characteristics describing the behaviour of an OFET, included the measured field-effect mobility.

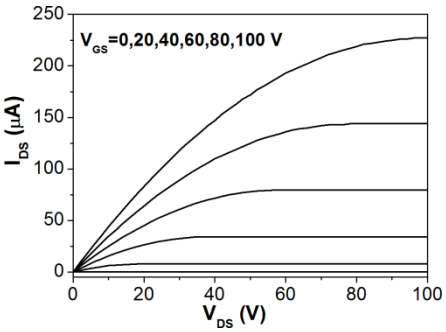

Figure 3. Example of an ideal OFET output characteristics plot.

In OLETs, by using an electroluminescent organic semiconductor, holes and electrons form excitons that recombine radiatively to generate light in the transistor channel. The optoelectronic characterization of OLETs requires the measurement of optical and electrical gate modulated characteristics, from which the external quantum efficiency (EQE, i.e. the ratio of the number of emitted photons to the number of injected charge carriers) and the brightness can be extracted.[17]

The length of each channel and thus the position of the recombination zone depends on applied V_{GS} and V_{DS}, as well as mobility ratio. Electrical characteristics (like in OFETs) allow to calculate the mobility and the on/off ratio of the device. Other informations are collected from the electroluminescence (EL) spectrum, which reveals the colour of the emitted light, and the imaging of the light emission region in the operating device, which shows the position of the recombination region as a function of the biasing conditions.

In a *unipolar* transistor (i.e. based on a p-type or a n-type material) the main drawback is represented by the photon losses in the proximity of the absorbing metal electrodes, resulting in inhibition of light emission, thus limiting the device efficiency and its brightness. On the contrary, an *ambipolar* transistor (composed of a single organic ambipolar emissive layer or a bi-layer of two unipolar semiconducting materials) allows to minimize this photon losses, since the position of the

recombination zone can be moved within the channel (far from the electrodes) by the applied gate and source-drain voltages, thus enhancing EQE and brightness of the OLET. Multilayer geometries with several function-specific layers have already been successfully developed. For example, in 2010 Capelli et al. proposed a tri-layer vertical hetero-junction OLET,[6a] reaching an EQE value of 5%, out-performing the OLED state-of-the-art based on the same emitting layer with an EQE of 2.2%.

Although these achievements in OLET devices performances, ambipolar transistors based on a single semiconductive and emissive material are more attractive, since their easy realization requires less synthetic and technological efforts, thus reducing effectively their global cost fabrication. Nevertheless, the development of materials combining excellent ambipolar charge transport properties with high electroluminescence still represents a great materials design challenge for the scientific community.

Usually molecular π-conjugated materials show unipolar behaviour in OFET devices, and the majority of experiments contributed to the general opinion that hole mobility in organic materials is consistently much common than electron mobility. Actually, organic conjugated materials could intrinsically transport both electrons and holes but unfortunately, there is a frequent lack of efficient electron transport in the channel of organic transistors.[18] This observation is mainly connected to i) a usual minor barrier for hole injection by the electrodes with respect to electron injection, ii) electron trapping at the interface between the semiconducting layer and the gate dielectric, and iii) a lower reduction potential of most conjugated molecules than that of H_2O and O_2, which react with the radical anions within the channel rendering the material environmentally unstable. For this last reason many n-channel transistors can only operate when processed and tested under inert conditions, making them technologically unattractive.

In the last years, many efforts have been made in order to overcome these drawbacks by both synthetic and technological points of view, but to date ambipolar charge transport in single layer OFETs has been achieved with just few materials .

Many small molecule materials showing a good hole transport capability in OFET devices have been synthesized. The state-of-the-art hole carrier mobilities for vacuum-deposited small molecules was achieved by 2-tridecyl[1]benzothieno[3,2-b][1]benzothiophene (C13-BTBT, chart 2) which reached 17.2 $cm^2/V{\cdot}s$ with an on/off current ratio of 10^7 and threshold voltages of about -2 V.[19] In the case of solution-processed molecules, with printed single crystals of 2,7-

dioctyl[1]benzothieno[3,2-b][1]benzothiophene (C8-BTBT, chart 2), thin-film transistors with average mobilities as high as 16.4 $cm^2/V{\cdot}s$ and a maximum value as 31.3 $cm^2/V{\cdot}s$ were achieved, with on/off current ratio of 10^5-10^7 and V_T ~10 V.[20]

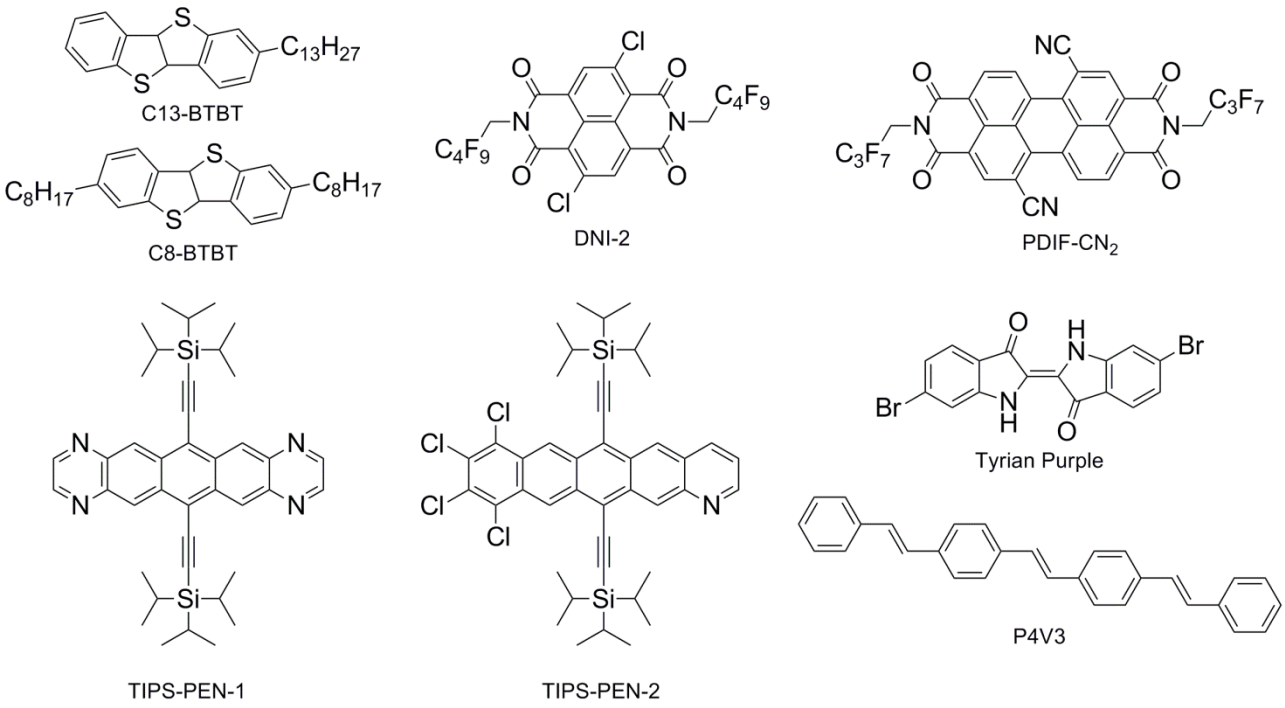

Chart 2. Organic π-conjugated semiconductors.

The development of n-type and ambipolar molecular materials based OFETs instead still lags behind.[21]

One famous class of semiconductors showing n-type behaviour is represented by rylene and other aromatic diimides like naphthalene (NDIs) and perylene diimides (PDIs), also shown in chart 2. [22] In particular, a core-chlorinated NDI compound with fluorinated side chains, DNI-2 showed a very good performances, with mobility up to 1.43 $cm^2/V{\cdot}s$ in ambient conditions, an $I_{on/off}$ as high as 10^7 and a V_T = 20 V.[23]

Also PDIs have received much attention as n-type OSCs and 1,7-dicyano PDIs among all, show air stability. One of the most successfully n-type PDI semiconductor is represented by N,N'-1H,1H-perfluorobutyl dicyanoperylenecarboxydiimide (PDIF-CN_2), which showed in single crystal OFETs mobilities of 6 $cm^2/V{\cdot}s$ in vacuum and of 3 $cm^2/V{\cdot}s$ in air with very low threshold voltages.[24]

Silylethynylated N-heteropentacenes TIPS-PEN-1[25] and TIPS-PEN-2[26] showed ambipolar behaviour. TIPS-PEN-1 displayed hole mobility of 0.22 $cm^2/V{\cdot}s$ in air and electron mobility of 1.1 $cm^2/V{\cdot}s$ in vacuum (value decreased in ambient air to 10^{-3} $cm^2/V{\cdot}s$) with $I_{on/off}$ = 10^4 and V_T = -28 V,

while TIPS-PEN-2 mobilities μ_h = 0.23 $cm^2/V{\cdot}s$ and μ_e = 0.21 $cm^2/V{\cdot}s$ in inert atmosphere with threshold voltages of about 40 V. OFETs fabricated with the natural pigment Tyrian Purple (6,6'-dibromoindigo) exhibited ambipolar characteristics in vacuum, but deterioration of the n-channel performance after exposure to air.[27] In fact while the hole mobility changed from 0.22 to 0.20 $cm^2/V{\cdot}s$ passing from vacuum to ambient air, the electron mobility decreased from 0.21 to $1.5{\cdot}10^{-2}$ $cm^2/V{\cdot}s$.

A balanced ambipolar behaviour is shown in single crystal oligo(p-phenylenevinylene) (P4V3, chart 2) based OFET (μ_h = 0.12 $cm^2/V{\cdot}s$, μ_e = 0.11 $cm^2/V{\cdot}s$) and interestingly, electroluminescence was also observed in the device channel.[28] The combination of both these functionalities, i.e. charge transport and electroluminescence in the solid state, can enable the fabrication of single layer OLETs. Since usually these two properties exclude each other,[29] only very few molecular materials allowing the fabrication of single layer OLETs have been reported up to now and they are depicted in chart 3.

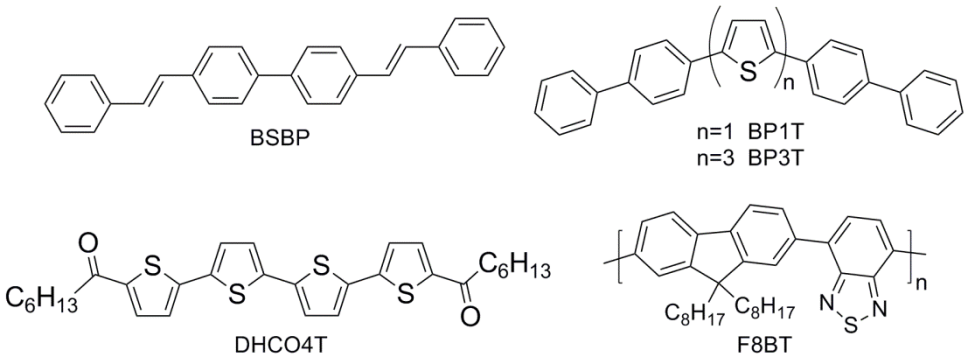

Chart 3. Ambipolar and electroluminescent materials.

An OLET device fabricated on 4,-4'-bis(styryl)biphenyl (BSBP)[30] showed mobilities of μ_h = $1.5{\cdot}10^{-3}$ $cm^2/V{\cdot}s$ and μ_e = $2.5{\cdot}10^{-5}$ $cm^2/V{\cdot}s$ in vacuum and EL with a modest external quantum efficiency (EQE) of 0.5%. Phenyl-thiophene co-oligomers like 2,5-bis(4-biphenylyl)thiophene (BP1T)[31] and α,ω-bis(biphenyl-4-yl)-terthiophene (BP3T)[32] also displayed these features in OLETs: in particular a device based on BP3T showed mobilities of μ_h = $9.13{\cdot}10^{-3}$ $cm^2/V{\cdot}s$ and μ_e = $2.94{\cdot}10^{-2}$ $cm^2/V{\cdot}s$ in vacuum with a gate-controlled light emission, but a high source-drain voltage was required (V_{DS}= -200 V).

Another example is described by α,ω-dihexylcarbonylquaterthiophene (DHCO4T)[33]: although it displayed ambipolarity and EL, unfortunately the performance of devices exploiting DHCO4T strongly depend on the dielectric-organic interface, thus affecting and limiting their work.

To date, the state-of-the-art for OLETs, is reported by Sirringhaus' group which obtained the highest performance by using a polymer. Poly(9,9-dioctylfluorenealt-benzothiadiazole) (F8BT), showed balanced electron and hole mobilities, and emitting capability which achieved external quantum efficiencies >8% and luminance efficiencies >28 $cd \cdot A^{-1}$.[34]

1.1.2 Design, synthesis and structure-properties relationships of molecular OSCs

Even if it's nearly impossible to exactly predict the charge transport properties of molecular semiconductors from their molecular structure, many efforts in chemical design are oriented to optimize their performances in OFET/OLET devices.

When a molecular semiconductor is designed, several parameters must be taken into account.[2a,5c]

In fact, optoelectronic and electrical properties of materials highly depend on π-conjugation extent, molecular packing at the solid state, film morphology and interfacial properties among the others.

In detail, for a good charge carriers injection, tuning organic semiconductor *frontier molecular orbitals* (FMOs) HOMO and LUMO levels, which need to match with the electrode work function, is essential for improving the device performance.

After charge injection, charge carriers migrate via intermolecular hopping between the molecules, so a highly ordered molecular *packing* at the solid state plays an important role too.

Four packing modes in organic crystals exist: 1) herringbone packing (face-to-edge) without π-π overlap (face-to-face) between adjacent molecules (figure 4a); 2) herringbone packing with π-π overlap between adjacent molecules, sometimes called slipped π-stacking (figure 4b); 3) lamellar packing, one-dimension (1-D) π-stacking (figure 4c); 4) lamellar packing, two-dimension (2-D) π-stacking (figure 4d). The most efficient packing for charge transport is the lamellar 2-D π-stacking, since it can transport the charge carriers through an almost straight line.

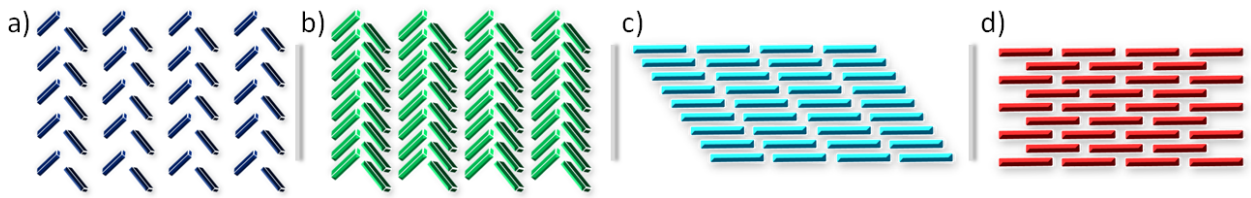

Figure 4. Packing modes in organic crystals.

Moreover, since the mobility in an organic semiconductor reflects the efficiency of charge transport within the molecule and from one molecule to another, it's intimately related to the electron cloud of the single molecule itself and the cloud splitting with its neighbour molecules.

The semiconductor *crystal structure* and *morphology* at the interface with the dielectric layer represent other parameters influencing the charge transport capability of the materials in the device. It is well-known that the existence of grain boundaries and defects in the organic active layer deteriorates the electrical performance as a result of the lowering of mobility. Moreover, OFETs based on single crystals instead of polycrystalline or amorphous materials provide higher charge mobilities, however obtaining a single crystal structure is not possible with any kind of material. A high purity level of materials also needs to be achieved, since impurities can trap charge-carriers and thus lower the OFET performance. Moreover, materials stability in the device can be improved by tuning their FMOs levels. Finally, a solution-based processing technology would offer the major advantage for application of molecular materials in low-cost and large area electronics. However, alkylation of the conjugated material, a common strategy to enhance solubility, can influence the molecular packing.

Taken into account all of these points, the design of novel molecular OSCs result a not trivial aspect in the development of novel organic based electronic devices.

As described in Bao's perspective,[2a] molecular OSCs can be divided into four parts, each of them responsible of defined properties and thus of great importance in the design and synthesis of semiconducting materials (figure 5): i) the conjugated backbone, i.e. the *core*, determines electronic properties such as energy level and bandgap, inter/intramolecular interaction, and it influences the molecular packing; ii) *heteroatoms* on the core tune electronic properties, solubility and packing; iii) *substituents* also modifies electronic properties, solubility and molecular arrangements; iv) *side chains* are usually introduced to improve solubility, even if they change the molecular packing and conformation of the core too.

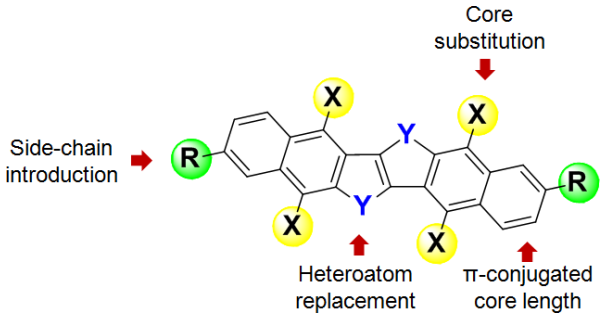

Figure 5. Generic π-conjugated molecular OSC.

For example, theoretical field-effect mobilities of acenes increase with the number of benzene rings. The corresponding experimental results showed good agreement with theoretical calculations, confirming that conjugation extension in small molecules is one viable approach to improve charge mobility in linear acenes. The combination of benzene and heteroaromatic rings allows to maintain the good electrical properties of acenes and to improve their stability as well: the successful demonstration of benzothienoacenes which can achieve high charge mobilities is a good example. Heteroatom replacement in fact constitutes an important change in a conjugated backbone, and imposes a big influence on electronic structure and crystal packing of the molecule.

A common approach followed to increase the electron affinity of a material and thus to enhance its environmentally stability trying to improve electron (and ambipolar) charge transport in OFET devices, is the insertion of electron withdrawing groups (EWGs) into the π-conjugated backbone. Halogens (fluorine atoms in particular), cyano and imide groups constitute the most popular EWGs introduced with the aim of lowering the LUMO energy levels and achieve n-type OFETs.

Moreover, since the extent of conjugation decreases the solubility of small molecule materials in organic solvents, side chains are commonly introduced to prevent this drawback. Even if they don't contribute directly to charge transport (they are insulators), they present a considerable effect on it since they influence molecular packing and thin film morphology in solid state. Side chains introduction improves also environmental stability and prevents dimerization of the molecules. Of course bulky and branched chains tend to disturb crystal packing, leading to a more amorphous solid state morphology and thus reducing the resulting charge mobility.
Only the careful rationalization of all of these parameters, considering also their mutual influence, can establish the rules of a successful new molecular materials design.

π-conjugated organic materials are conventionally synthesized by Pd catalyzed *cross-coupling* reactions, in particular Stille and Suzuki cross-couplings (figure 6).[35]
Stille reaction, a Pd(0)-catalyzed coupling between an organostannane and a haogen (or triflate)-derivative to form a new C-C bond, is widely used in organic materials synthesis since the precursor organotin compounds i) tolerate a wide variety of functional groups, ii) are not sensitive to oxygen unlike other reactive organometallic compounds, and iii) are easily prepared, isolated, and stored.

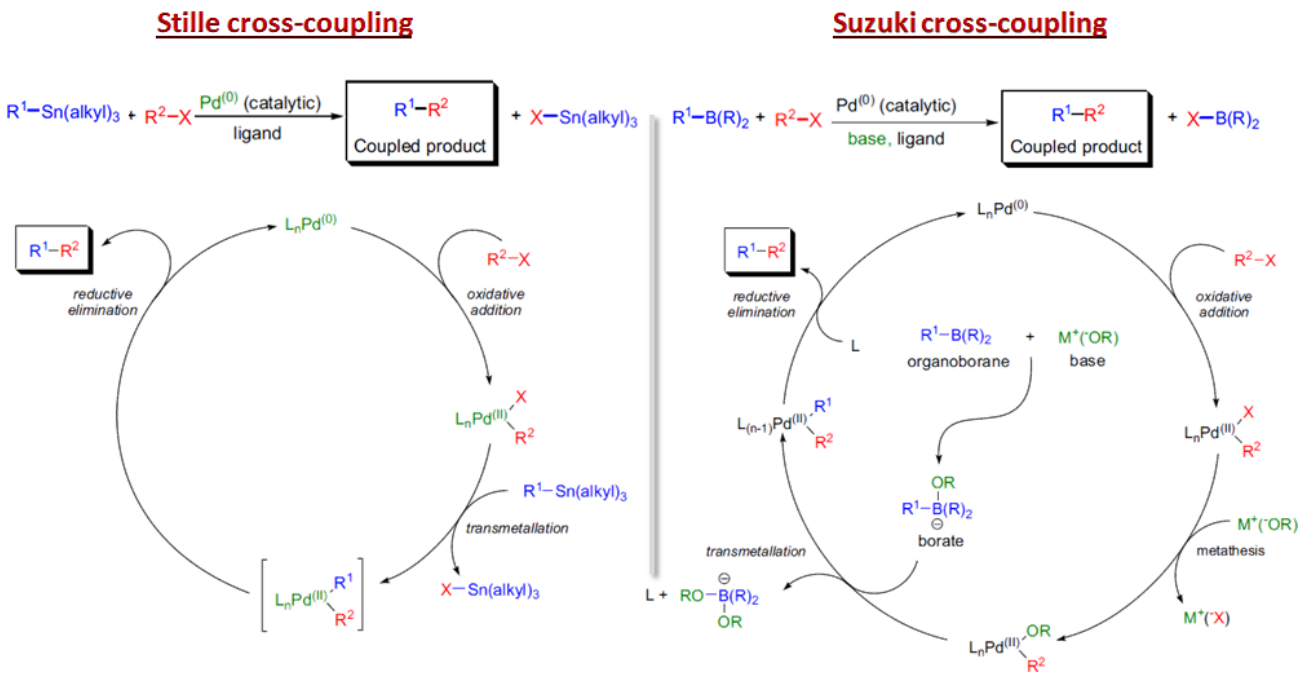

Figure 6. Generic Stille and Suzuki cross-coupling reactions with relative mechanisms (X=halogen/triflate; R^1,R^2=aryl/alkenyl; R=OH/O-alkyl).

The main disadvantages in the use of stannilated reagents are their toxicity and the difficulty to remove traces of tin by-products from the reaction mixture.

Conversely, Suzuki reaction affords the formation of C-C bonds by exploiting a palladium-catalyzed cross-coupling between organoboron compounds and organic halides or triflates in the presence of a base. The advantages of using this method are the mild reaction conditions, the commercial availability of many boronic acids and the easy removal of inorganic by-products from the reaction mixture among the others.

Nevertheless, undesired by-products such as self-coupling derivatives are often formed, and usually the reaction needs a huge excess of the organoboron derivative.

In the synthesis of organic materials, these procedures suffer from the presence of stoichiometric amount of metal waste and by-products deriving from side-reactions like metal-halogen exchange, difficult to remove completely from the target materials. Also traces of impurities can be detrimental for the performance of devices which needs a high level of materials purity.

Thus generally, the material undergoes time demanding and expensive post-synthetic purifications (i.e. repeated crystallizations and vacuum sublimations) before being tested into the electronic device. For this reason the use of a cleaner synthetic procedure could avoid these tedious extra-steps.

On this view, one alternative approach to achieve high purity level materials is based on the use of *direct arylation* reactions,[36] instead of the traditional cross-coupling protocols (scheme 1). In direct arylations, unfunctionalized (hetero)arenes are employed directly and coupled (exploiting the C-H bond activation) with pseudohalides substituted arenes, thus without the need of stoichiometric organometallic reagents.

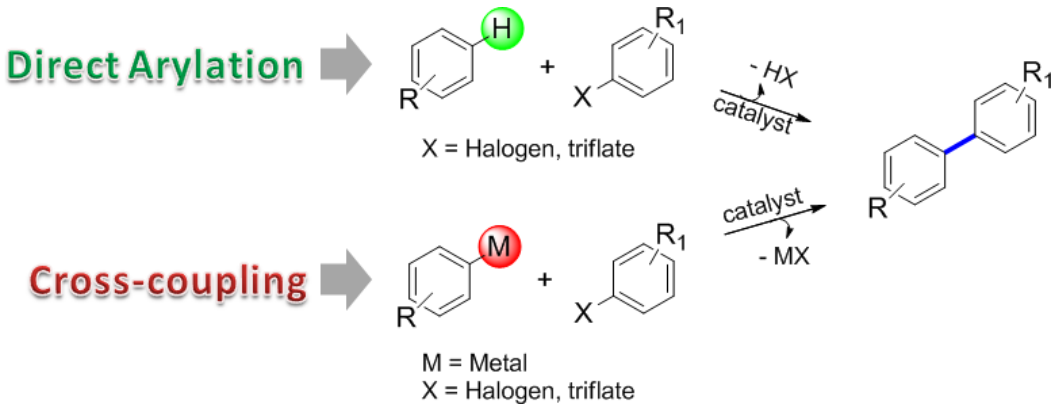

Scheme 1. Generic scheme comparing direct arylation and cross-coupling reactions.

An example of direct arylation in the field of organic materials science has been reported by Leclerc's group.[37] A thieno[3,4-c]pyrrole-4,6-dione based polymer with excellent performance in both solar cells and field-effect transistors was prepared by heteroarylation polycondensation by using phosphine based Pd(0) catalysts.

Moreover, Fagnou et al. applied the direct arylation for the synthesis of several aryl and heteroaryl small molecules (mainly dimers and trimers) useful as building blocks of functional molecular organic materials.[38]

Compounds depicted in chart 4 represent some examples of molecules successfully prepared in yields ranging from 52 to 99% by using a Pd(0) catalyst, an excess of K_2CO_3 as base and a sub-stoichiometric amount of pivalic acid (pivOH) as proton shuttle, which promotes the cleavage of the C-H bond.

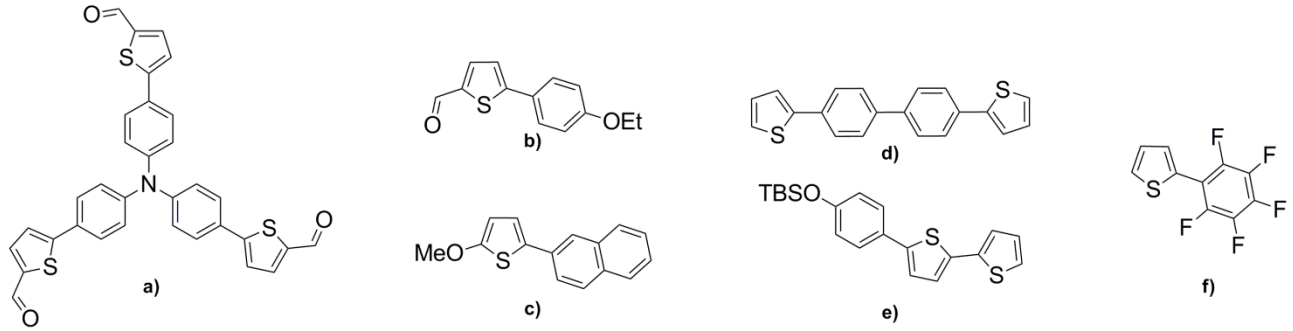

Chart 4. Some of the compounds synthesized by Fagnou's group under their developed direct arylation conditions.

Shortly after, Kappe's group demonstrated the compatibility of Fagnou's protocol with MW-assisted synthesis and enhanced the reactivity of poor reactive substrates, like pyridine and nitrobenzene derivatives.[39]

1.2 Thesis starting point: the case of NT4N

Aromatic imides constitute a widely exploited electron-withdrawing building block in both small molecules and polymers for enhancing their electron affinity, electron mobility and ambient stability, and materials bearing imide-based moieties are commonly used for applications in OFET devices as well as organic photovoltaic.[22a] Examples of materials characterized by an imide-based building block are depicted in chart 5.

A reported series of alternating donor-acceptor (D-A) copolymers based on naphthalene diimide (NDI) acceptor and thiophene donor moieties have been realized and used in n-type and ambipolar OFETs.[40] Maintaining the LUMO levels constant due to the NDI moiety, the HOMO levels were instead varied by the incorporation of different electron-donating thiophene based comonomers, this resulting in transition from n-type to ambipolar charge transport.

Moreover, the insertion of imide-bridged bithiophene units (BTIs) has emerged as a powerful tool to obtain electron and ambipolar transporting polythiophenes,[41] while a family of linear fused molecular dithieno[2,3-b:3'2'-d]-thiophene diimides (DTTDIs)[42] has been reported as potential n-channel organic semiconductors, showing low-laying LUMO energy levels and close intermolecular packing distance.

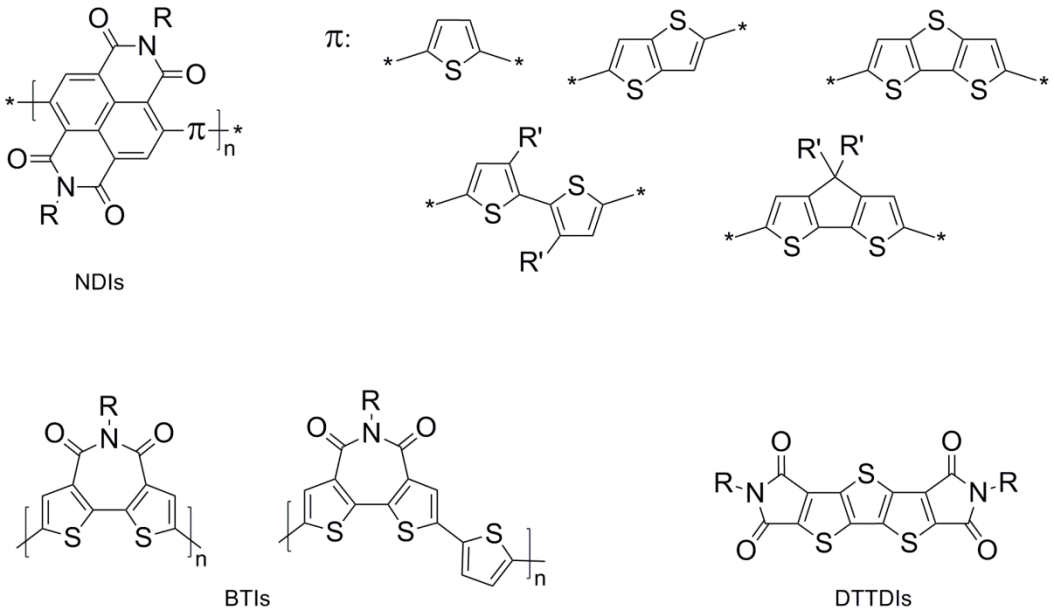

Chart 5. Molecular structures of NDI, BTI and DTTDI based molecular and polymeric materials.

In this framework, the imide based building block thieno[3,4-c]pyrrole-4,6-dione (TPD, chart 6), usually receiving much attention in low band gap D-A copolymers for organic photovoltaic

devices,[43] has been recently introduced into thiophene based polymers for OFET applications.[44] The presence of the TPD unit lowers the HOMO energy levels, leading to an enhanced device storage stability of the resulting copolymers, which exhibited also good processability and p-type or ambipolar charge transport capability (depending on the thiophene based comonomer).

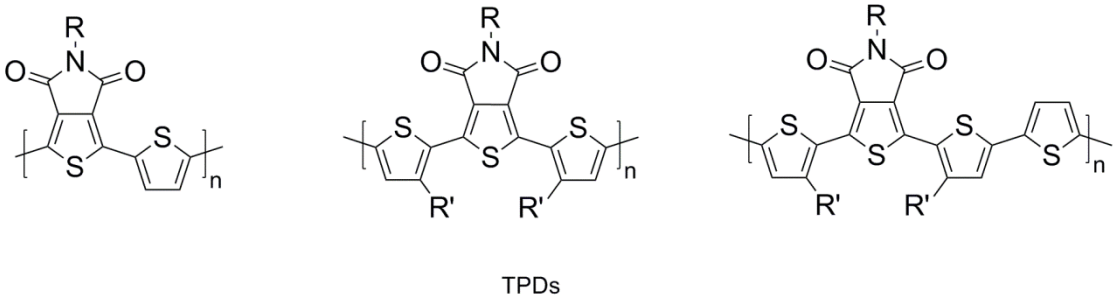

Chart 6. Generic molecular structures of some TPD polymeric materials.

Several reasons make the thieno[3,4-c]pyrrole-4,6-dione (TPD) building block attractive in the field of materials semiconductors: when incorporated into conjugated polymers, its symmetric and coplanar structure provides interactions along and between the polymer chains and its strong electron withdrawing effect lowers HOMO and LUMO energy levels, a desired property for increasing stability and n-type charge transport respectively. Furthermore, TPD and its derivative building blocks can be easily prepared from the commercially available thiophene-3,4-dicarboxylic acidin few synthetic steps replacing old longer protocols.[45]

Although the wide interest for this moiety bearing an imide group on C3 and C4 positions of the thiophene ring (from which the name *3,4-thienoimide*, or 3,4-TI) in the field of organic materials, on the contrary its regioisomeric form, *2,3-thienoimide* (2,3-TI, figure 7), was never synthesized or reported in literature.

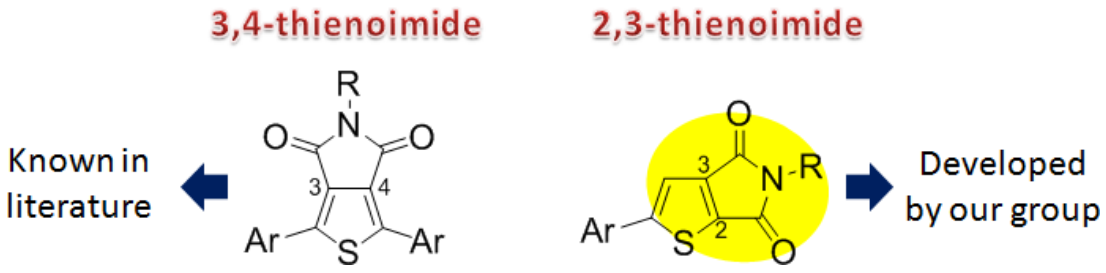

Figure 7. Molecular structures of isomeric 3,4- and 2,3-thienoimide moieties.

The only case of an imidic group on C2 and C3 positions of the thiophene ring was reported by Zhu et al.[42] However, in their DTTDI based molecules the thienoimide does not represent a building

block, but it constitutes a part of the completely fused structure (see chart 5), thus it cannot be isolated and introduced in π-conjugated molecular or polymeric materials.

In 2011, inspired by these molecular moieties, the research group in which this thesis work has been carried out (in collaboration with ETC s.r.l., a spin-off company of CNR and Saes Getters S. p. A.), synthesized for the first time the 2,3-thienoimide building block and introduced it into a small thiophene based material.

Surprisingly, the resulting material, 2,2'-([2,2'-bithiophene]-5,5'-diyl)bis(5-butyl-4H-thieno[2,3-c]pyrrole-4,6(5H)-dione), named NT4N and depicted in figure 8, showed ambipolar behaviour with simultaneous light emission capability.[46]

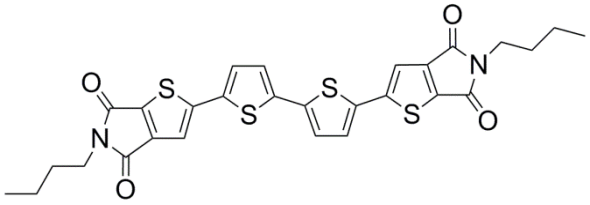

Figure 8. Chemical structure of NT4N material.

NT4N was synthesized by a series of bromination and cross-coupling reactions starting from the 2,3-thienoimide, which was prepared through a variation of the 3,4-TI known old synthetic protocol from commercial 2,3-dibromothiophene (scheme 2).

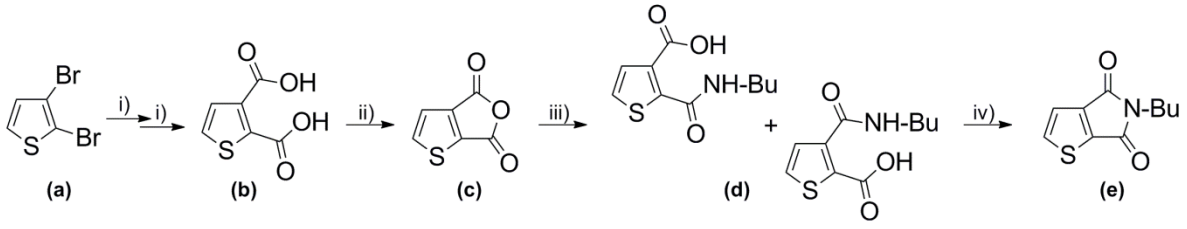

Scheme 2. Synthetic route to 2,3-TI. i) BuLi, CO_2 (gas), Et_2O. ii) Acetic anhydride, reflux. iii) Buthylamine ($BuNH_2$), toluene, reflux. iv) $SOCl_2$, reflux.

In scheme 2 is described the reported synthesis of the 2,3-TI moiety. 2,3-dibromothiophene (**a**) was first converted into its dicarboxylic acid derivative (**b**), whose dehydration with acetic anhydride led to thiophene-2,3-dicarboxylic anhydride (**c**).

A two-step procedure was then used to synthesize the TI group: after reacting with buthylamine, the anhydride was converted into a mixture of two isomeric butylcarbamoylthiophene-carboxylic acid compounds (**d**), which were finally made react with $SOCl_2$ to get the 2,3-TI building block (**e**) (overall yield 40%).

In the following scheme 3 the synthetic way to NT4N is depicted.

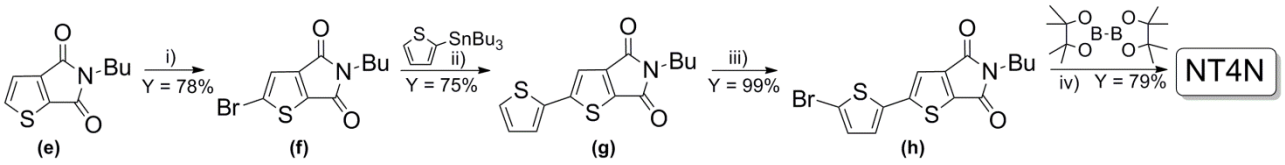

Scheme 3. Synthesis of NT4N. i) NBS, TFA/H_2SO_4. ii) Stille coupling, Pd(0) cat., toluene, reflux. iii) NBS, AcOH/CH_2Cl_2. iv) One-pot borylation/Suzuki coupling under MW assistance, $PdCl_2$dppf, THF/H_2O.

2,3-TI was initially brominated with NBS in a TFA/H_2SO_4 solvent mixture to get 2-bromo-5-butyl-4H-thieno[2,3-c]pyrrole-4,6(5H)-dione (**f**, 78% Y). Then, a Stille cross-coupling reaction with commercial tributylstannylthiophene led to the dimeric compound (**g**) in 75% yield, which was successively brominated under conventional halogenation conditions with NBS (**h**, semi-quantitative yield). Finally, microwave (MW)-assisted (P = 300 W, T = 80 °C, 10 min) high throughput, high purity borylation/Suzuki coupling followed by flash chromatography purification, provided the material NT4N in 79% yield.

A second approach, based on a Stille cross-coupling reaction between the brominated thienoimide (**f**) and commercial 5,5'-bis(tributylstannyl)-2,2'-bithiophene (scheme 4) to directly get NT4N (75% Y), was then performed for comparison. This alternative route presents the advantage of less synthetic reaction steps with comparable yields.

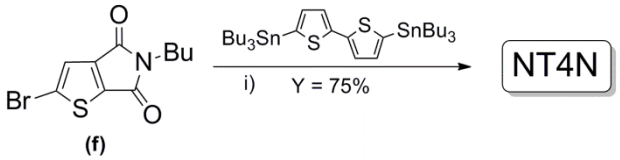

Scheme 4. Synthesis of NT4N from brominated TI (**f**) through Stille cross-coupling approach. i) Pd(0) cat., toluene, reflux.

The full chemo-physical characterization of NT4N, included the electrical one in an OFET device, was carried out in order to investigate the effect of the insertion of the 2,3-TI groups on the oligothiophene based structure.

The absorption and emission spectra of NT4N in CH_2Cl_2 solution and film (figure 9a) are similar, suggesting high molecular planarity and rigidity. The absorption maximum is located at about λ_{max}= 450 nm in solution and λ_{max}= 430 nm in film (shoulder at λ_{max}= 520 nm). They result strongly red shifted if compared to the known unipolar semiconductors dihexyl quaterthiophene (DH4T, p-type, λ_{max}= 402 nm) and diperfluorohexyl quaterthiophene (DF4T, n-type, λ_{max}= 398 nm) but close

to that of the longer dihexyl substituted sexithiophene (λ_{max}= 440 nm),[47] as a result of the higher conjugation length originated by the inclusion of the imide moieties in the conjugated system. Similarly, the emission maximum λ_{em} is located at 579 nm (λ_{exc} = 449 nm) in solution and λ_{em} = 603 nm in film, strongly red-shifted with respect to that of DH4T.[48]

Differential scanning calorimetry (DSC) analysis (10°C/min, not reported herein) showed a first endothermic peak at T= 187°C and a second one corresponding to the melting from crystal to liquid crystal at 280 °C. A single transition, corresponding to the crystallization at 272 °C, was revealed in the cooling run.

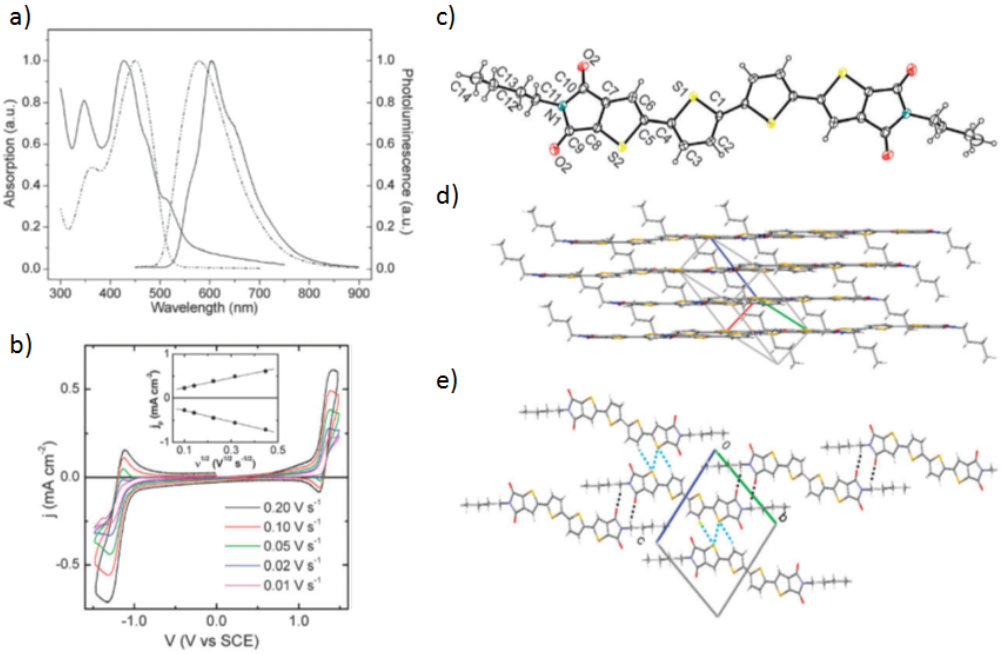

Figure 9. a) Normalized absorption and emission of NT4N solution (CH_2Cl_2, $4\cdot10^{-5}$ M, dashed line) and film (100 nm thick, solid line). b) CV curves in CH_2Cl_2 0.1 mol L^{-1} $(C_4H_9)_4NClO_4$. c) ORTEP drawing of NT4N. d) Arbitrary view of the crystal packing showing the π–π stacks. e) View along the axis of one 1D network generated by C–H···O interactions (dashed black). S···S and C–H···S contacts (light blue).

The cyclic voltammetries (CVs, figure 9b) appear quasi-reversible and symmetrical in the cathodic and anodic regions showing comparable kinetics both in reduction and oxidation. The standard potentials resulted $E°_{red}$= -1.21 V and $E°_{ox}$= 1.32 V vs. SCE, giving an electrochemical energy gap E^{elec}_g = 2.53 eV (close to the optical one E^{opt}_g =2.4 eV),[49a] a HOMO energy value of -6 eV and a LUMO one of -3.4 eV. The X-ray crystal structure of NT4N shows that the molecule lies on a crystallographic inversion center located at the midpoint of the bond between the two thiophene units (figure 9c).

The molecular backbone is almost planar and the crystal packing (figure 9d) shows that interestingly the molecules adopt a slipped π– π stacking packing mode instead of the herringbone structure usually common for oligothiophenes,[50] including the already cited DTTDI.[42]

The XRD patterns of the powder sample together with those of cast, cast-melt-quenched and vacuum sublimed films (details not reported) show several well resolved diffraction peaks confirming an important degree of crystallinity, suggesting an almost perpendicular arrangement of the molecules with respect to the substrate, as generally observed for oligothiophene semiconductors.

Electrical characterization of NT4N (figure 10) was carried out in a bottom-gate top-contact geometry OFET with gold electrodes, under a N_2 controlled atmosphere, by using as active layer a 30 nm thick film of NT4N grown by vacuum sublimation on top of a Glass/ITO/PMMA substrate. Interestingly, ambipolar behaviour was found for the realized OFET device, with an unbalanced contribution of hole and electron transport.

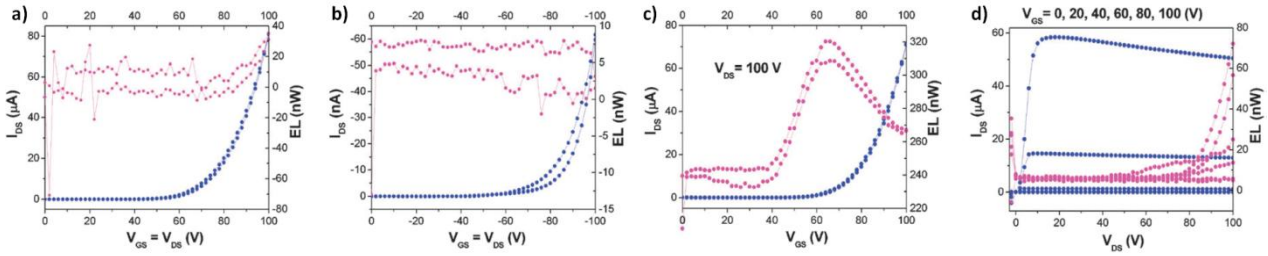

Figure 10. Electrical characteristics (blue) and corresponding light emission intensity (purple) of single layer OFET based on NT4N. (a, b) n type (a) and p-type (b) locus curves. (c) n-type transfer saturation curve, and (d) n-type multiple output curves.

A surprisingly high electron mobility value of μ_e = 0.053 $cm^2/V{\cdot}s$ (V_T^e = 60 V) has been calculated, while on the contrary, a three-order-of-magnitude lower hole mobility $\mu_h = 6.4{\cdot}10^{-5}$ $cm^2/V{\cdot}s$ (V_T^h = -71 V) has been found. Moreover, electroluminescence was also detected in the device, with the light emission signal of the transfer curve peaked in the ambipolar working region of the device, in agreement with the typical behaviour reported for single layer OLETs.

References

[1] a) A. J. Heeger, N. S. Sariciftci and E. B. Namdas, *Semiconducting and Metallic Polymers*, Oxford University Press, **2010**; b) Z. Bao and J. Locklin, *Organic Field-Effect Transistors*, CRC Press, **2007**; c) H. Klauk, *Organic Electronics: Materials, Manufacturing and Applications*, Wiley-VCH, Weinheim, Germany, **2006**; d) S. R. Forrest, *Nature* **2004**, *428*, 911-918.

[2] a) J. Mei, Y. Diao, A. L. Appleton, L. Fang and Z. Bao, *J. Am. Chem. Soc.* **2013**, *135*, 6724-6746; b) B. J. Jung, N. J. Tremblay, M.-L. Yeh and H. E. Katz, *Chem. Mater.* **2011**, *23*, 568-582; b) S. Allard, M. Forster, B. Souharce, H. Thiem and U. Scherf, *Angew. Chem. Int. Ed.* **2008**, *47*, 2-31.

[3] a) M. Berggren, D. Nilsson and N. D. Robinson, *Nature Mater.* **2007**, *6*, 3-5; b) S. R. Forrest, *Nature* **2004**, *428*, 911-918..

[4] a) J. G. C. Veinot and T. J. Marks, *Acc. Chem. Res.* **2005**, *38*, 632-643; b) S. Y. Lee, T. Yasuda, Y. S. Yang, Q. Zhang and C. Adachi, *Angew. Chem. Int. Ed.* **2014**, *53*, 6402-6046.

[5] a) H. Sirringhaus, *Adv. Mater.* **2014**, *26*, 1319-1335; b) C.-A. Di, F. Zhang and D. Zhu, *Adv. Mater.* **2013**, *25*, 313-330; c) C. Wang, H. Dong, W. Hu, Y. Liu and D. Zhu, *Chem. Rev.* **2012**, *112*, 2208-2267; d) A. R. Murphy and J.M. J. Fréchet, *Chem. Rev.* **2007**, *107*, 1066-1096..

[6] a) R. Capelli, S. Toffanin, G. Generali, H. Usta, A. Facchetti and M. Muccini, *Nat. Mater.* **2010**, *9*, 496-503; b) M. Muccini, *Nat. Mater.* **2006**, *5*, 605-613; c) J. Zaumseil and H. Sirringhaus, *Chem. Rev.* **2007**, *107*, 1296-1323; d) J. A. Misewich, R. Martel, P. Avouris, J. C. Tsang, S. Heinze and J. Tersoff, *Science*, **2003**, *300*, 783-786.

[7] a) J. Roncali, P. Leriche and P. Blanchard, *Adv. Mater.* **2014**, *26*, 3821-3838; b) A. Mishra and P. Bäuerle, *Angew. Chem. Int. Ed.* **2012**, *51*, 2020-2067; c) Z. Lu, B. Jiang, X. Zhang, A. Tang, L. Chen, C. Zhan and J. Yao, *Chem. Mater.* **2014**, *26*, 2907-2914; d) Y. Huang, E. G. Kramer, A. J. Heeger and G. C. Bazan, *Chem. Rev.* **2014**, *114*, 7006-7043.

[8] a) D. Khodagholy, J. Rivnay, M. Sessolo, M. Gurfinkel, P. Leleux, L. H. Jimison, E. Stavrinidou, T. Herve, S. Sanaur, R. M. Owens and G. G. Malliaras, *Nature Commun.* **2013**, 4 : 2133; b) D. A. Bernards, D. J. Macaya, M. Nikolou, J. A. DeFranco, S. Takamatsu and G. G. Malliaras, *J. Mater. Chem.* **2008**, *18*, 116-120; c) J. Kawahara, P. Andersson Ersmana, I. Engquist and M. Berggren, *Org. Electron.* **2012**, *13*, 469-474; d) M. Berggren, R. Forchheimer, J. Bobacka, P.-O. Svensson, D. Nilsson, O. Larsson and A. Ivaska, *PEDOT:PSS-Based Electrochemical Transistors for Ion-to-Electron Transduction and Sensor Signal Amplification*, Organic Semiconductors in Sensor Applications Springer, **2008**, *107*, 263-280; e) D. Nilsson, N. Robinson, M. Berggren and R. Forchheimer, *Adv. Mater.* **2005**, *17*, 353-358.

[9] a) H. Sirringhaus, N. Tessler and R. H. Friend, *Science* **1998**, *280*, 1741-1744; b) H. Sirringhaus, P. J. Brown, R. H. Friend, M. M. Nielsen, K. Bechgaard, B. M. W. Langeveld-Voss, A. J. H. Spierlng, R. A. J. Janssen, E. W. Meijer, P. Herwig and D. M. de Leeuw, *Nature* **1999**, *401*, 685-688; c) R. D. McCullough, S. Tristram-Nagle, S. P. Williams, R. D. Lowevt and M Jayaraman , *J. Am. Chem. Soc.* **1993**, *115*, 4910-4911; d) G. Sauvé, A. E. Javier, R. Zhang, J. Liu, S. A. Sydlik, T. Kowalewskia and R. D. McCullough, *J. Mater. Chem.* **2010**, *20*, 3195-3201.

[10] a) T. W. Kelley, D. V. Muyres, P. F. Baude, T. P. Smith and T. D. Jones, *Mater. Res. Soc. Symp. Proc.* **2003**, *771*, 169; b) V. C. Sundar, J. Zaumseil, V. Podzorov, E. Menard, R. L. Willett, T. Someya, M. E. Gershenson and J. A. Rogers, *Science* **2004**, *303*, 1644-1646.

[11] G. Giri, E. Verploegen, S. C. B. Mannsfeld, S. Atahan-Evrenk, D. H. Kim, S. Y. Lee, H. A. Becerril, A. Aspuru-Guzik, M. F. Toney and Z. Bao, *Nature* **2011**, *480*, 504-508.

[12] G. M. Whitesides, *Angew. Chem. Int. Ed.* **2015**, *54*, 2-16.

[13] G. Whitesides, *MRS Bullettin* **2002**, 56-65.

[14] A. Tsumura, H. Koezuka and T. Ando, *Appl. Phys. Lett.* **1986**, *49*, 1210-1212.

[15] A. Hepp, H. Heil, W. Weise, M. Ahles, R. Schmechel and H. von Seggern, *Phys. Rev. Lett.* **2003**, *91*, 157406.
[16] V. Coropceanu, J. Cornil, D. A. da Silva Filho, Y. Olivier, R. Silbey and J.-L. Brédas, *Chem. Rev.* **2007**, *107*, 926-952.
[17] F. Cicoira and C. Santato, *Adv. Funct. Mater.* **2007**, *17*, 3421-3434.
[18] J. Cornil, J.-L. Brédas, J. Zaumseil and H. Sirringhaus, *Adv. Mater.* **2007**, *19*, 1791-1799.
[19] A. Y. Amin, A. Khassanov, K. Reuter, T. Meyer-Friedrichsen and M. Halik, *J. Am. Chem. Soc.* **2012**, *134*, 16548-16550.
[20] H. Minemawari, T. Yamada, H. Matsui, J. Tsutsumi, S. Haas, R. Chiba, R. Kumai and T. Hasegawa, *Nature* **2011**, *475*, 364-367.
[21] a) Y. Zhao, Y. Guo and Y. Liu, *Adv. Mater.* **2013**, *25*, 5372-5391; b) J. E. Anthony, A. Facchetti, M. Heeney, S. R. Marder and X. Zhan, *Adv. Mater.* **2010**, *22*, 3876-3892.
[22] a) X. Zhan, A. Facchetti, S. Barlow, T. J. Marks, M. A. Ratner, M. R. Wasielewski and S. R. Marder, *Adv. Mater.* **2011**, *23*, 268-284; b) D. Shukla, S. F. Nelson, D. C. Freeman, M. Rajeswaran, W. G. Ahearn, D. M. Meyer and J. T. Carey, *Chem. Mater.* **2008**, *20*, 7486-7491.
[23] J. H. Oh, S. L. Suraru, W. Y. Lee, M. Konemann, H. W. Hoffken, C. Roger, R. Schmidt, Y. Chung, W. C. Chen, F. Wurthner and Z. Bao, *Adv. Funct. Mater.* **2010**, *20*, 2148-2156.
[24] A. S. Molinari, H. Alves, Z. Chen, A. Facchetti and A. F. Morpurgo, *J. Am. Chem. Soc.* **2009**, *131*, 2462-2463.
[25] Z. Liang, Q. Tang, R. Mao, D. Liu, J. Xu and Q. Miao, *Adv. Mater.* **2011**, *23*, 5514-5518.
[26] W. J. Zeng, X. Y. Pan, C. L. Song and H. L. Zhang, *Aip Advances* **2013**, *3*, 012101.
[27] E. D. Glowacki, L. Leonat, G. Voss, M. A. Bodea, Z. Bozkurt, A. M. Ramil, M. Irimia-Vladu, S. Bauer and N. S. Sariciftci, *Aip Advances* **2011**, *1*, 042132.
[28] H. Nakanotani, M. Saito, H. Nakamura and C. Adachi, *Appl. Phys. Lett.* **2009**, *95*, 033308.
[29] a) A. Dadvand, A. G. Moiseev, K. Sawabe, W.-H. Sun, B. Djukic, I. Chung, T. Takenobu, F. Rosei and D. F. Perepichka, *Angew. Chem. Int. Ed.* **2012**, *51*, 3837-3841 ; b) I. F. Perepichka, D. F. Perepichka, H. Meng and F. Wudl, *Adv. Mater.* **2005**, *17*, 2281-2305; c) M. B. Smith and J. Michl, *Chem. Rev.* **2010**, *110*, 6891-6936; e) H. Najafov, B. Lee, Q. Zhou, L. C. Feldman and V. Podzorov, *Nat. Mater.* **2010**, *9*, 938-943.
[30] T. Sakanoue, M. Yahiro, C. Adachi, H. Uchiuzou, T. Takahashi and A. Toshimitsu, *Appl. Phys. Lett.* **2007**, *90*, 171118.
[31] T. Yamao, Y. Shimizu, K. Terasaki and S. Hotta, *Adv. Mater.* **2008**, *20*, 4109–4112
[32] K. Yamane, H. Yanagi, A. Sawamoto and S. Hotta, *Appl. Phys. Lett.* **2007**, *90*, 162108.
[33] R. Capelli, F. Dinelli, S. Toffanin, F. Todescato, M. Murgia, M. Muccini, A. Facchetti and T. J. Marks, *J. Phys. Chem. C* **2008**, *112*, 12993-12999.
[34] M. C. Gwinner, D. Kabra, M. Roberts, T. J. K. Brenner, B. H. Wallikewitz, C. R. McNeill, R. H. Friend and H. Sirringhaus, *Adv. Mater.* **2012**, *24*, 2728-2734.
[35] a) D. Milstein and J. K. Stille, *J. Am. Chem. Soc.* **1979**, *101*, 4992-4998; b) E. Negishi, A. O. King and N. Okukado, *J. Org. Chem.* **1977**, *42*, 1821-1823; c) N. Miyaura, T. Yanagi, and A. Suzuki, *Synth. Commun.* **1981**, *11*, 513-519.
[36] a) L. Ackermann, R. Vicente and A. R. Kapdi, *Angew. Chem. Int. Ed.* **2009**, *48*, 9792-9826; b) A. Facchetti, L. Vaccaro and A. Marrocchi, *Angew. Chem. Int. Ed.* **2012**, *51*, 3520-3523; c) L. G. Mercier and M. Leclerc, *Acc. Chem. Res.* **2013**, *46*, 1597-1605; d) K. Okamoto, J. Zhang, J. B. Housekeeper,S. R. Marder and C. K. Luscombe, *Macromolecules* **2013**, *46*, 8059-8078.
[37] P. Berrouard, A. Najari, A. Pron, D. Gendron, P.-O. Morin, J.-R. Pouliot, J. Veilleux and M. Leclerc, *Angew. Chem. Int. Ed.* **2012**, *51*, 2078-2071.

[38] a) S. I. Gorelsky, D. Lapointe and K. Fagnou, *J. Org. Chem.* **2012**, *77*, 658-668; b) D. J. Schipper and K. Fagnou, *Chem. Mater.* **2011**, *23*, 1594-1600; c) B. Liégault, D. Lapointe, L. Caron, A. Vlassova and K. Fagnou, *J. Org. Chem.* **2009**, *74*, 1826-1834.

[39] a) M. Baghbanzadeh, C. Pilger and C. O. Kappe, *J. Org. Chem.* **2011**, *76*, 8138-8142; b) A. Sharma, D. Vacchani and E. Van der Eycken, *Chem. Eur. J.* **2013**, *19*, 1158-1168.

[40] X. Guo, F. S. Kim, M. J. Seger, S. A. Jenekhe and M. D. Watson, *Chem. Mater.* **2012**, *24*, 1434-1442.

[41] X. Guo, R. P. Ortiz, Y. Zheng, Y. Hu, Y.-Y. Noh, K.-J. Baeg, A. Facchetti and T. J. Marks, *J. Am. Chem. Soc.* **2011**, 133, 1405-1418.

[42] W. Hong, H. Yuan, H. Li, X. Yang, X. Gao and D. Zhu, Org. Lett. 2011, 6, 1410-1413.

[43] a) T.-Y. Chu, J. Lu, S. Beaupré, Y. Zhang, J.-R. Pouliot, S. Wakim, J. Zhou, M. Leclerc, Z. Li, J. Ding and Y. Tao, *J. Am. Chem. Soc.* **2011**, *133*, 4250-4253; b) G.-Y. Chen, Y.-H. Cheng, Y.-J. Chou, M.-S. Su, C.-M. Chen and K.-H. Wei, *Chem. Commun.* **2011**, *47*, 5064-5066; c) C. Piliego, T. W. Holcombe, J. D. Douglas, C. H. Woo, P.M. Beaujuge and J. M. J. Fréchet, *J. Am. Chem. Soc.* **2010**, *132*, 7595-7597.

[44] X. Guo, R. P. Ortiz, Y. Zheng, M.-G. Kim, S. Zhang, Y. Hu, G. Lu, A. Facchetti and T. J. Marks, *J. Am. Chem. Soc.* **2011**, *133*, 13685-13697.

[45] a) Y. Zou, A. Najari, P. Berrouard, S. Beaupré, B. Réda Aïch, Y. Tao and M. Leclerc, *J. Am. Chem. Soc.* **2010**, *132*, 5330-5331; b) C. B. Nielsen and T. Bjørnholm, *Org. Lett.* **2004**, *6*, 3381-3384; c) Q. Zhang and J. M. Tour, *J. Am. Chem. Soc.* **1997**, *119*, 5065-5066.

[46] a) M. Melucci, M. Zambianchi, L. Favaretto, M. Gazzano, A. Zanelli, M. Monari, R. Capelli, S. Troisi, S. Toffanin and M. Muccini, *Chem. Commun.* **2011**, *47*, 11840-11842; b) E.T.C. S.r.l., M. Melucci, L. Favaretto, M. Zambianchi, R. Capelli, M. Muccini, PATENT: WO2012156948 A1; WO2014057422 A1.

[47] A. Facchetti, M.-H. Yoon, C. L. Stern, G. R. Hutchison, M. A. Ratner and T. J. Marks, *J. Am. Chem. Soc.* **2004**, *126*, 13480-13501.

[48] M. Melucci, M. Zambianchi, A. Zanelli, N. Camaioni, M. Gazzano, A. Bongini and G. Barbarella, *ChemPhysChem* **2007**, *8*, 2621-2626.

[49] a) L. Micaroni, F. C. Nart and I. A. Hummelgen, *J. Solid State Electrochem.* **2002**, *7*, 55-59; b) C. Santato, L. Favaretto, M. Melucci, A. Zanelli, M. Gazzano, M. Monari, D. Isik, D. Banville, S. Bertolazzi, S. Loranger and F. Cicoira, *J. Mater. Chem.* **2010**, *20*, 669-676.

[50] a) A. Mishra, C.-Q. Ma and P. Baüerle, *Chem. Rev.* **2009**, *109*, 1141-1276; b) G. Barbarella, M. Melucci and G. Sotgiu, *Adv. Mater.* **2005**, *17*, 1581-1593.

Chapter 2

Aims and objectives

The aim of this work, is the development of new thienoimide based molecular materials inspired by the case of NT4N (described in chapter 1) with enhanced functionalities. Different design strategies have been planned for the fine tailoring of its molecular structure with the aim of i) investigating the structure-properties relationships in molecular materials characterized by the thienoimide moiety, ii) tuning optical, packing, morphology, charge transport and electroluminescence properties, iii) optimizing the performances in device and iv) investigating and enabling new applications.

The design strategies tested for the fine tailoring of NT4N molecular structure and discussed in the following chapter 3 are schematized in figure 11 and here introduced.

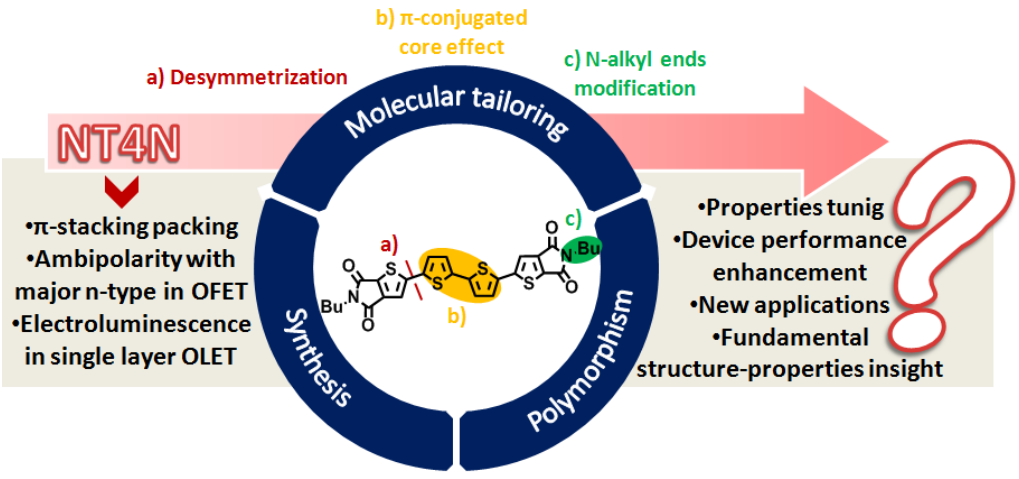

Figure 11. Design strategies for the tailoring of NT4N.

a) In order to understand the role of two 2,3-TI groups in oligothiophenes materials, a *desymmetrization* strategy will be followed by replacing one thienoimide with a simple thiopene (bearing or not alkyl substituents) unit and comparing the non-symmetric derivatives with NT4N and with conventional thiophene based semiconductors (section **3.1**).

b) The tailoring will be then addressed to the core: π-conjugated system *heterocycles* replacement (section **3.2**) and *length* modifications (section **3.3**) will be realized, studying how the optoelectronic and electrical properties in OFETs change as consequence in the synthesized materials with respect to NT4N.

c) The *N-alkyl ends* effect will be discussed in section **3.4**: different sized and shaped chains will be introduced, for the synthesis of a family of NT4N derivatives. Besides the design and synthesis, a deep combined theoretical-experimental investigation approach will be exploited to study the optoelectronics properties, packing, morphology (organization in thin film, self-assembly) and emission/charge transport properties of the newly developed materials, depicted in figure 12.

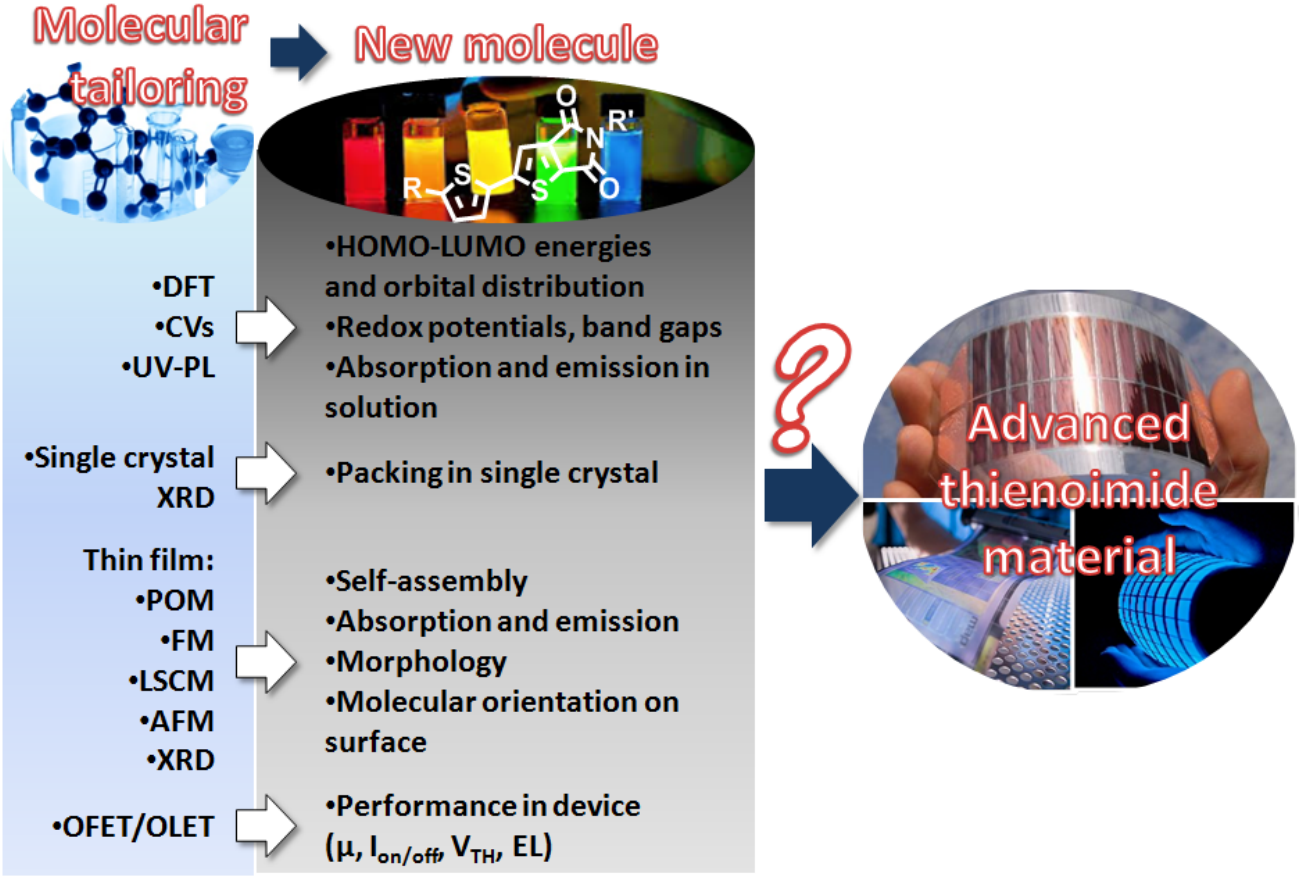

Figure 12. Combined approaches from the molecular tailoring to the development of a potential new multifunctional thienoimide material.

Moreover, particular focus will be given to the molecular packing issues of the newly synthesized thienoimide materials characterized by *polymorphic behaviour*. A part of the work will be indeed

focused on the engineering and control of polymorphism of selected materials, with the aim of developing truly multifunctional materials from a single polymorphic compound (section **3.5**).

Finally, besides the careful discussion on the tailoring studies, innovative synthetic protocols based on *direct arylation* reactions will be applied to the synthesis of various families of π-conjugated materials, characterized by 2,3- and 3,4-thienoimide moieties as well as anthracene and thiophene based building blocks, replacing cross-coupling based conventional methodologies. In section **3.6**, a comparison between the synthetic methods will be carried out, rationalizing the most convenient in terms of yield and purity of the final material, in the view of a scale-up evolution.

Chapter 3

Results and discussion

3.1 Desymmetrization of NT4N

The adopted desymmetrization strategy consistes in the insertion of a thienoimide moiety as end group in two highly performing unipolar oligothiophene based semiconductors, i.e. dihexylquaterthiophene (DH4T), p-type material, and perfluorohexylquaterthiophene[1] (DF4T), n-type material.[2]

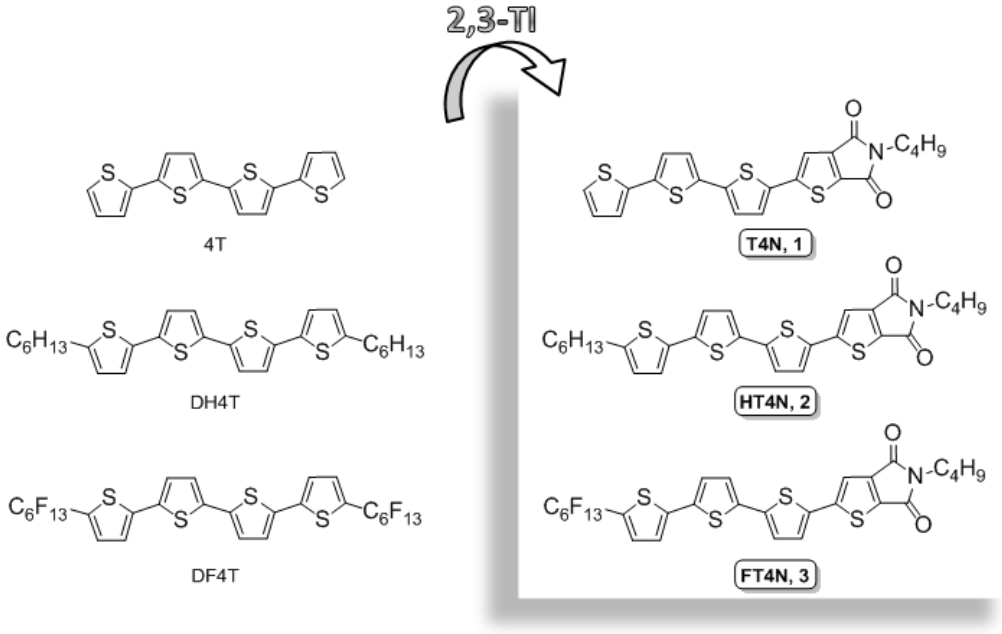

Chart 7. Molecular structure of the developed non-symmetric TI based materials.

Substantially, one of the ends of these symmetric materials, a thiophene bearing an alkyl (for DH4T) or perfluoroalkyl (for DF4T) chain, was replaced with a TI moiety, thus obtaining HT4N and FT4N respectively (chart 7).

Moreover T4N, a derivative with an unsubstituted thiophene ring opposite to the TI moiety, was prepared for comparison.

By following this approach, three non-symmetric 2,3-TI based materials have been synthesized, characterized and tested in OLET devices.

3.1.1 Synthesis, thermal and optoelectronic properties of non-symmetric NT4N derivatives

The target compounds were prepared by a Stille coupling reaction based sequence starting from the brominated TI building block **4**, whose synthesis was already reported in chapter 1.

The synthetic route to T4N, HT4N and FT4N materials is depicted in the following scheme 5.

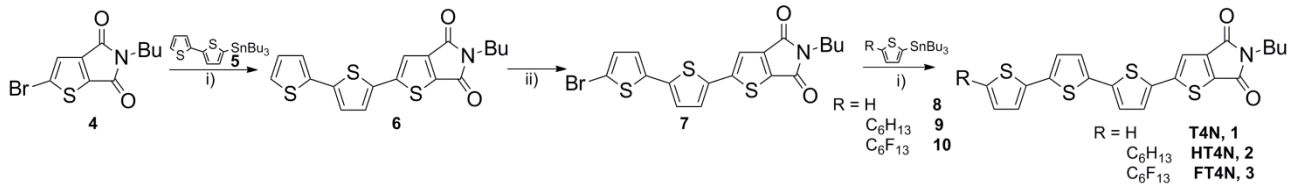

Scheme 5. Synthetic route to T4N, HT4N and FT4N materials. i) Toluene, reflux, in situ $Pd(AsPh_3)_4$. (ii) NBS, CH_2Cl_2/AcOH.

In detail, brominated TI **4** was first made react in a Stille cross-coupling with the commercially available tributylstannyl derivative **5**, obtaining the trimer **6** (Y = 80%). A bromination reaction with NBS in a 1:1 mixture of CH_2Cl_2 and acetic acid led to compound **7** in 97% of yield. Finally, a second Stille cross-coupling reaction between derivative **7** and the stannilated thiophene bearing the proper substituent **8**, **9** or **10**, yielded the target materials T4N (**1**, Y = 55%), HT4N (**2**, Y = 68%) and FT4N (**3**, Y = 74%) respectively after purification steps through flash chromatography on silica gel and following crystallization methods.

Thermal characterization by differential scanning calorimetry (DSC, figure 13) and hot stage polarized optical microscopy (POM, figure 14) revealed thermotropic liquid crystalline properties at temperatures below 200 °C for all the newly synthesized compounds.

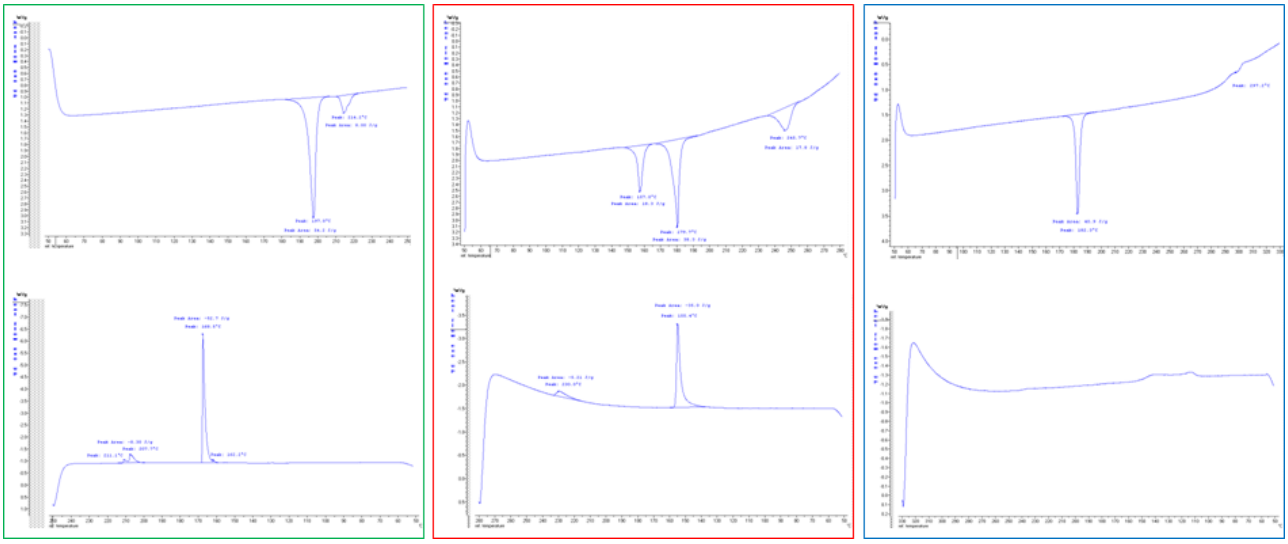

Figure 13. DSC thermograms of compounds T4N (green box), HT4N (red box) and FT4N (blue box), in air (10°C/min).

Figure 13 highlights that all compounds show a complex thermal behaviour with multiple transition peaks. In particular, T4N shows a reversible crystal → liquid crystal (LC) transition at about 197°C followed by melting to isotropic phase at 214°C. HT4N shows the melting transition at about 157°C followed by a transition LC1 → LC2 at 179°C. Finally isotropization occurs at 246°C. FT4N shows a not reversible crystal → LC transition at about 100 °C followed by the transition to isotropic phase at 297 °C.

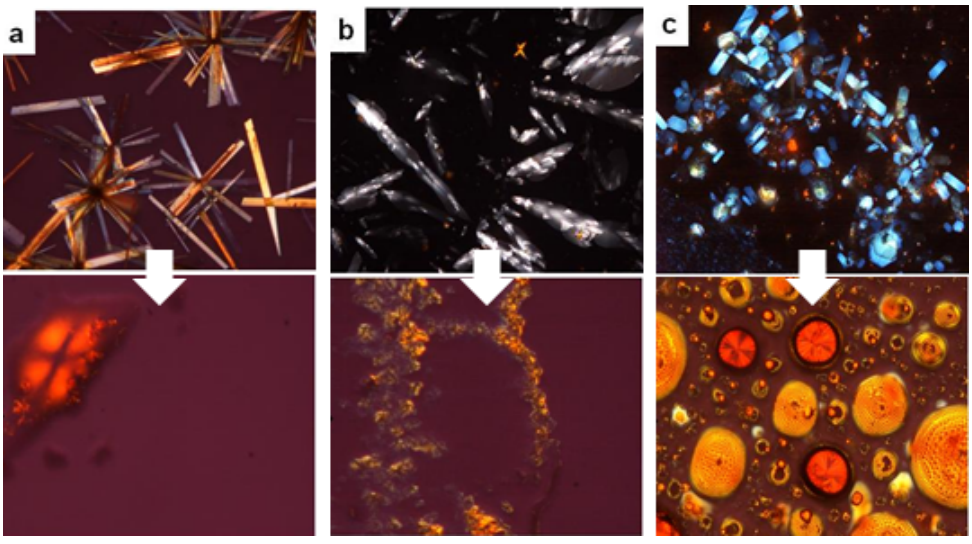

Figure 14. POM micrographs of cast films from toluene on glass of compound T4N (a), HT4N (b) and FT4N (c) at rt (top), and corresponding LC mesophase at 225 °C, 182 °C and 278 °C, respectively (bottom).

Figure 14 shows the polarized optical microscopy (POM) images of cast film (from toluene 1 mg/ml) at room temperature and the corresponding liquid crystalline mesophase at 225°C, 182°C

and 278°C for compounds T4N, HT4N and FT4N respectively.

UV−Vis absorption spectra in CH_2Cl_2 diluted solution (figure 15a-c, left curve) display structured spectra with maximum peaks at similar energetic positions (440−449 nm) regardless of the type of ω-end substituent, in good agreement with the calculated values (reported in table 1). The photoluminescence spectra (PL, figure 15a-c, right curve) are broad, almost unstructured and strongly red-shifted with respect to the absorption spectra. In vacuum-sublimed thin films (figure 15d-f) the absorption spectra are blue-shifted with respect to the solution ones with a convoluted profile exhibiting at least two absorption peaks suggesting the possible formation of aggregates. The thin film PL spectrum of FT4N shows almost identical features to that in solution, while a blue-shifted maximum emission wavelength was found for HT4N and T4N with respect to the solution. HT4N shows a shoulder before the emission maximum resembling the structured spectra observed for NT4N, DF4T, and DH4T compounds and different from those of T4N and FT4N. Moreover, HT4N emission is slightly red-shifted with respect to that of T4N and FT4N. These features suggest the role of the hexyl chain in promoting H-motif-like packing.

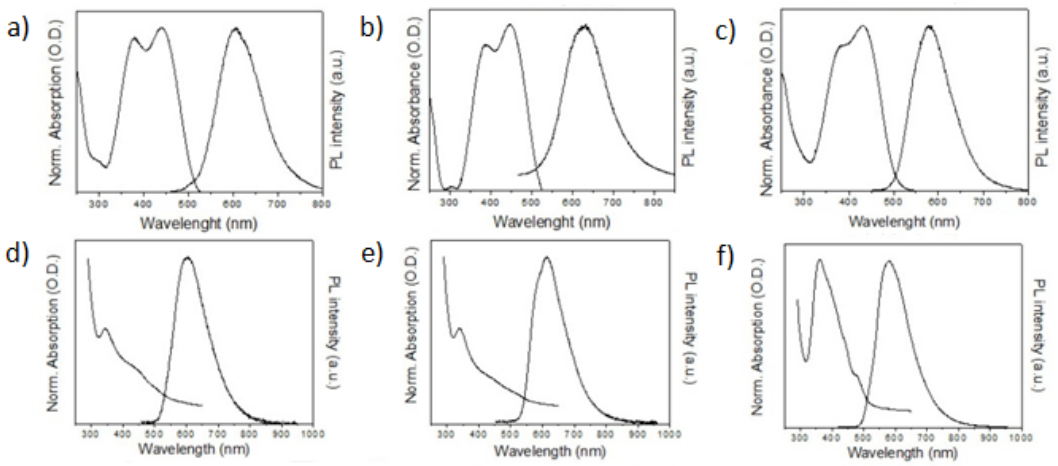

Figure 15. Absorption and emission spectra of (a, d) T4N, (b, e) HT4N, and (d, f) FT4N compounds in CH_2Cl_2 solution (top) and vacuum sublimed film (30 nm thick, bottom).

The PL quantum yield values in solution are in the range 8−17%, i.e., slightly lower with respect those of DH4T and DF4T. On the other hand, the quantum yield of thin films was higher than that of DH4T (1−1.5% vs 0.6%) but markedly lower than that of DF4T (~7%).

In table 1 here following is summarized the optical characterization of the synthesized non-symmetric compounds (T4N, HT4N, FT4N), together with references materials, i.e. DH4T, DF4T and NT4N.

Table 1. Optical and cyclic voltammetry data for all the compounds in chart 7 and for NT4N as symmetric TBI material reference.

Comp.	λ_{abs} [a] nm (theor)	λ_{em} nm[a]	E_g^{opt} eV	λ_{abs} film[b] (nm)	λ_{em} film[b] (nm)	HOMO eV[c] (theor)	LUMO eV[c] (theor)	E_g [c] eV
T4N	441 (442)	606	2.81	344	603	-5.74 (-5.25)	-3.47 (-2.43)	2.27
HT4N	447 (450)	631	2.77	340	584/611	-5.73 (-5.14)	-3.42 (-2.31)	2.31
FT4N	433 (437)	580	2.83	361	580	-5.99 (-5.43)	-3.42 (-2.47)	2.57
NT4N	449 (450)	572	2.76	430	603	-6.00 (-5.51)	-3.47 (-2.62)	2.53
DH4T	401[d]	463, 495, 527	3.09		523/562	-5.5	-2.40	2.87
DF4T	398[e]	458, 489	3.11		524/564/ 614	-6.2	-3.30	2.88

[a]In CH_2Cl_2, 10^{-5} M. [b]30 nm thick film. [c]E_{HOMO} = e(4.68 − E°$_{ox}$); E_{LUMO} = e(4.68 − E°$_{red}$).[3,4] [d]In *o*-chlorobenzene. [e]From ref.[5]

Figure 16 displays the cyclic voltammetry (CV, left) curves of compounds T4N (a), HT4N (b), and FT4N (c), together with DFT calculations (right) for the non-symmetric compounds (d-f) and for the reference compound NT4N (g).

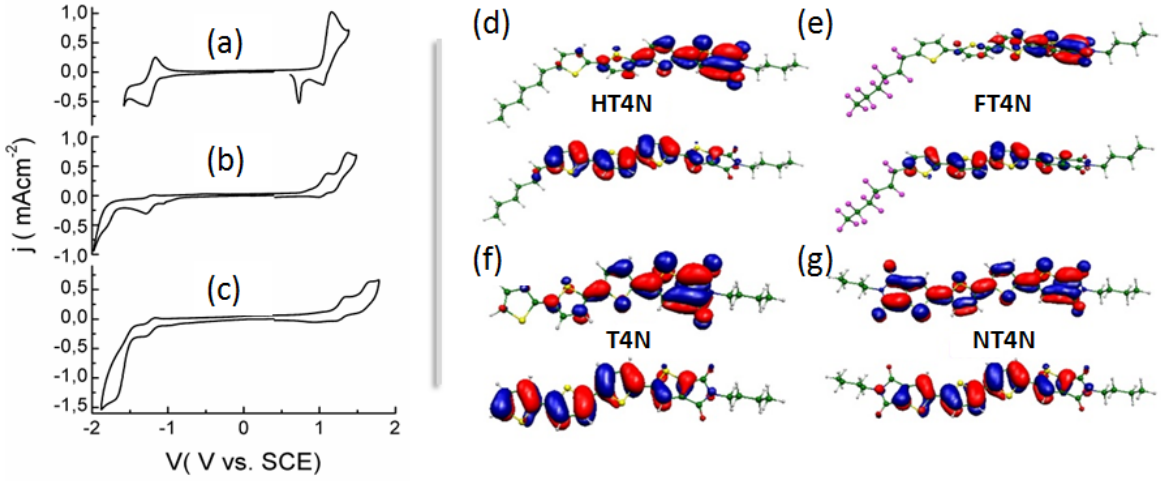

Figure 16. Left: CVs of 1.1 mmol·L^{-1} compounds T4N (a), HT4N (b) and FT4N (c) at 100 mV/s in CH_2Cl_2, 0.1 mol·L^{-1} $(C_4H_9)_4NClO_4$. Right: isodensity plots of the HOMOs (down) and LUMOs (top) for HT4N (d), FT4N (e), T4N (f) and NT4N (g).

Compound T4N (figure 16a) shows a quasi-reversible reduction wave at E°$_{red}$ = −1.22 V, related to the TI moiety, and an oxidation wave at E°$_{ox}$ = 1.10 V. whose current is enhanced by the electrochemical–chemical–electrochemical kinetics of the dimerization at the terminal thiophene

group. The reverse wave is split in two current peaks, the lower one (1.05 V) due to the reduction of the radical cation, and the sharper one (0.73 V) to the reduction of the dimer.

The voltammogram of HT4N (figure 16b) shows two oxidation waves at $E°_{ox1}$ = 1.05 V and $E°_{ox2}$ = 1.28 V. On the other hand, it shows a quasi-reversible reduction wave at $E°_{red1}$ = −1.24 V and an irreversible reduction wave at $E^{1/2}_{red2}$ = −1.75 V due to the oligothiophene moiety. Finally, the quasi-reversible reduction of compound FT4N (figure 16c) occurs at the same potential of compound HT4N, with the irreversible one at $E^{1/2}_{red2}$ = −1.58 V which is 0.17 V less negative than that of HT4N. This potential shift is due to the electron withdrawing effect of the perfluorohexyl chain opposite to the TI moiety, which also influences the oxidation potential. Indeed, the oxidation potential shifts to more positive potentials, i.e., $E°_{ox1}$ = 1.29 V and $E°_{ox2}$ = 1.63 V, enhancing the energy gap of the frontier orbitals (E_g = 2.57 eV vs 2.31 eV).

Overall, the electrochemical data show that the number of thienoimidic end units provides a minor effect on the LUMO energy value. Indeed, LUMO energy values of compounds T4N, HT4N, and FT4N are similar to that of NT4N. On the contrary, HOMO energy of T4N and HT4N are higher than those of NT4N and FT4N. Finally, compound NT4N presents a HOMO energy value between those of DF4T and HT4T (−6.00 eV, −6.2 eV, and −5.5 eV, respectively).

DFT calculations[6] were carried out to gain insights on the frontier orbital distribution. In all the compounds the HOMO is delocalized over the entire molecule (figure 16d-g, bottom) while the LUMO is delocalized along the whole molecule only for symmetric NT4N (figure 16g, top). For non-symmetric compounds the LUMO is instead mainly localized on the thienoimide moiety, independently on the type of its opposite substitution (figure 16d-f, top). This explains the reason why the LUMO energy level results insensitive to the type of the oligomer end.

Together, electrochemical and theoretical data highlight how in TI end substituted compounds it's possible to tune just the HOMO energy level maintaining an unaltered LUMO level, simply by changing the type of end substituent opposite to TI.

The crystal structures of compounds T4N and FT4N, having in common a nearly planar backbone, are shown in figure 17a-b. In the crystal packing of T4N (Figure 17c), the molecules are aligned in an antiparallel way with respect to each other and adopt a herringbone-like arrangement with slipped π-π stacking (figure 17e). Differently for T4N, in FT4N one of the two independent molecules shows the usual anti−anti−anti orientation of the S atoms whereas the second one exhibits an uncommon syn−anti−anti conformation (figure 17d).

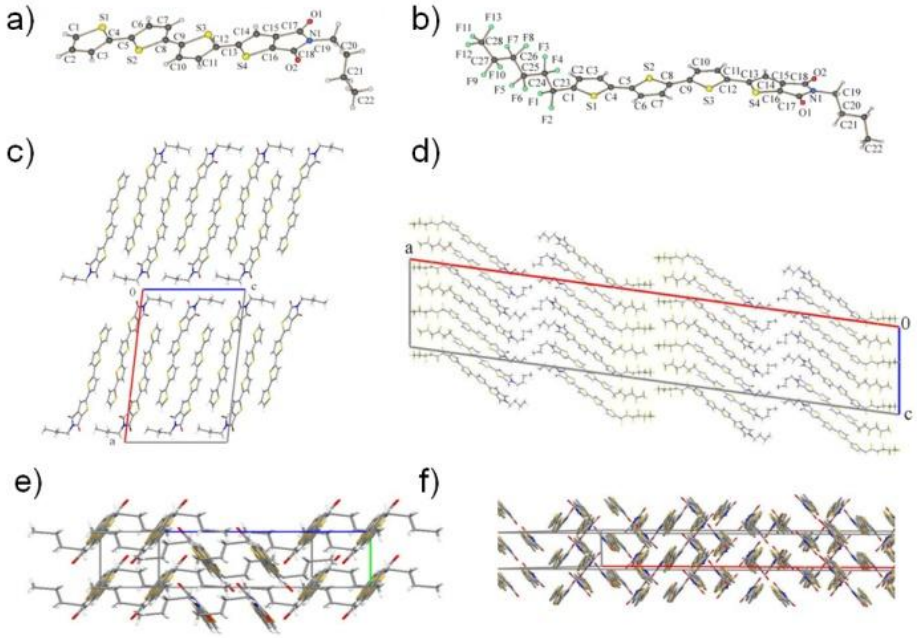

Figure 17. Crystal structure of T4N (a) and FT4N (b). (c,d) View down the b axis of the crystal packing of T4N and FT4N respectively. (e, f) View along the long molecular axis of T4N and FT4N respectively, showing the herringbone-like packing. The H atoms, the perfluorohexyl and n-butyl chains in FT4N have been removed for clarity.

In the crystal packing of FT4N the two conformers are aligned face-to-face and establish a slipped π-π stacking. Looking down the long molecular axis a herringbone-like pattern is noticed (figure 17f). Intermolecular C–H···O and C–H···F interactions connect the π–π stacks.

Interestingly, as described in chapter 1, while compounds T4N and FT4N show herringbone-like packing, as generally observed for linear alkyl end substituted oligothiophenes,[7] NT4N characterized by two thiemoimide end moieties, showed a slipped π–stack packing motif.

The XRD of the vacuum evaporated films suggests a molecular organization with the long molecular axis almost perpendicular to the surface (figure 18a-b) as generally observed for oligothiophenes , as well as for NT4N (see chapter 1). The morphology investigation of the same films by atomic force microscopy (AFM, figure 18c-e) revealed highly three-dimensional and poorly interconnected fiber-like crystal structures for all the compounds. Underneath these structures, a more uniform terraced morphology was visible, suggesting a good suitability of these compounds for thin film transistors applications.

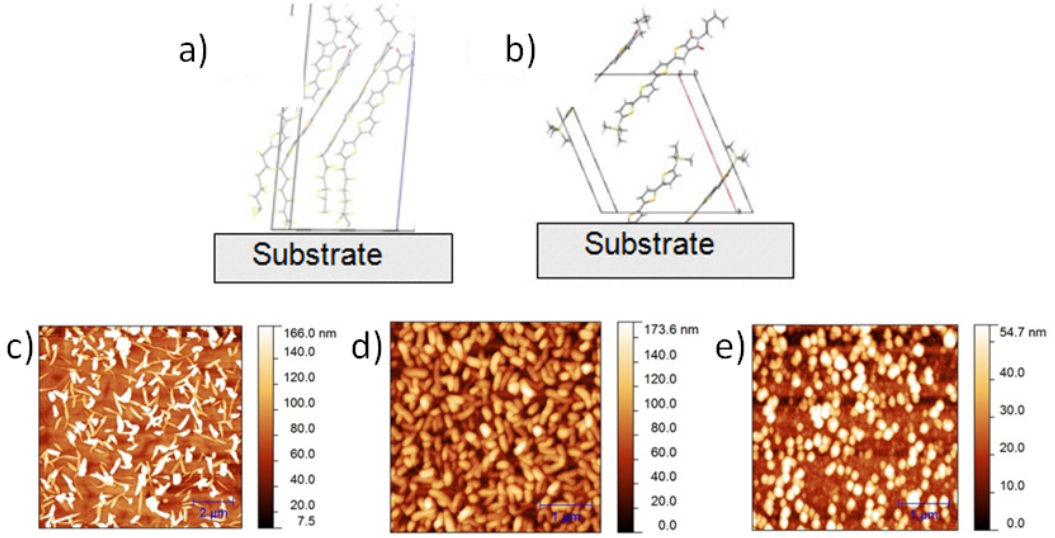

Figure 18. Top: sketch of the molecular organization of a) FT4N and b) HT4N on the substrate. Bottom: AFM images of films grown on PMMA of c) T4N (15 nm thick), d) HT4N (30 nm thick) and e) FT4N (30 nm thick), obtained by vacuum sublimation.

3.1.2 Electrical characterization and molecular structure–charge transport relationships

Electrical characterization in a field-effect device (bottom-gate top-down configuration) was performed to analyze the charge transport properties in thin films of the synthesized molecules.

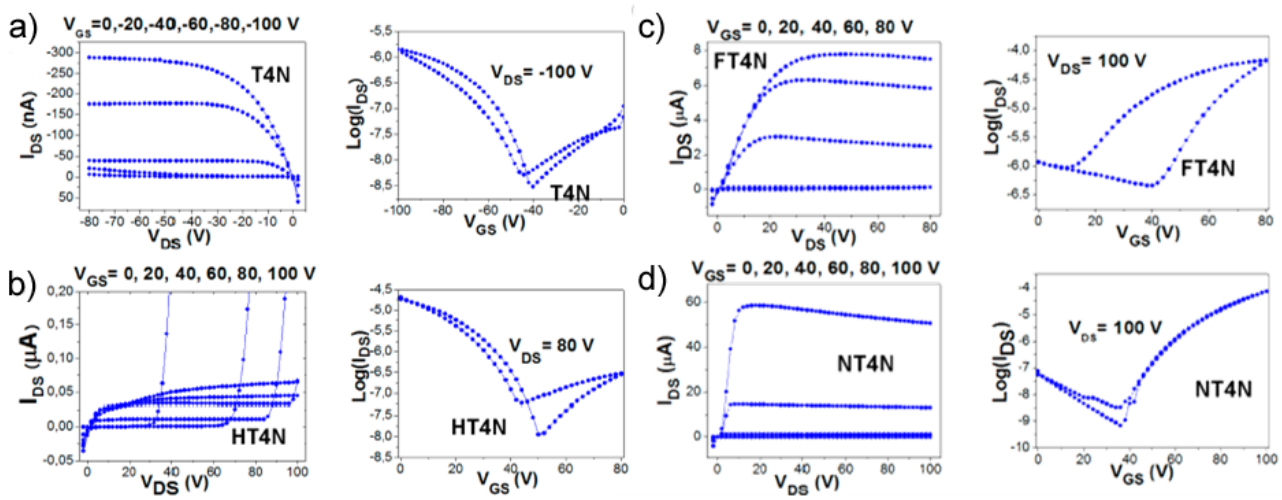

Figure 19. Electrical characteristics for T4N (a), HT4N (b), FT4N (c), and NT4N (d) based OFETs. For each material, the left graph is the OFETs output curve while in the right graph is corresponds to the OFETs transfer curve.

The compounds displayed ambipolar charge transport: the electrical transfer characteristics, obtained by sweeping the gate voltage at fixed drain−source bias, show the v-shaped behaviour typical of ambipolar transistors (figure 19a-c). Electrical characterization of NT4N was also performed by optimizing the film processing conditions (figure 19d) with respect the first characterization reported in chapter 1.

Data in table 2 reveal major n-type behaviour for NT4N and FT4N in accordance to the unipolar n-type behaviour observed for oligothiophene bearing electron-withdrawing ends such as DF4T. On the contrary, a major hole charge transport was observed for HT4N and T4N in accordance to the unipolar p-type behaviour of unsubstituted quaterthiophene and DH4T. The reason of such inversion is difficult to explain in terms of different HOMO−LUMO energy levels, being their values very close one another.

However, the molecular packing clearly plays a crucial role on the electrical properties of these materials. The comparison between NT4N and FT4N is strongly indicative. Even if the HOMO−LUMO energy levels (see table 1) and the thin film morphology of these two compounds are almost identical, their charge mobilities are markedly different (two and one order of magnitude for the p- and n-type mobilities, respectively).

A significant difference between NT4N and FT4N can be observed in their crystal packing, i.e. herringbone-like for FT4N and π-stack-like for NT4N. The latter packing type has been already related to enhanced charge transport capability in molecular materials,[7] and indeed NT4N shows the best p- and n-type charge mobility with respect to all non-symmetric compounds.

Table 2. Electrical parameters for all the compounds in chart 6 and for NT4N as symmetric reference material.

Compound	μ_h ($cm^2V^{-1}s^{-1}$)	V_T^P/V	I_{on}/I_{off}	μ_e ($cm^2V^{-1}s^{-1}$)	V_T^N/V	OLET EP (nW)
T4N	$1.2\cdot10^{-4}$	-20.7	10^3	$2\cdot10^{-6}$	10.0	*a*
HT4N	$3.1\cdot10^{-3}$	-17.5	10^4	$2.8\cdot10^{-5}$	10.9	8
FT4N	$1.4\cdot10^{-5}$	-39.5	10^4	0,011	19.1	50
NT4N	$7.0\cdot10^{-3}$	-26.7	10^5	0.55	10.0	180
DH4T	0.12	-15.0	10^6	-	-	-
DF4T	-	-	10^6	0.48	38	-

Film thickness 30 nm. [a]Value below the detection limit.

During the electrical characterization of OFETs, intense electroluminescence emission from the devices was also measured, highlighting the potential of these materials for single layer ambipolar OLETs devices.

Figure 20a–c shows the optoelectronic transfer curves of single layer OLET devices based on HT4N, FT4N, and NT4N compounds respectively. The device architecture is invariant for all devices (bottom-gate top-contact geometry) to enable a direct comparison of the electrical and optoelectronic properties. The peaked electroluminescence corresponding to the maximum electron–hole balance ($V_{GS} \sim 1/2V_{DS}$) shown in figure 20 is a clear fingerprint of the light generation inside the OLET channel, occurring at the spatial position where electron and hole currents meet.

Indeed, in a unipolar OLET, in which only one type of charge is effectively transported through the channel, the light is generated at the drain electrode following the minority carrier injection and the electroluminescence intensity increases monotonically with the applied V_{GS} potential.

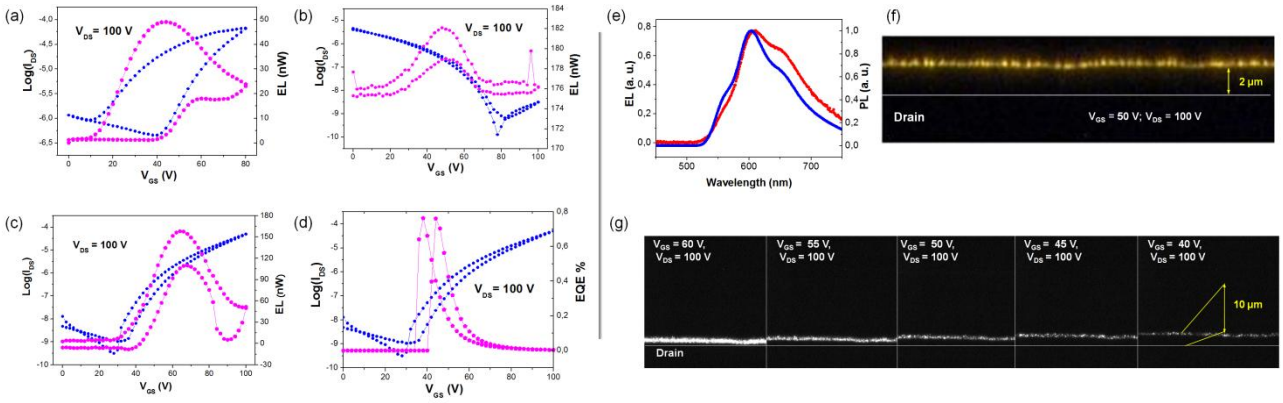

Figure 20. Optoelectronic transfer curves of an OLET device based on (a) FT4N, (b) HT4N, and (c) NT4N molecules. The blue lines represent the measured OLETs drain current, and the purple lines are the emitted photons power. (d) EQE efficiency curve for NT4N based OLET. The blue line is the drain current, and the purple line is the EQE. (e) Electroluminescence spectrum of OLET based on NT4N (red line) compared to the PL spectrum (blue line). (f) Optical microscope image of a working FT4N OLET. (g) High resolution inverted microscope image of a working NT4N OLET highlighting the emissive stripe motion within the device channel by decreasing the gate voltage. The device channel size is 70 µm.

Figure 20d shows the plot of the external quantum efficiency for NT4N showing the highest device efficiency. The maximum EQE relevant value is about 0.2%, at 50 V (where the EL intensity is still significant). In figure 20e the EL spectrum compared to the PL of NT4N is shown.

The spectra are very similar, confirming that the EL emission originates from NT4N. Images of working FT4N and NT4N based devices, showing the typical ambipolar OLET emission inside the channel, controlled by the gate potential, are reported in figure 20f,g.

The emissive stripe within the transistor channel is closer to the drain electrode as a consequence of the difference between hole and electron mobilities. However, the electroluminescence generation area is well separated from the drain edge, preventing optical coupling of the emitted light with the metal electrodes.

Taking into account the specific geometry used for our devices (same channel width, PMMA dielectric layer, and gold electrodes) and comparing it with that of F8BT-polymer based OLETs (state of the art ambipolar OLET), it emerges that the total light power of our single layer molecular OLETs compares favorably with it.[8]

Even if the comparison of the maximum observed EQE is still unfavorable, it should be noted that our devices have not yet been optimized to maximize the light outcoupling. Moreover, the intrinsic quantum efficiency of our materials in film is much lower than that of the F8BT polymer, and the hole and electron charge mobility are still quite unbalanced.

3.1.3 Conclusions

The approach of introducing a TI group into linear thiophene oligomers resulted to switch unipolar and non electroluminescent thiophene-based materials to ambipolar and electroluminescent ones.

When in the p-type semiconductor HT4H a hexyl group is replaced by a TI moiety, the resulting material becomes ambipolar, with major p-type character, and electroluminescent. Analogously, ambipolarity, but with major n-type contribution, and consequent electroluminescence are observed for NT4F derived from the n-type FT4F.

The substitution with one TI end moiety can be exploited for i) tuning the HOMO energy values of oligothiophenes while maintaining unchanged the LUMO energy, ii) localizing the LUMO distribution on the oligomer periphery, iii) mastering the charge transport (ambipolar with predefined major p- or n-type behavior) by a proper TI opposite end substitution, and iv) enabling thin film electroluminescence in combination with ambipolar charge transport.

Indeed, end substitution by an electron donating group (EDG) promotes hole charge transport (T4N or HT4N) while an EWG as TI opposite end favors electron charge transport (FT4N).

Given the stringent need for electroluminescent molecular semiconductors, these results are relevant for a deeper understanding of the structure−property relationship in such materials, which is of great relevance and still a matter of debate. Remarkably, by using the newly developed ambipolar and electroluminescent TBI materials we realized thin film single layer ambipolar OLETs with optical power comparable to that of the equivalent polymeric devices.

3.2 Inner core tailoring: heterocycles replacement in NT4N

The insertion of different heterocycles as π-conjugated cores in TBI based materials represented the first approach to tailor the backbone of such semiconductors, with the aim of improving the electrical performances in device.[9]

Two novel compounds featuring fine-tunable inner cores such as bithiazole (Tz - NTzN, **11**, chart 8) and thienothiophene (ThT - NThTN, **12**, chart 8) have been synthesized. Thienothiophene insertion into linear oligothiophenes has been related to efficient hole charge transport.[10] In contrast, the insertion of thiazole rings into trifluorophenyl ended oligothiophenes improves electron charge transport with respect to all-thiophene based analogues.[11]

So, the possibility of controlling the n-type behaviour of TBI based semiconductors by using π-inner cores with an increasing electron-deficiency with respect to the bithiophene core (i.e. NT4N) was envisioned. To further validate this strategy, a probe compound bearing a dimethylated bithiophene inner core (TMe - NTMeN, **13**, chart 8) was also synthesized and investigated.

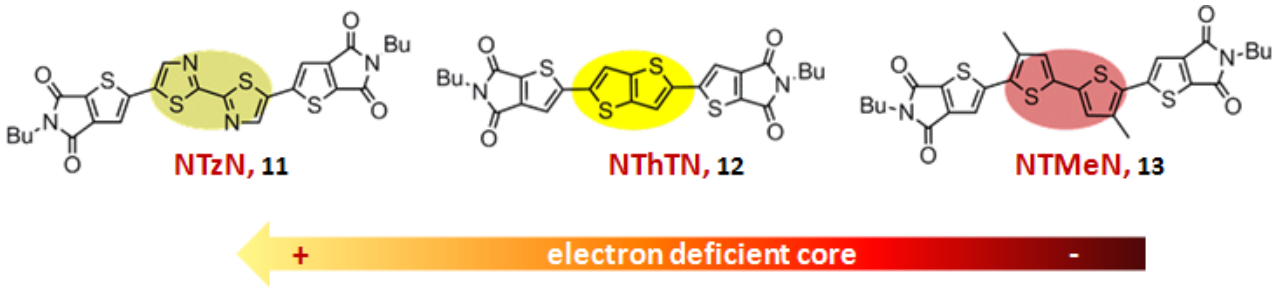

Chart 8. Molecular structure of the newly synthesized TBI based materials bearing different π-conjugated inner cores.

3.2.1 Synthesis, thermal and optical properties

The targeted compounds were prepared through a Stille cross-coupling reaction between the synthesized brominated thienoimide **4** (see details in chapter 1) and the proper distannyl derivative as depicted in scheme 6. Precisely, compound **4** was made react with commercial 2,5-bis(trimethylstannyl)thieno[3,2-b]thiophene **15** to give NTzN **12** in 54% yield. The other two stannilated derivatives, 5,5'-bis(tributylstannyl)-2,2'-bithiazole **14** and (3,3'-dimethyl-[2,2'-bithiophene]-5,5'-diyl)bis(tributylstannane) **16**, were prepared under classical metallation conditions starting from their brominated precursors **17** and **18** respectively, in semi-quantitative

yields. Stille cross-coupling reactions between compound **4** and stannilated derivatives **14** and **16** provided the target materials NTzN **11** and NTMeN **13** in 44% and 64% yield respectively.

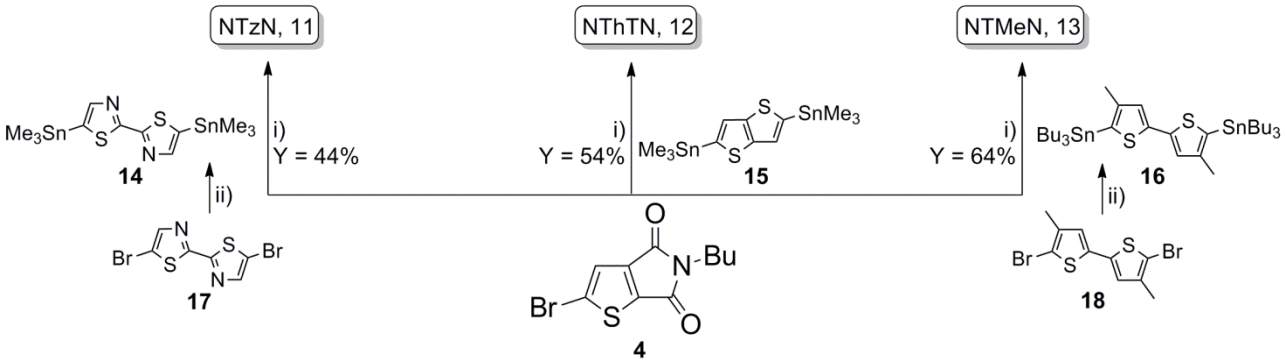

Scheme 6. Synthetic route to NTzN, NThTN and NTMeN materials. i) Toluene, reflux, in situ $Pd(AsPh_3)_4$. ii) BuLi, Bu_3SnCl, Et_2O, -50°C to rt.

Differential scanning calorimetry revealed liquid crystalline properties of NThTN and NTMeN (figure 21). NTzN melts to isotropic phase at 364 °C, instead NThTN shows a reversible crystal → LC transition at about 354°C followed by melting to isotropic phase at 383°C. NTMeN also shows a reversible crystal → LC transition at 242°C followed by melting to isotropic phase at 248°C.

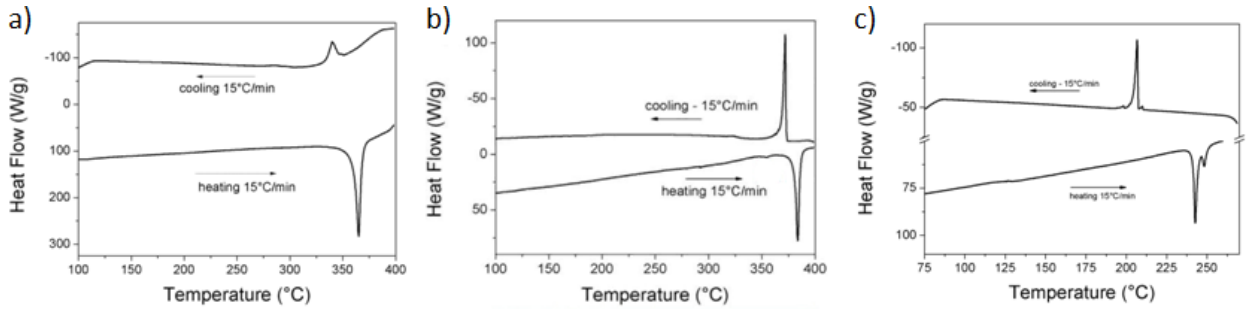

Figure 21. DSC thermograms of a) NTzN, b) NThTN and c) NTMeN in air (15°C/min).

The UV-Vis absorption and emission spectra of compounds **11–13** are shown in figure 22a and the complete list of the optical and electrochemical data is summarized in table 3. Interestingly, the introduction of the Tz core causes a blue shift of the maximum absorption wavelength λ_{max} of about 15 nm and 20 nm with respect to NThTN and NTMeN respectively. The same trend is observed for the maximum emission wavelengths, strongly blue shifted for NTzN with respect to the other compounds. In detail, NTzN showed structured emission with two maxima located at 489 nm and 514 nm respectively. NThTN and NTMeN displayed unstructured emission with the

maxima shifted by 32 nm and 67 nm respectively (figure 22a). The optical energy band gap E^{opt}_g of NTzN was about 0.10 eV higher than those of the other compounds.[12]

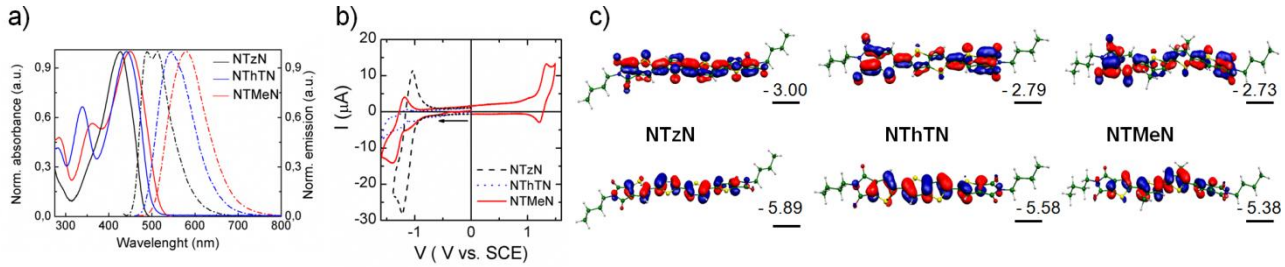

Figure 22. a) UV-Vis and PL spectra in CH_2Cl_2, b) CVs at 0.2 $V \cdot s^{-1}$ of NTzN, NThTN, and NTMeN saturated solutions in CH_2Cl_2 containing 0.1 M $(C_4H_9)_4NClO_4$, c) isodensity plots for NTzN, NThTN and NTMeN (HOMOs bottom, LUMO top).

CVs of compounds NTzN and NThTN show a quasi-reversible reduction wave (note: NThTN gives a current too low to allow an accurate determination of reduction potential) while NTMeN shows both reduction and oxidation quasi-reversible waves in the electrochemical window of the electrolytic solution (figure 22b), in agreement with the smaller E_g^{opt} (table 3). The reduction potential $E°_{red}$ becomes more negative on passing from NTzN to NTMeN suggesting a less delocalized LUMO in the latter.

Accordingly, DFT calculations performed with B3LYP functional[13] and a 6-31G* basis set show that in NTzN both the HOMO and LUMO are almost uniformly delocalized on the entire molecular backbone (figure 22c). In contrast, for NThTN and NTMeN the HOMO (bottom) is mainly localized in the inner core while the LUMO (top) is localized at the periphery of the electron-withdrawing TI ends. Such orbital distribution suggests higher suitability to charge transport for NTzN since higher intermolecular overlap (favourable to charge transport) can be expected for conjugated oligomers having uniformly distributed frontier orbitals.[14]

Table 3. Experimental and calculated optoelectronic parameters for the synthesized compounds.

Comp.	$\lambda_{abs}{}^a$ (nm)	$\lambda_{em}{}^a$ (nm)	$E°_{ox}{}^b$ (V)	$E°_{red}{}^b$ (V)	E_{HOMO} (eV) (theor)	$E_{LUMO}{}^c$ (eV) (theor)	$E_g^{opt\ d}$ (eV)
NTzN	428	489/514	>1.6	-1.13	-5.81[e] (-5.89)	-3.24 (-3.00)	2.57
NThTN	443	546	>1.6	-1.2	-5.69[e] (-5.58)	-3.2 (-2.79)	2.49
NTMeN	449	581	+1.28	-1.26	-5.65[e] (-5.38)	-3.11 (-2.73)	2.39

[a]In CH_2Cl_2. [b]Vs. SCE in CH_2Cl_2 containing 0.1 $mol \cdot L^{-1}$ $(C_4H_9)_4NClO_4$. [c]E_{LUMO} = e(4.37 + $E°_{red}$), E_{HOMO} = e(4.37 + $E°_{ox}$).[3] [d]$E_g^{opt} = 1240/\lambda_{onset}$.[15] [e]$E_{HOMO} = E_{LUMO} - E_g^{opt}$.

Thin deposits of the newly synthesized compounds were analysed by polarised optical microscopy to investigate the self-organization capability of these materials at surface. Upon drop-casting, all compounds formed isolated micrometre sized, birefringent crystals whose shape depends on the substrate and the solvent used (figure 23b).[16] However, a lithographically controlled wetting (LCW, figure 23a)[17] technique allowed the fabrication of parallel micrometre-sized stripes (μ-stripes) of a few millimetres length (figure 23c) covering the entire substrate.

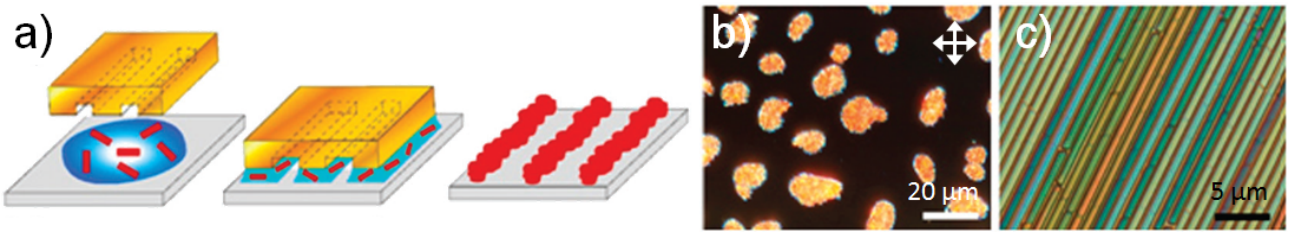

Figure 23. Thin deposit and μ-stripes of NTMeN fabricated by LCW on the Si/SiO_2 surface. (a) Scheme of the LCW process. (b) POM image of a drop cast film, taken with crossed polars oriented along the axes of the image. (c) Optical micrographs of μ-stripes.

Although some cracks appear along the μ-stripes, they look very homogeneous (figure 24) and exhibit the typical behaviour of optically anisotropic birefringent materials.

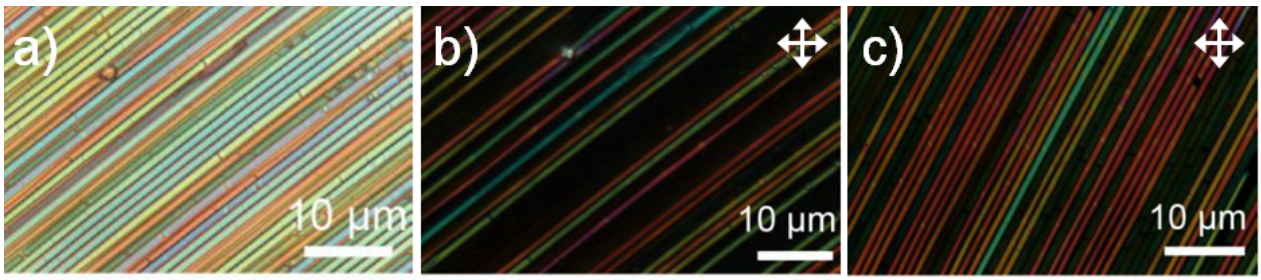

Figure 24. Optical micrographs of μ-stripes recorded: a) under un-polarized light, b) with crossed polars oriented along the axes of the image, c) with crossed polars oriented along the axes of the image rotating the sample ~30°.

In particular, they appear homogeneously coloured, highlighting an almost constant thickness over the entire stripe. The μ-stripes extinguish in four positions at intervals of 90°. Although the cracks, the light extinction occurs at the same orientation in every position within a single μ-stripe (figure 24b), suggesting the crystalline domains grow with the same orientation inside each stripe. However, the variation of the extinguishment angle for different stripes (figure 24c), indicates a different crystallographic orientation of them respect to one another. It can be evinced by this behaviour that the confined deposition by LCW induces a coherent, long-range order along the direction of the stripes independently in each of them.

3.2.2 Electrical characterization

The electrical properties of the synthesized materials were measured in bottom-gate top-contact OFET devices (N_2 atmosphere, 1 ppm O_2, 1 ppm H_2O).

The device responses are reported in figure 25 showing the multiple output curves for each compound. NTzN shows exclusively electron charge transport with charge mobility values of up to μ_e = 0.16 $cm^2/V{\cdot}s$ and a threshold voltage V_T^e = 39.7 V (table 4).

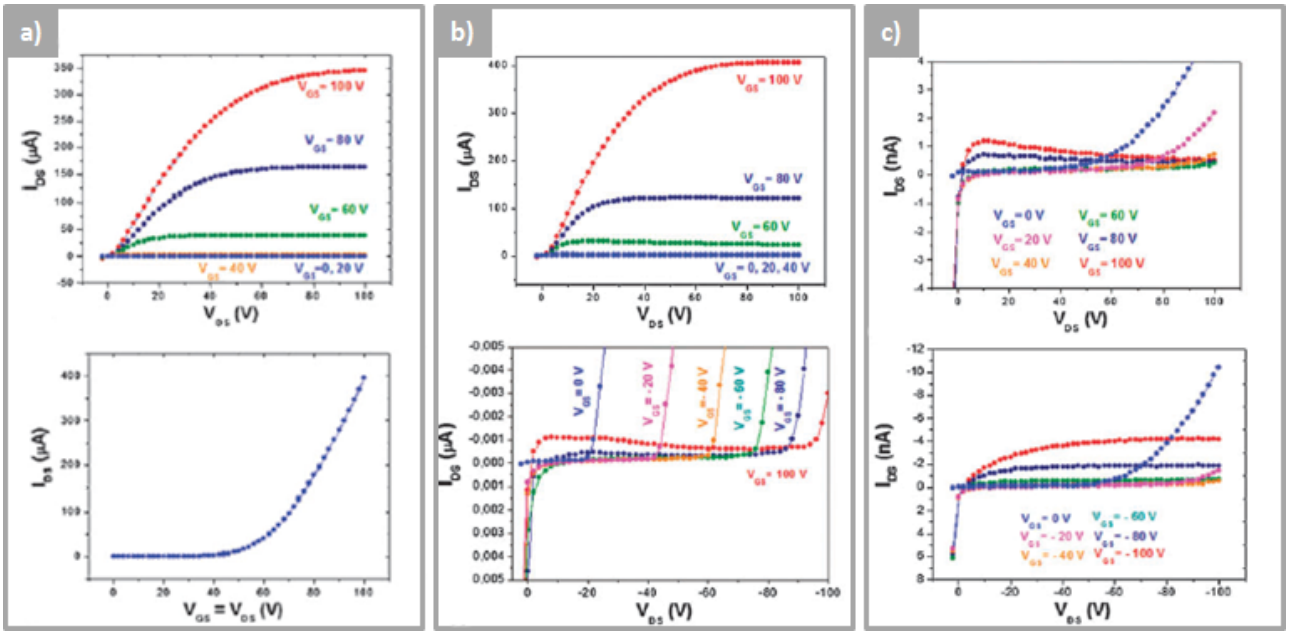

Figure 25. (a) Multiple output n-type (top) and locus n-type (bottom) curves for NTzN, (b) multiple output n-type (top) and multiple output p-type (bottom) curves for NThTN, (c) multiple output n-type (top) curves for NTMeN, (f) multiple output p-type curves for NTMeN.

In contrast, NThTN shows ambipolar charge transport with an excellent electron charge mobility of μ_e = 0.3 $cm^2/V{\cdot}s$ but higher threshold voltage (with respect to NTzN) and a hole mobility of μ_h = $6.4{\cdot}10^{-5}$ $cm^2/V{\cdot}s$ (table 4). Both electron mobility values are one order of magnitude higher than that observed for the already reported NT4N (chapter 1, μ_e = $5.3{\cdot}10^{-2}$ $cm^2/V{\cdot}s$ for not optimized devices) and comparable or even better than the best performances so far achieved for n-type thiophene based materials.[1,18] It should be noted that no device optimization (i.e. substrate functionalization or annealing procedures) was performed. The electron mobilities drop by about three orders of magnitude on passing to NTMeN having the more electron rich methylated bithiophene inner core (table 4).

Table 4. Electrical parameters for the synthesized compounds **11**-**13**.

Compound	μ_h (cm^2/V·s)	V_T^h/V	I_{on}/I_{off}	μ_e (cm^2/V·s)	V_T^e/V
NTzN	nd	nd	10^7	$1.6\cdot10^{-1}$	39.7
NThTN	$6.4\cdot10^{-5}$	-67.3	10^6	$3.0\cdot10^{-1}$	62.6
NTMeN	$3.0\cdot10^{-6}$	-45.0	10^4	$1.3\cdot10^{-5}$	56.9

The beta methyl substitution could prevent a close molecular overlap required for efficient charge transport, thus it would explain why so low mobility values have been registered for NTMeN. Moreover, the unipolar rather than ambipolar behaviour observed for NTzN could be due to the less favourable matching of the estimated HOMO energy of NTzN (lower than the other compounds) with the gold electrode work function which limits the hole injection.

Collectively the results of this study reveal that electron deficient cores strongly improve the electron charge transport capability of thieno(bis)imide based materials.

3.2.3 Conclusions

In conclusion, by exploiting the inner core heteroatoms replacement design approach, two new efficient and highly processable n-type molecular semiconductors based on the combination of thieno(bis)imide end units with thiazole and thienothiophene π-inner cores have been presented. Electron charge mobility values of up to 0.3 cm^2/V·s (in un-optimized devices) were measured for these materials. Such OFET performance is one order of magnitude higher than those achieved by using unsubstituted bithiophene π-cores (NT4N) and three orders of magnitude higher with respect to NTMeN having a more electron rich core.

3.3 Tailoring of the oligomer size (NT3N and NT5N vs NT4N)

With the aim of exploring the full potential of TBI based materials for applications in charge transport based devices, the oligomer length i.e. different π-conjugation extent, is herein discussed as a pivotal tool to control the optoelectronic and electrical properties of TBI materials.[19]

It should be noted that odd-membered oligothiophenes T5 and T7 based systems, have shown peculiar optical[20] self-organizing properties[21], and electrical properties with respect to even membered materials, most intensively studied over the past few years. Accordingly, two new TBI odd-membered oligomers (shown in chart 9), trimer NT3N (**19**) and pentamer NT5N (**20**) were selected as model compounds and investigated. Their optoelectronic and electrical properties have been compared to those of NT4N and to those of conventional unsubstituted oligothiophenes (T3, T4 and T5).

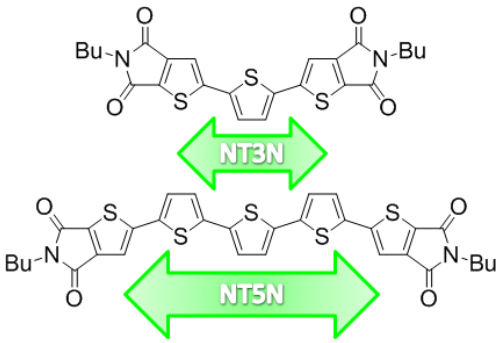

Chart 9. Molecular structure of NT3N and NT5N TBI based materials.

3.3.1 Synthesis, characterization and optoelectronic properties

Two different synthetic approaches to prepare these novel materials have been tested and compared, i.e. conventional Stille cross-coupling way and a *direct arylation* route, a method which avoids the use of organometallic species. Its main advantages reside in less synthetic steps and easier purifications but this issue will be discussed in details in the section dedicated to the synthetic strategies (section 3.6).

For the Stille cross-coupling conventional route, the brominated TI **4** constituted the starting material for both NT3N and NT5N (scheme 7). Optimal reaction conditions required the use of in situ prepared $Pd(AsPh_3)_4$ catalyst and the corresponding bis-stannyl thiophene derivative under

refluxing toluene. The target trimer **19** was isolated in 65% yield after the coupling with commercial 2,5-bis(tributylstannyl)thiophene **21**, and the subsequent purification by flash cromatography and following crystallization from toluene. Pentamer **20** was instead synthesized (63% yields) by coupling compound **4** with the stannylated terthiophene derivative **22**, prepared from commercial 5,5''-bibromo-2,2':5',2''-terthiophene by a conventional stannylation reaction in a semi-quantitative yield.

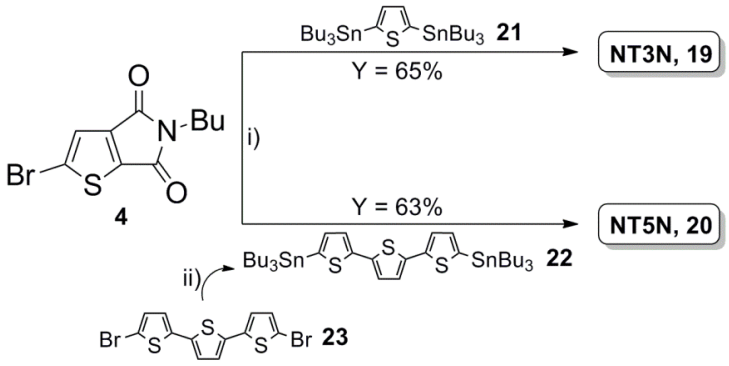

Scheme 7. Stille cross-coupling route to NT3N and NT5N materials. i) Toluene, reflux, in situ $Pd(AsPh_3)_4$. ii) BuLi, Bu_3SnCl, Et_2O, -50°C to rt.

UV–Vis absorption analysis shows a red shift of the maximum absorption wavelength on passing from NT3N to NT4N to NT5N (λ_{max} = 428 nm, 449 nm and 465 nm respectively, figure 26a and data in table 5).

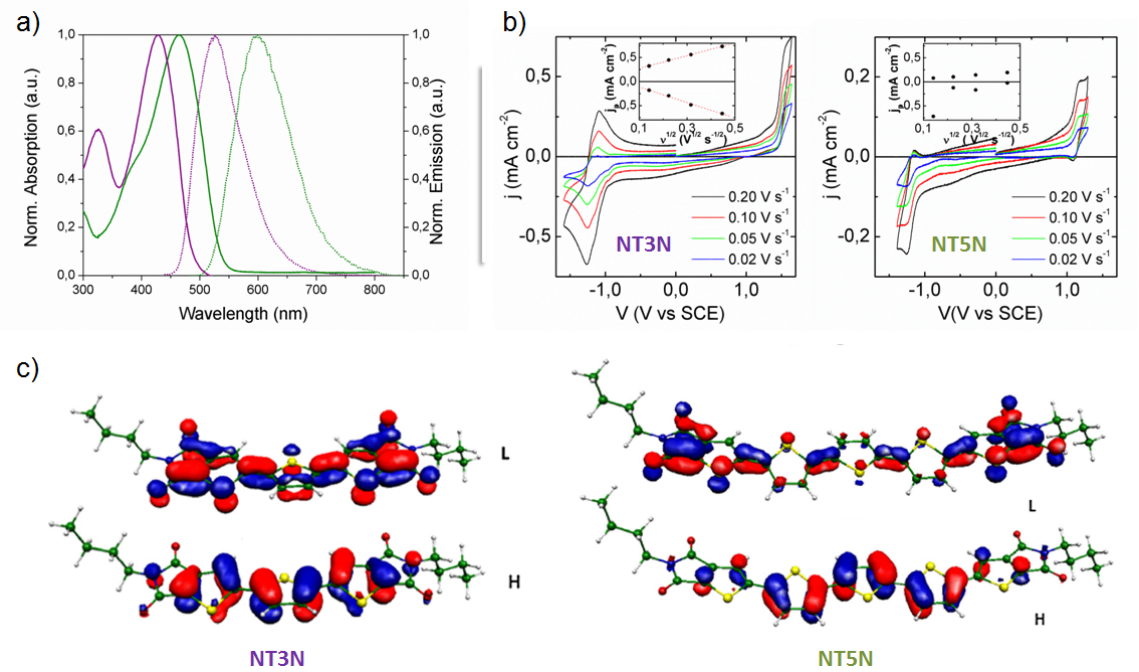

Figure 26. (a) UV–Vis spectra of NT3N (purple lines) and NT5N (green lines) and corresponding PL spectra (dotted lines), in CH_2Cl_2. (b) CVs at several scan rate of NT3N (left) and NT5N (right). In the inset the peak currents vs. the square root of the scan rate. (c) Isodensity for the LUMOs and HOMOs levels of NT3N (left) and NT5N (right).

PL followed the same trend, showing spectra with the λ_{max} located at 526 nm, 572 nm and 599 nm for NT3N, NT4N and NT5N respectively (figure 26a, values in table 5). In general a strong red shift for both the absorption and the emission spectra was observed for TBI based compounds with respect to unsubstituted analogues, ascribed to the presence of the carboxylic groups of the thienoimide, which extends the degree of π-conjugation. Accordingly, lower band gap energies were calculated for TBI based compounds with respect to conventional T3, T4 and T5 having the same number of thiophene units respectively. On going to thin films spectra (not depicted herein but values in table 5), the absorption spectra extend to higher energies and are structured with respect to the solution ones, as expected for an ordered system of interacting linear molecules. Indeed, the solid state PL spectra are less broad and more structured with respect to those in solution, with at least three peaks. Moreover, only NT3N spectrum is clearly red-shifted with respect to the correspondent one in solution. This feature suggests an extended delocalization of the electronic excitation-possibly due to a higher crystalline degree in solid-state for NT3N.

The cyclic voltammetries (figure 26b, data in table 5) of NT3N show an irreversible oxidation wave with the half wave potential $E_{1/2}$ = 1.49 V vs. SCE (1.09 V vs. Fc/Fc+), and a quasi-reversible reduction wave with the standard potential E° = -1.18 V vs. SCE (-1.58 V vs. Fc/Fc+).

The energies of NT3N frontier orbitals can be estimated as E_{HOMO} = -6.17 eV and E_{LUMO} = -3.50 eV, consequently the electrochemical band gap results E_g^{elec} = 2.67 eV (table 5)[3]. NT5N shows a quasi-reversible oxidation wave at 1.14 V vs. SCE (0.67 V vs. Fc/Fc+) and a quasi-reversible reduction one at -1.21 V vs. SCE (-1.68 V vs. Fc/Fc+, figure 26b). As expected the electrochemical band gap resulted lower than that of the shorter analogue (E_g^{elec} = 2.35 eV).

Table 5. Optoelectronic parameters for NT3N, NT4N, NT5N and reference compounds T3, T4 and T5.

Compound	λ_{abs} sol/film (nm)	λ_{em} sol/film (nm)	E_g^{opt} (eV)[a]	E_g^{electr} (eV)	HOMO (eV) exp/theo	LUMO (eV) exp/theo
NT3N	428/405	526/550	2.89	2.67	-6.17[b]/-5.73	-3.50[b]/-2.80
NT4N[c]	449/430[c]	572/603[c]	2.76	2.53	-6.00[b]/-5.51	-3.47[b]/-2.62
NT5N	465/398	599/620	2.66	2.35	-5.82[d]/-5.23	-3.47[d]/-2.74
T3	355[e]	407/426[e]	3.49	3.02	-5.58[d]	-2.56[d]
T4	390[e]	437/478[b]	3.17	2.71	-5.43[d]	-2.72[d]
T5	416[e]	482/514[e]	2.98	2.52	-5.34[d]	-2.82[d]

[a] $E_g^{opt} = 1240/\lambda_{max}$. [b] E_{HOMO} = e (4.68 -E°$_{ox}$); E_{LUMO} = e (4.68 -E°$_{red}$) vs SCE.[13] [c] From ref. 2,9. [d] E_{HOMO} = e (4.62 -E°$_{ox}$); E_{LUMO} = e (4.62 -E°$_{red}$) vs Ag/AgCl.[22] [d] In $CHCl_3$, values taken from The Handbook of Oligo-and Polythiophenes.[23] Film thickness 100 nm.

DFT calculations show a HOMO orbital in all cases delocalized over the entire molecular backbone. On the contrary, the LUMO orbital is mainly localized on the electron withdrawing TI groups, at the oligomer ends (figure 26c). Accordingly, while the HOMO levels increase from NT3N to NT5N, the LUMO energy value is almost unaffected by the conjugation length (table 5) as also observed for TBI based tetramers (as reported in the previous sections).

As for the TBI analogues the HOMO energy of conventional T3 and T5 increases on increasing the conjugation length but for these compounds contrarily to the TBIs the LUMO energy decrease on going from T3 to T5.

Thermal characterization by DSC (figure 27) revealed liquid crystalline properties for compound NT3N with a transition to liquid crystal located at about 200°C closer to the clearing point (205°C). As expected NT5N showed higher melting point (258°C), close to that of conventional T5, but differently from NT3N no evidences of LC behaviour were found.

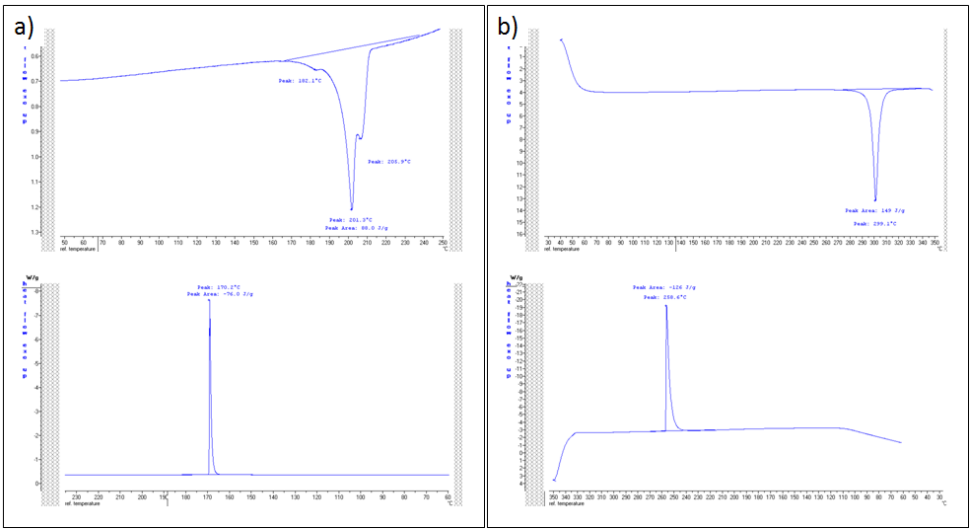

Figure 27. DSC thermograms of a) NT3N (5°C/min) and b) NT5N (25°C/min) under atmospheric conditions.

3.3.2 Thin film morphologies and electrical properties

In order to determine the field-effect transport properties of the new compounds, a bottom-gate top-contact OFET based on vacuum evaporated films (30 nm thick) was realized and characterized. Figure 28a-b shows the AFM topographical image of the vacuum evaporated films of NT3N and NT5N.

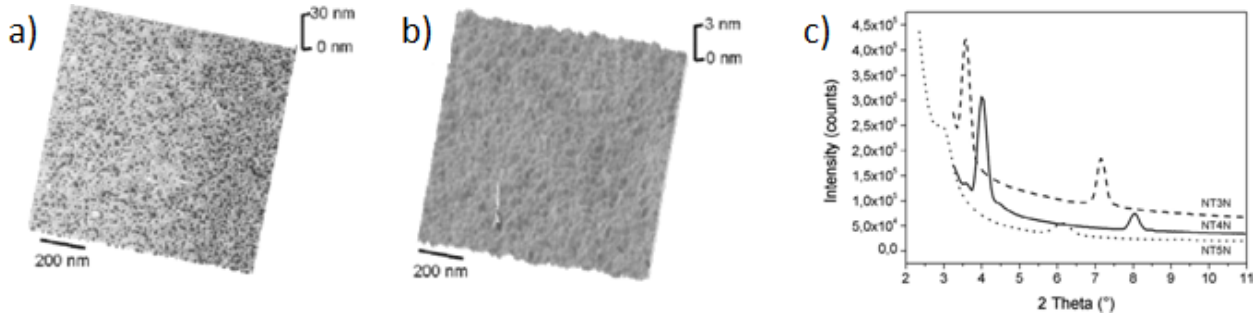

Figure 28. AFM images of vacuum evaporated thin films a) of NT3N, 15 nm thick, b) NT5N 30 nm thick and c) XRD of the same films (together with NT4N one).

The film of NT3N appears homogeneous at large scale with a r.m.s. roughness of about 4 nm, and formed by a homogeneous distribution of fibers structures covering ~60% of the surface area (figure 28a). On the other hand NT5N, forms a highly homogeneous and smooth film with a r.m.s. roughness of about 6 Å (figure 28b). Figure 28c, shows the X-ray diffraction profiles of the vacuum sublimed films. The lower angle peaks are located at 2.2 nm for NT3N, 2.4 nm for NT4N and 2.8 nm for NT5N and almost correspond to their molecular length (2.4, 2.8 and 3.2 nm respectively). This suggesting a vertical, tilted orientation of the molecules with respect to the substrate.

Figure 29 shows the output locus and saturation curves of the synthesized materials.

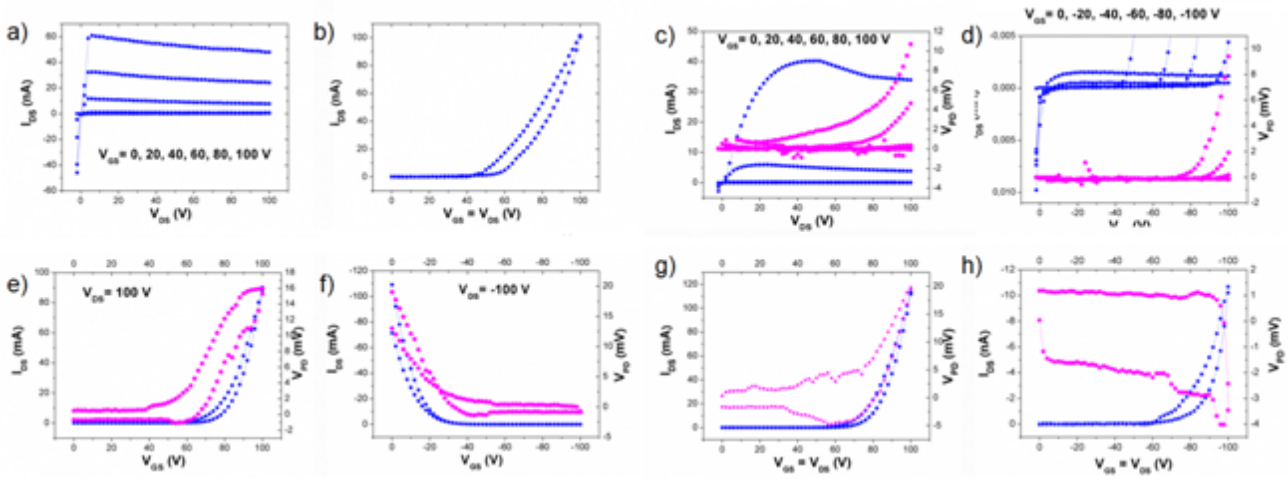

Figure 29. Electrical characteristics of single layer OFET based on NT3N and NT5N. a) p-type multiple output and b) locus curves of NT3N. c) n-type and d) p-type multiple output curves for NT5N. e) n-type and f) p-type transfer saturation curves for NT5N. g) n-type and h) p-type locus curves for NT5N. Electroluminescence from NT5N based devices is reported in magenta curves.

OFETs based on NT3N show exclusively electron transport with mobility $\mu_e = 10^{-4}$ cm^2/V·s. To the best of our knowledge this is the only case of linear terthiophene reported so far showing charge transport, in particular n-type one. Indeed, n-type behaviour with mobility values up to 0.2 cm^2/V·s in air has been reported only for quinoidal dicyanomethylene end functionalized

terthiophenes,[24] while no charge transport was found for non-quinoidal perfluorohexyl end substituted terthiophene[25] pertaining to one of the most investigated class of n-type small molecule semiconductors. Moreover, differently from conventional unipolar T5 and perfuoro-end-substituted T5, NT5N based devices showed ambipolar behaviour, confirming that the TBI insertion in oligothiophenes promotes ambipolar charge carrier transport.

Data in table 6, also show that an increase of the electron charge mobility values ($10^{-4} \rightarrow 10^{-1}$ $cm^2/V{\cdot}s$) can be achieved on passing from NT3N to NT5N.

Table 6. Electrical parameters for the synthesized compounds NT3N, NT4N and NT5N.

Compound	μ_h ($cm^2/V{\cdot}s$)	μ_e ($cm^2/V{\cdot}s$)	V_T^h (V)	V_T^e (V)	$I_{on/off}$
NT3N	-	$1.0{\cdot}10^{-4}$	-	31.7	10^4
NT4N[a]	$6.4{\cdot}10^{-5}$	$5.3{\cdot}10^{-2}$	-71.0	60.0	10^6
NT5N	$1.6{\cdot}10^{-5}$	$1.4{\cdot}10^{-1}$	-60.3	64.3	10^6

[a]Data from ref. 26 (devices prepared in not optimized experimental conditions).

The hole mobility values are instead insensitive to the oligomer size increasing. Indeed, the hole mobility, which is negligible for NT3N, remained unchanged for NT5N with respect NT4N, in the standard device preparation conditions (not the optimized ones). The unbalanced holes and electrons charge mobilities can derive by a complex interplay between optoelectronic and molecular packing properties. Contrarily to conventional oligothiophenes having HOMO and LUMO orbitals homogeneously distributed over the entire backbone, like in also the other TBI based derivatives, the LUMO results mainly located on the thienoimide moiety, i.e., at the oligomer periphery. In thin films, the adopted molecular packing allows a good LUMO's overlap (allowing the electron transport) but a poorer HOMO's overlap, this limiting the p-type contribute to charge transport. The molecular packing could also explain the increase in n-type mobility on increasing the oligomer length. Although single crystal structures of NT3N and NT5N are not known (no singles crystals could be isolated), XRD analysis of thin films, suggest they adopt a π-stacking similar to that of NT4N described in chapter 1, for which structural analysis revealed a vertical molecular orientation, with respect to the substrate,[26] with a partial interdigitation between overlapped layers.

Therefore, assuming that the same π-stacking mode is adopted also by NT3N and NT5N, the increasing length and consequently the increasing π-electron density, would improve the π-stacking attitude, promoting the enhanced charge transport capability on increasing the oligomer length. Figure 29c–f also shows the electroluminescence signal, observed for NT5N during the

OFETs characterization. Interestingly, the EL displayed by NT5N, confirm the suitability of TBI based compounds different from quaterthiophenes, as ambipolar and electroluminescent materials for OLETs.

3.3.3 Conclusions

In summary with this approach, the effects of the variation of the π-core length of NT4N on the optoelectronic and electrical properties have been investigated.

Optical analysis shows a strong red shift of both absorption and emission spectra of NT3N and NT5N with respect to conventional oligothiophenes having the same size. CVs and DFT calculations reveal that, while the HOMO energy level is strongly influenced by the number of conjugated units as observed for conventional oligothiophenes, the LUMO level, being localized on the TBI moiety, is poorly affected by the oligomer size. This is crucial for tuning the HOMO level while maintaining unchanged the LUMO. Despite the short oligomer size, significant electron mobility values (up to 10^{-4} $cm^2/V{\cdot}s$) were observed for NT3N. Only by increasing the oligomer size to tetramer and pentamer, ambipolar semiconducting properties and electroluminescence can be achieved. Indeed, also NT5N is ambipolar and electroluminescent, but it displays electron mobility value one order of magnitude higher than that of NT4N measured under the same experimental conditions.

3.4 N-alkyl ends tailoring

Besides the modification of the inner core of TBI based materials, the N-alkyl end chains substitution was investigated as a design strategy to change the solid state organization and packing in thin films.[27]

Maintaining fixed a quaterthiophene sized (T4) π-conjugated backbone, TBI derivatives (namely collectively Cx-NT4N) with linear (C1–C8), branched (C6) or cyclic (C6) alkyl end substituents (chart 10) have been synthesized.

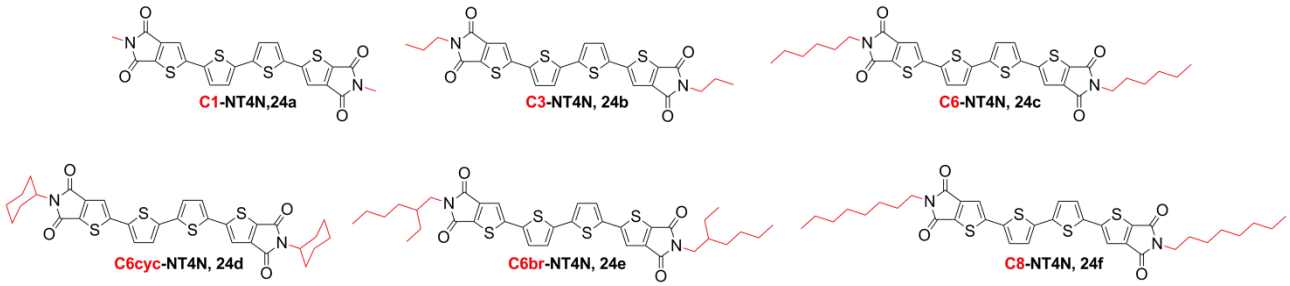

Chart 10. Molecular structure of Cx-NT4N materials **24a-f**, bearing different linear, cyclic and branched N-alkyl ends.

3.4.1 Synthesis, optical and thermal characterization

Compounds Cx-NT4N were prepared by conventional Stille cross-coupling reaction from 5,5'-bis(tributylstannyl)-2,2'-bithiophene **29** and the proper brominated TI **28a-f** (scheme 8) catalyzed by in situ prepared $Pd(AsPh_3)_4$. The thienoimides bearing the different N-alkyl ends were synthesized by intramolecular nucleophilic acyl substitution of the thienoanhydride **25** with the proper alkylamine (**26a-f**), followed by intramolecular dehydration of the intermediates through refluxing $SOCl_2$, as reported in chapter 1 for NT4N.

The isolated yields of the Stille cross-coupling reactions after purification by flash-chromatography on silica gel followed by crystallization from toluene, ranged from 40% to 80% mainly depending on the final material solubilities. Methyl and cyclohexyl substituted C1-NT4N and C6cyc-NT4N showed a poor solubility in organic solvents like toluene and CH_2Cl_2. The solubility increased by increasing the chain length or by using branched substituents.

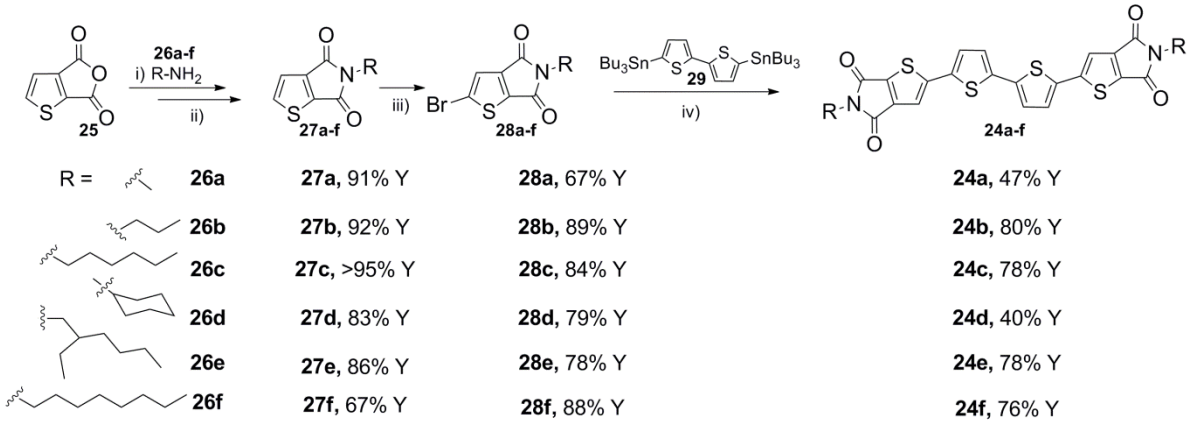

Scheme 8. Synthetic route to the target compounds. (i) Toluene, reflux, (ii) $SOCl_2$ reflux. (iii) TFA/H_2SO_4, NBS. (iv) $Pd(AsPh_3)_4$, toluene, reflux.

The UV-Vis absorption spectra in diluted CH_2Cl_2 solutions were almost comparable for all the compounds with the maximum absorption wavelength at about 350 and 450 nm. The emission spectra are featureless with the emission maximum wavelength at around 570 nm. Absorption and emission values are summarized in table 7 and as reference, the spectra of C8-NT4N are reported in figure 30a.

The absorption spectra of vacuum-sublimed thin-films are well structured with absorption maxima at about 345 and 430 nm for compounds bearing linear alkyl substituents with C > 1. C1-NT4N was the only compound showing the absorption maximum red-shifted to 450 nm. By increasing the alkyl chain length from C1 to C8 units no relevant variations in PL spectra were observed (in figure 34b the spectra of C8-NT4N is reported as reference material). All the values related to the films from C1- to C8-NT4N are shown in table 7, together with the corresponding PL quantum yields (ø), resulted almost invariant within the experimental error ranging between 3.5% (C8-NT4N) and 6.5% (C6br-NT4N).

Table 7. Spectroscopic parameters of CH_2Cl_2 diluted solutions and thin films (100 nm thick) of compounds **24a-f**.

Compound	λ_{abs} (nm) (solution)	λ_{em} (nm) (solution)	λ_{abs} (nm) (film)	λ_{em} [a] (nm) (film)	ø[b](%)
C1-NT4N	451	570	350, 450	617	4
C3-NT4N	451	572	345, 429	605	6
C6-NT4N	451	568	346, 426	602	5
C6cyc-NT4N	444	568	365, 432	592	4
C6br-NT4N	451	571	368, 446	604	6.5
C8-NT4N	450	568	345, 427	604	3.5

[a]λ_{exc} = 325 nm. [b]Excitation at absorption maximum.

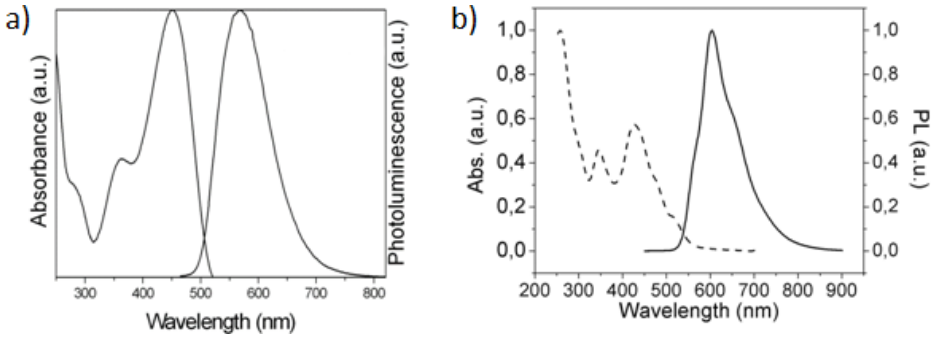

Figure 30. UV-Vis and PL spectra of compound C8-NT4N in a) CH_2Cl_2 diluted solution and b) vacuum-sublimed thin-film.

The thermal behaviour of compounds Cx-NT4N was investigated by differential scanning calorimetry combined to hot-stage polarized microscopy of thin deposits analyses. For almost all the materials, DSC traces show multiple temperature transitions beyond the melting one revealing liquid crystalline properties for these compounds, with exception for C1-NT4N and C6cyc-NT4N derivatives. All the transition temperatures and the melting enthalpies are indicated in table 8.

Table 8. Thermal properties of the synthesized materials **24a-f**.

Compound	Transition temperature [°C] (melting enthalpies [J g^{-1}])	
	Heating (20°C/min)	Cooling (20°C/min)
C1-NT4N[a]	nd	nd
C3-NT4N	274 (3.0), 289 (73.4), 301 (1.1)	262 (55.2), 281 (1.0),
C6-NT4N	244 (1.5), 265 (21.3), 287 (5.9)	219 (0.8), 243 (21.4), 269 (4.9)
C6cyc-NT4N	344 (1.8), 367 (73.9)	329 (15.1)
C6br-NT4N	218 (1.1), 235 (26.1)	213 (29.4), 201 (0.6)
C8-NT4N	121 (2.7), 248 (40.5), 279 (12.1)	231 (41.9), 266 (11.9)

[a]No transitions were observed up to 400°C.

Accordingly to DSC, hot-stage POM revealed LC properties for all these compounds, while only thermal decomposition was observed for C1-NT4N. The thin deposits of compounds Cx-NT4N for POM analysis were prepared by drop casting a chloroform solution (30 µl of 1 mg/ml or saturated solution) on quartz slides in a saturated atmosphere of solvent vapours. In all the deposits, larger crystals (size >100 µm, with the shape dependent on the molecular structure) accumulate at the boundaries while towards the centre of the droplet their sizes decrease till a few µm; moreover, in the case of compounds C3-, C6- and C8-NT4N a continuous film in between the crystals was observed by AFM and POM.

Compound C8-NT4N is discussed as a representative case for all the family and figure 31 summarizes its thermal behaviour.

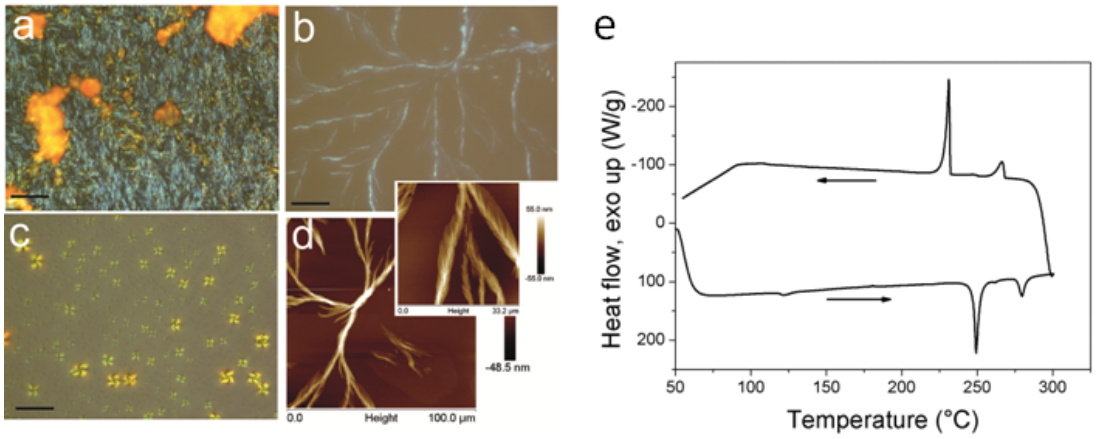

Figure 31. Thermal behaviour of compound C8-NT4N. POM micrographs (cross polars are oriented parallel and perpendicular to the axis of the images): a) birefrangent continuous film at the boundary of the deposit (bar 100 µm); b) fiber-like crystals at the centre of deposit (bar 10 µm); c) LC phase at 260°C (bar 100 µm). d) AFM image. e) DSC thermograms.

Under POM, the film exhibits birefringence without extinguishing at any direction (figure 31a). Furthermore in the centre of the deposit birefrangent fiber-like crystals are often observed (figure 31b). The fiber-like crystals appear as long crystallites (>50 µm) randomly distributed on the surface, with width ranging from 200 µm to 10 µm (resulting in a length–width ratio between 1 : 5 and >1 : 10). The fibers exhibit a strong birefringence, however they do not extinguish at any directions, indicating their polycrystalline nature. In accordance with the DSC trace (figure 31e), C8-NT4N thin deposits show a transition to the LC phase at 255 °C followed by the transition to the isotropic phase at 280 °C. By heating above 255 °C, C8-NT4N becomes a liquid crystal and de-wets forming a homogeneous distribution of droplets exhibiting the typical behaviour of a smectic liquid crystal (figure 31c). Accordingly, AFM (figure 31d) investigation revealed crystals with well defined borders and angles and very slight roughness terraces (r.m.s. roughness <1 nm).

3.4.2 XRD of single crystal, powder, thin films

Compound C3-NT4N was taken as reference compound since it afforded single crystals useful for crystal structure solution and molecular packing determination. The molecule of C3-NT4N is centrosymmetric and the backbone is almost planar being the two inner thiophene rings strictly

coplanar and the dihedral angle between the thiophene and the thienoimide units 1.1(4)° (figure 32a). Moreover, interestingly, the thienoimide units result in uncommon syn conformations with their adjacent thiophene ring (figure 32a). The π-conjugated backbones of C3-NT4N adjacent molecules run parallel to one another and the molecules are involved in a bifurcated C–H---O hydrogen bond to form a 1D network (figure 32b). The π-stack and hydrogen bond interactions pack efficiently the molecules to form layers having in the inner part the conjugated backbone and the alkyl chains on the surfaces (figure 32c).

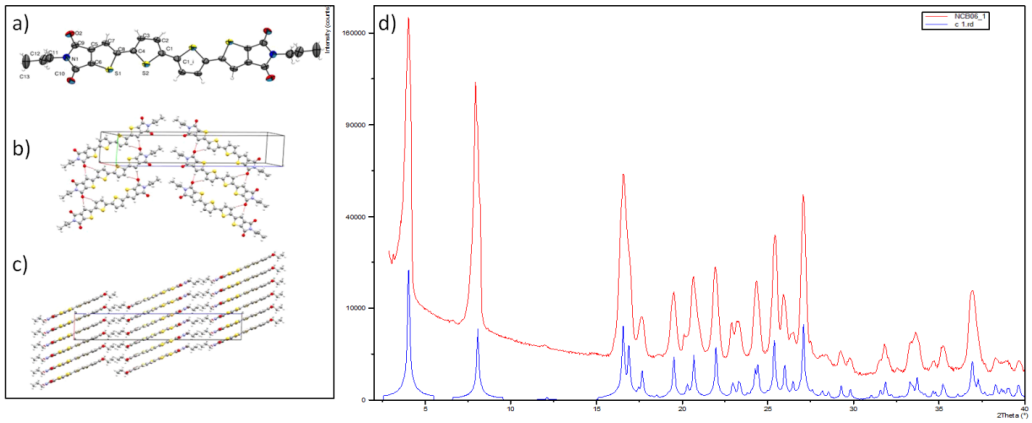

Figure 32. (a) ORTEP drawing of C3-NT4N (displacement ellipsoids drawn at the 50% probability level). Unlabeled atoms are related to the labeled atoms by symmetry operation ½-x, ½-y, -z. (b) Arbitrary units of the crystal packing showing the C-H---O interactions (red lines). (c) View along the b axis showing the π-stack interactions and the assembly of the layers. (d) Comparison between experimental (red line) and calculated (blue) profile for compound C3-NT3N.

Figure 32d shows that the XRD pattern calculated from the structural data (blue line) fits very well with that experimentally collected for the C3-NT4N powder sample (red line) confirming that the crystal phase is the same. Even if not shown herein, no significant differences were observed for the other compounds showing XRD patterns of the powder reminiscent of that of C3-NT4N.

The XRD plots of vacuum evaporated films on PMMA substrate for compounds bearing linear alkyl chains C1–C8-NT4N are shown in figure 33a. They high intensity in the *0 0 l* reflections of C3-NT3N based device reveals the presence of a strong preferential orientation of the molecules with respect to the substrate in the film. The profiles are very similar to one another differing in the position of the main reflections. Indeed each profile shows two or more intense and sharp reflections that are further orders of the interlayer distance reported in the inset of figure 33a.

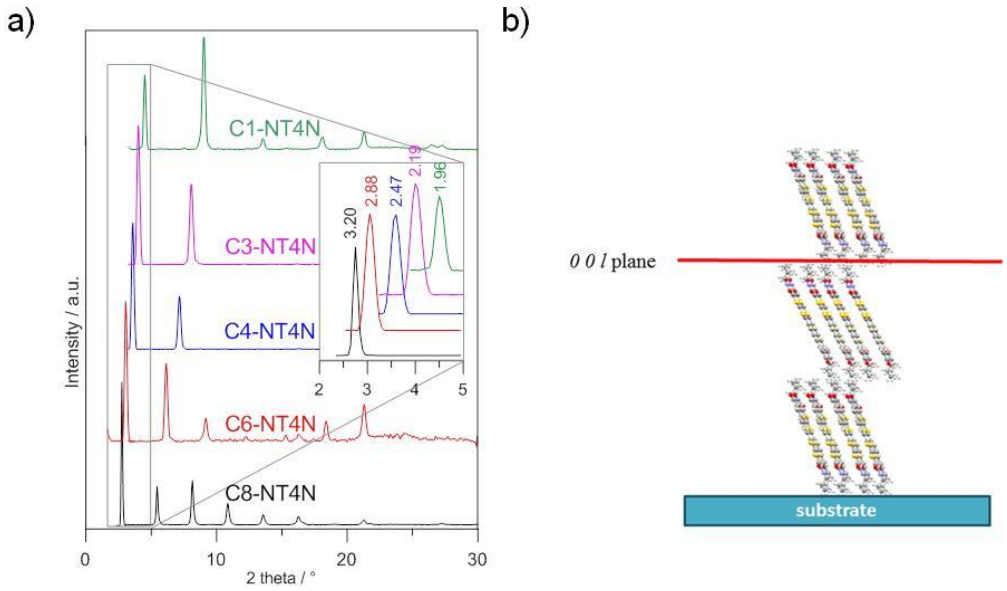

Figure 33. (a) XRD patterns of compounds C1, C3, C4, C6, C8-NT4N devices directly exposed to the X-ray beam. In the inset the small angle region is enlarged and the corresponding interlayer distances are reported in nm. b) Schematic representation of the C4-NT4N molecules arrangement on the substrate.

3.4.3 Electrical characterization and structure-properties relationships

Electrical characterization of the synthesized materials bearing different alkyl chains was performed in devices with bottom-gate top-contact configuration. Charge transport and electroluminescence data expressed as device emission power for all the synthesized materials are summarized in table 9.

Table 9. Electrical parameters for compounds the synthesized Cx-NT4N materials measured under the same experimental conditions.

Compound	μ_e ($cm^2/V{\cdot}s$)	μ_h ($cm^2/V{\cdot}s$)	V_T^e (V)	V_T^h (V)	EP [nW]
C1-NT4N	$3.0x10^{-1}$	$2.8x10^{-3}$	27	-61	nd
C3-NT4N	$2.4x10^{-1}$	$1.5x10^{-4}$	40	-45	30
C6-NT4N	$1.7x10^{-1}$	$1.3x10^{-4}$	20	-66	145
C8-NT4N	$3.2x10^{-1}$	$3.0x10^{-3}$	28	-62	150
C6cyc-NT4N	$2.9x\ 10^{-2}$	nd	40	nd	nd
C6br-NT4N	nd	nd	nd	nd	nd

Film thickness 100 nm.

Considering the electrical properties, contrarily to conventional oligothiophenes, for which cyclohexyl end substitution promotes charge transport,[28] C6cyc-NT4N showed lower electrical

performances. Similarly, the branched C6-tail does not promote either charge transport or EL. On the other hand, linear alkyl tail bearing compounds (C1–C8-NT4N) showed ambipolar behaviour with a major n-type contribution to charge transport. The hole mobility covered a wide range of values, oscillating between 2 and 3.5 orders of magnitude lower than electron mobility that ranged between $1.7 \cdot 10^{-1}$ and $3.2 \cdot 10^{-1}$ $cm^2/V \cdot s$. Locus, multiple output and saturation curves for reference material C8-NT4N are shown in figure 34.

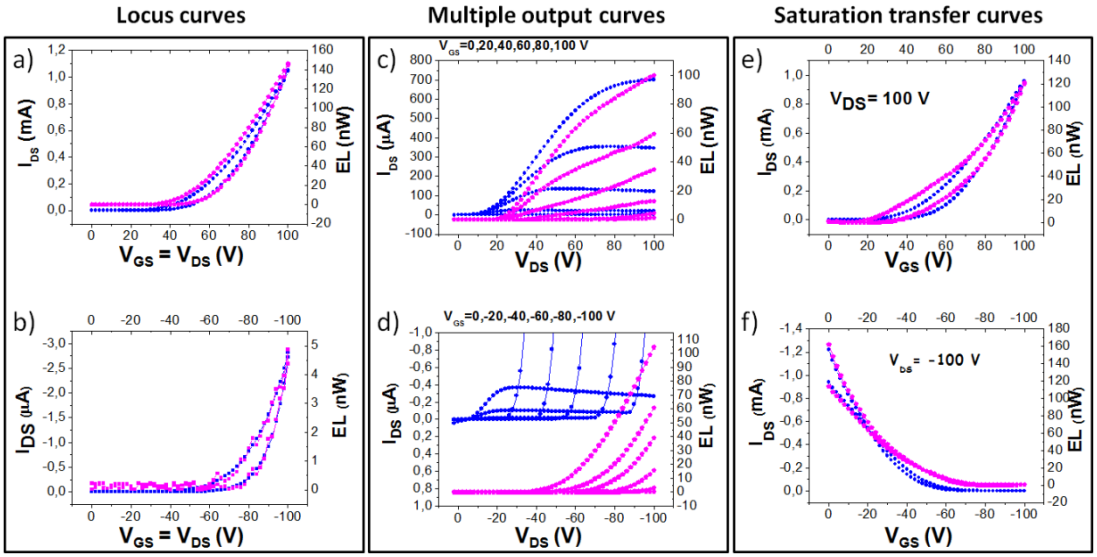

Figure 34. Locus, multiple output and saturation transfer curves for compound C8-NT4N. a), c) and e) n-type, b), d), and f) p-type. In each graph, the blue dotted curves represent the device drain-source current (referred to the left scale), while the purple dotted curves represent the emitted optical power (referred to the right scale).

The observed major electron charge transport was investigated by theoretical calculations in the framework of the small polaron hopping model.[28] A thorough understanding of the correlation between the molecular structure and charge mobility is provided by the investigation of the inner *reorganization energy* λ_i and the charge *transfer integral* τ, parameters influencing the mobility. The former corresponds to the energy loss when a charge carrier passes through a molecule and is dependent on the conjugation length, degree and packing; the latter is the degree of molecular orbital overlap of adjacent molecules and thus depends on the π-π distance, orientation and displacement distance. A high value of mobility is usually obtained with a large transfer integral and a small reorganization energy. Table 10 shows the calculated reorganization energies λ_i for all the synthesized materials.

Table 10. Calculated frontier orbitals and intramolecular reorganization energy, λ_i of compounds Cx-NT4N.

Compound	λ_i^h [meV]	λ_i^e [meV]	HOMO [eV]	LUMO [eV]
C1-NT4N	321	328	-5.56	-2.89
C3-NT4N	319	333	-5.53	-2.87
C6-NT4N	342	351	-5.55	-2.84
C8-NT4N	341	350	-5.54	-2.84
C6cyc-NT4N	346	366	-5.53	-2.83
C6br-NT4N	330	349	-5.54	-2.85

Only minor differences in calculated λ_i are observed by varying the alkyl substituent type and/or length, with all the values included in a 30-40 meV width range. Moreover, the slight promotion of p-type transport in terms of λ_i (i.e. $\lambda_i^h < \lambda_i^e$) is in strong disagreement with the measured OFET mobilities shown in table 9. Since the predominance of n-type behaviour cannot be understood at a molecular structure level and requires also the analysis of the molecular packing, the transfer integrals of C3-NT4N (for which the crystal structure was determined and the XRD showed comparable thin film crystal packing) were calculated to gain an insight into the packing-charge transport relationships. The possible charge hopping pathways are shown in figure 35.

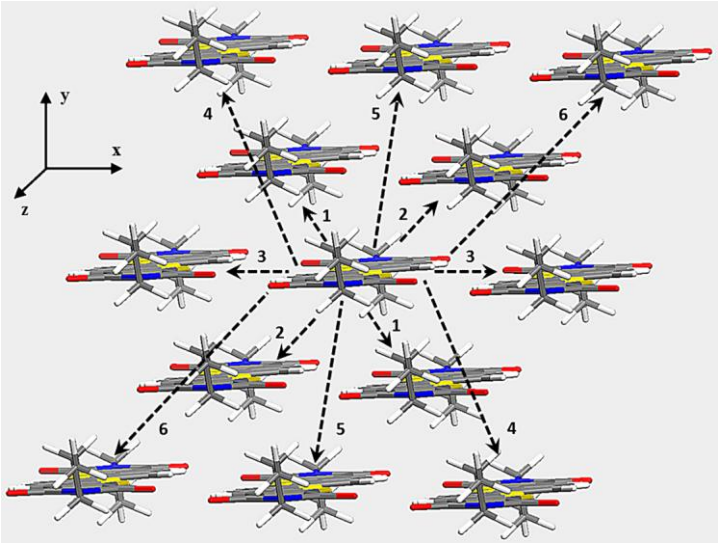

Figure 35. Charge hopping pathways schemes for molecule C3-NT4N in bulk crystal. y and z axis perpendicular and parallel to the molecular axis, respectively.

As shown from data in table 11, the highest electronic couplings are computed for the dimers involving first next neighbouring molecule pairs, namely pathways 1, 2 and 3. While all the three pathways show not negligible electron transfer integral values τ_e, on the contrary, only pathway 1 present a significant hole transfer integral τ_h.

Table 11. Computed charge transfer integrals τ for all the pathways having distances lower than 11 Å for molecule C3-NT4N.

Pathway	*r* [Å]	τ_h [meV]	τ_e [meV]
1	5.38	51.56	46.72
2	5.38	7.48	74.86
3	7.75	3.13	26.26
4	10.76	0	0.39
5	7.47	0.14	0.97
6	10.76	0.41	0.15

Displacements between molecules reported by *r*.

Therefore all the directions are favourable for electron transport while only one allows the hole transport. In table 12 bulk charge calculated (in a non-adiabatic hopping model, but details on the computed experiments are not reported herein) mobilities μ_{calc} are shown for a comparison with the experimental FET ones, μ_{OFET}.

Table 12. Charge mobilities for molecule C3-NT4N.

	μ_{OFET} [$cm^2V^{-1}s^{-1}$]	μ_{calc} [$cm^2V^{-1}s^{-1}$]	μ_{calc}* [$cm^2V^{-1}s^{-1}$]
Hole	$1.5x10^{-4}$	$1.15\ x10^{-1}$	$2.20x10^{-3}$
Electron	$2.4x10^{-1}$	$1.82\ x10^{-1}$	$2.13x10^{-1}$

Experimental OFET mobility μ_{OFET} and computed bulk mobilities μ_{calc} and μ_{calc}* obtained by considering all the pathways reported in figure 39 and excluding pathway 1, respectively.

The electron mobility shows a good agreement with experimental one, while the hole mobility dramatically overestimates the OFET one of about three order of magnitudes. This discrepancy may be ascribed to the different types of computed and experimental mobility. In fact, at the theory level the charge mobility is described by Brownian motion of charge carriers with no spatial constraints, while the experimental OFET mobility strictly depends on the source–drain potential tensor that means the device configuration (e.g. film orientation). Thus, while electrons can move along any crystal directions thanks to non negligible transfer integrals τ, hole transport is significantly high only along pathway 1 (table 11). If the device configuration forbids this pathway, even a damping of some orders of magnitude may become possible for hole mobility. In fact, as shown in table 12, by ignoring pathway 1, values of $\mu_{calc,e}$*= $2.13\cdot10^{-1}$ $cm^2/V\cdot s$ and $\mu_{calc,h}$*= $2.20\cdot10^{-3}$ $cm^2/V\cdot s$ are obtained, in much better agreement with the experimental OFET mobility.

As shown in table 9, the emission power signal of the device (taken as comparative parameter) slightly increases on increasing the tail length from C3 to C8, even if the thin-film quantum yields result almost comparable for all the synthesized materials. The EL spectra of compounds C3, C6,

C8-NT4N are shown in figure 36 and are similar to the PL ones (herein reported just for C8-NT4N, figure 34), demonstrating that the EL emission truly comes from the organic active layer. Figure 36 shows the movement of the emissive stripe inside the device channel by changing the applied bias, a typical feature of ambipolar OLETs also previously observed for other TBI-based materials including the first synthesized NT4N.

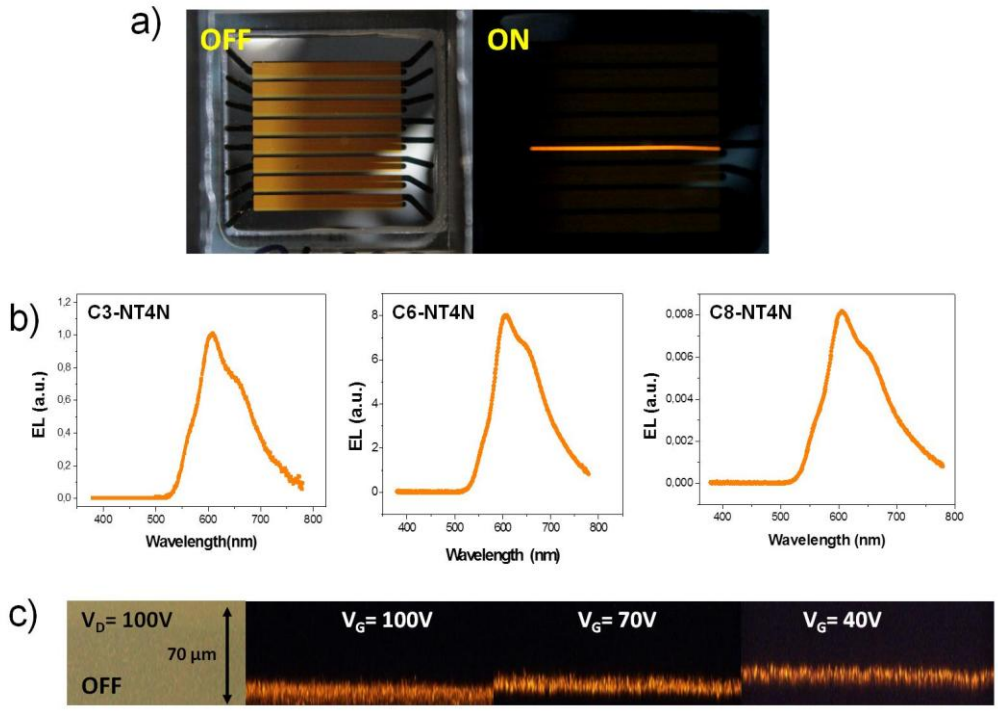

Figure 36. a) Images of a device in the OFF state and in the ON state showing light emission visible by eyes. b) Electroluminescence spectra of compounds C3, C6, C8-NT4N. c) Optical imaging of the emissive stripe motion in the channel achieved by tuning the gate voltage for compound C8-NT4N.

3.4.4 Conclusions

In conclusion by the N-alkyl end modification approach, contrarily to what generally observed for conventional oligothiophenes, evidences showed that different N-alkyl chains on TBI based materials afford no significant effects on the optical properties, thin films morphology and charge mobility. The major electron charge transport (mobilities up to 0.3 $cm^2/V{\cdot}s$) with respect to hole charge transport measured in OFET devices, was rationalized by theoretical calculations from single crystal structure, giving an insight on the structure-properties relationships in TBI materials. Tail dependent electroluminescence was instead observed, suggesting the potential key role of the

N-alkyl end of the TBI moiety for the selective modulation of the electroluminescence of these materials for ambipolar single layer OLET device applications.

3.5 Polymorphism in TBI based materials

As introduced in chapter 2, some TBI based materials showed a peculiar polymorphic behaviour. Generally, organic materials crystals are characterized by weak intermolecular interactions, π-π stacking, H-bonding etc., which allow one material to assume more than one form in the solid state. Polymorphism has been subject of intense research in the last few decades,[29] and several examples in organic materials field, have been reported for pentacene, rubrene and oligothiophene semiconductors, among the others.[30] Moreover, the opportunity to exploit polymorphism as an atom economic, properties-tuning tool is strongly emerging in the materials science scenario.[30, 31]

A dedicated study on the control of polymorphism in thienoimide based materials, by both synthetic strategy and post-synthesis treatments is herein reported and discussed.

3.5.1 Even/odd N-alkyl ends driven polymorphism

Surprisingly in our studies, the even/odd N-alkyl end symmetry has been found, and thus exploited, to induce and control conformational polymorphism in a series of 2,3-thienoimide based oligothiophenes (Cx-NT4N) in single crystal, powder and solution cast film.[32]

The molecular structure of the Cx-NT4N materials investigated is shown in chart 11.

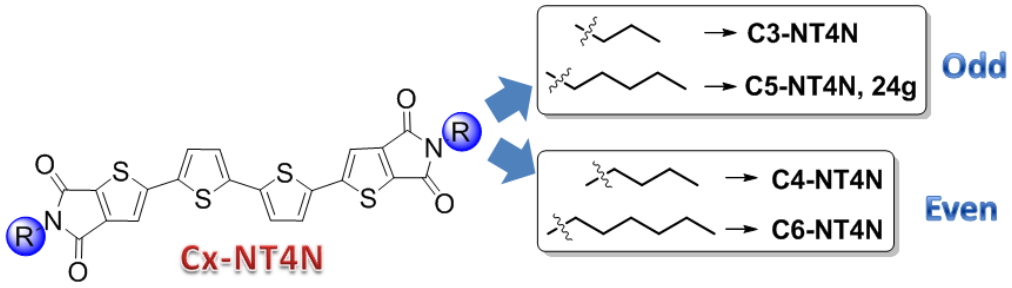

Chart 11. Molecular structure of even/odd Cx-NT4N materials (note: in this section the first material NT4N is named C4-NT4N).

Details on the synthesis are not reported since the procedure is the same described in section 3.4.1 (yield and characterization of material **24g** are reported in the experimental section), based on Stille cross-coupling reactions starting from the proper synthesized brominated thienoimide. Structure determination of even chain ended C4- and C6-NT4N revealed two possible polymorphic forms characterized by different molecular conformation and packing type. The thienoimide moiety can adopt both syn and anti conformation with respect to the adjacent thiophene ring. On the other hand, the two inner thiophene rings are always arranged in anti conformation, this

resulting in two possible polymorphs, i.e. anti-anti-anti and syn-anti-syn (figure 37a). The two conformational polymorphs adopt different molecular packing, namely phase A and phase B (figure 37b-c). In phase A, the molecules are piled in columnar stack and each Cx-NT4N strongly interacts through π–π stacking interactions with one molecule of the upper and lower layers. The interdigitation of these columns is favoured by the presence of C–H–O intermolecular interactions occurring between the thienoimide oxygen and one hydrogen of the alkyl layer of an adjacent molecule.

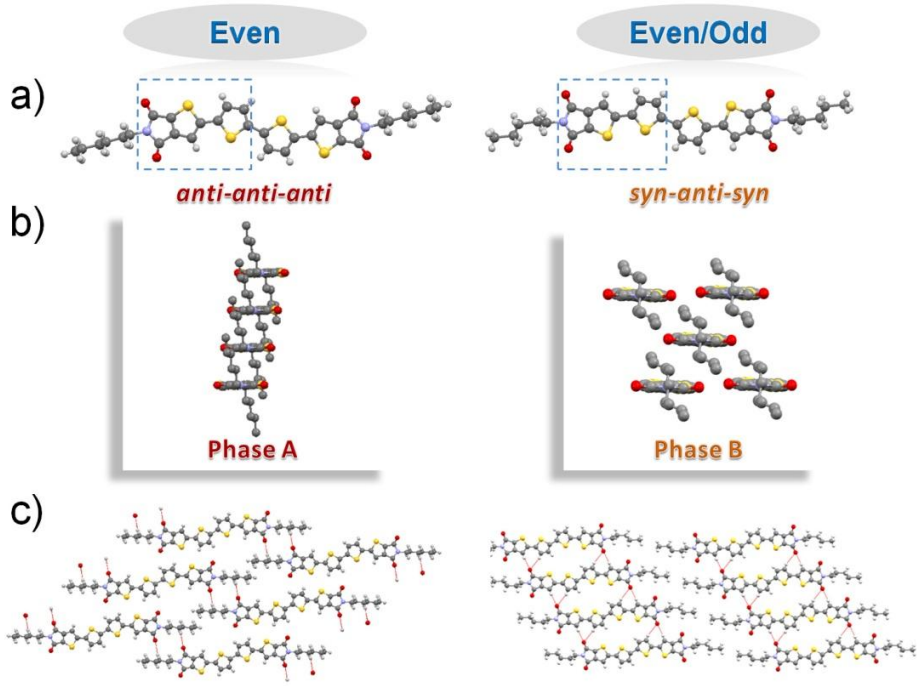

Figure 37. Left: C6-NT4N, right: C5-NT4N. (a) Molecular conformation, (b) a view parallel to the main molecular plane, (c) a view normal to the main molecular plane.

A different arrangement described as a brick wall was found in phase B in which Cx-NT4N interacts with four different close molecules and the packing results in a lower degree of interdigitation of the alkyl chains. In the syn-anti-syn conformers the oxygen of the thienoimide can interact with two hydrogen of the CH moiety of the syn-syn bithiophene framework of an adjacent molecule, promoting the alignment of the aromatic core. Surprisingly, odd chain ended C3- and C5-NT4N display exclusively the syn-anti-syn conformation and B-type packing only (figure 37, right).

Differential scanning calorimetry analysis (not reported herein) reveals only for even chain ended C4 and C6-NT4N a solid-solid transition compatible to the conversion of phase A to phase B. The DSC profile of C4-NT4N form A, taken as a representative case, is shown in figure 38a. The thermogram presents an endothermic peak at 185°C with an enthalpy of conversion $\Delta H_{A\rightarrow B}$ = 13 KJ/mol. This value is in good accordance with the conversion energy of about 14 KJ/mol (3

Kcal/mol) calculated by DFT calculations on the torsional barrier between conformer anti-anti-anti and syn-anti-syn (figure 38b).

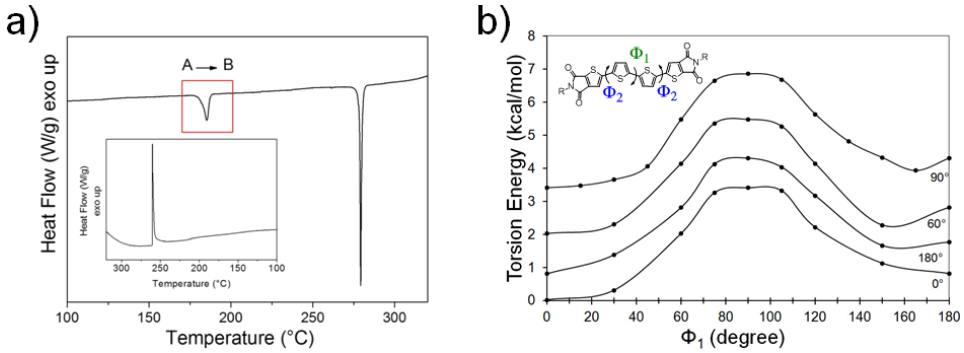

Figure 38. (a) DSC curve of C4-NT4N. The red square highlights the transition from phase A to phase B at 185°C (cooling profile in the inset). (b) Computed torsional energy for C4-NT4N in a vacuum as a function of the dihedral angle Φ_1, with Φ_2 fixed at the reported values.

Similarly C6-NT4N converts to form B at 136°C ($\Delta H_{A\rightarrow B}$ = 20 KJ/mol). The differences in $T_{A\rightarrow B}$ and $\Delta H_{A\rightarrow B}$ between C4-NT4N and C6-NT4N could be explained taking into account that the A→B conversion involves not only the conformation switch but also the conversion of the related packing type. No evidence of thermal transition compatible with conformational changes was found for odd chain ended C3- and C5-NT4N compounds.

The polymorphism behaviour of even ended systems C4- and C6-NT4N was also investigated in their solution cast films on silicon substrates. Figure 39a shows the fluorescence microscopy image of thin deposits of C4-NT4N at room temperature (top) and after the thermal cycle rt→200°C→rt (bottom).

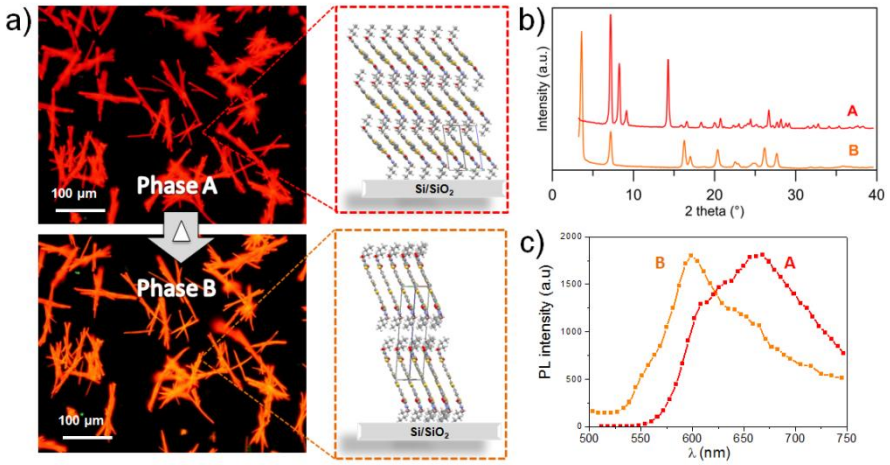

Figure 39. C4-NT4N: (a) fluorescence microscopy images of a thin deposit of C4-NT4N on Si/SiO_2 substrates at rt (top, phase A) and after the annealing (bottom, phase B), in the inset molecular organization and packing in thin deposits. (b) XRD patterns of the thin deposits before and after the thermal cycle and (c) corresponding confocal fluorescence spectra.

After solvent evaporation C4-NT4N forms needle shaped microcrystals, whose size ranges between 50 and 200 μm, which exhibit a strong red fluorescence at FM. The XRD profile (figure 39b, red curve) shows a very good fit with phase A observed for single crystals, indicating that the solution casting preferentially leads to the phase A. Interestingly, for vacuum evaporated films of the same compound and all the other alkyl ended derivatives only the phase B was found. Accordingly, space resolved fluorescence spectra taken by confocal microscopy show maximum intensity emission at about 670 nm (and a minor broad peak at 630 nm, figure 39c, red curve). The thermal annealing conversion of phase A to phase B was confirmed by XRD analysis (figure 39b) and by LSCM showing a blue shifted emission (figure 39c, orange curve), which displays a peak at 600 nm with a shoulder at 650 nm. As expected from XRD and DSC data, thermal treatment performed on odd-chain C3-NT4N thin deposits (rt→275°C→rt) did not lead to appreciable changes in fluorescence emission (results not reported herein).

This peculiar even-odd effect requires further dedicated efforts to shed light on the relationships between molecular conformation, molecular packing and alkyl end symmetry for a larger library of compounds. This strategy represents a straightforward and effective way to reduce the need of molecular variability and synthetic efforts aimed at the tailoring of packing-related functionalities, included charge transport and electroluminescence properties in device.

3.5.2 Polymorphic morphology of NT3N and its application in Time Temperature Integrator device

When deposited on a surface, NT3N material (introduced in section 3.3) exhibited a strong tendency to form crystals, whose size and shape depended on the experimental procedure and the solvent. Thin deposits of NT3N were prepared by drop-casting on Si/SiO_2 substrates from both toluene (high boiling point) and chloroform (low boiling point).

Besides showing an extraordinary tendency to crystallize, never observed in conventional terthiophene based compounds, it also shows polymorphic behaviour, with two types of crystal morphologies, yellow fluorescence fiber-like and green fluorescence platelet-like crystals (figure 40).

When deposited from toluene in air, NT3N shows the two polymorphic fiber-like and platelet-like crystals, with the platelets about 75% (estimated value) of the total. The platelet like crystals

exhibit the typical regular shape expected from the crystals with well-defined angles, with range size between 1 µm and >500 µm and with a length/width ratio ranging between 1:2 and 1:5.

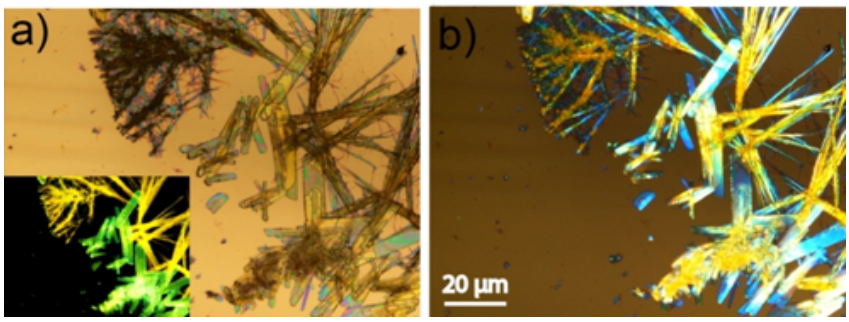

Figure 40. a) Optical micrograph of NT3N drop cast thin deposit (toluene 1 mg/ml on Si/SiO_2 wafer). The inset shows the same area under UV illumination. b) Micrograph obtained by cross polars.

On the contrary, the fiber-like crystals appear as long fibers (>1 mm) randomly distributed on the surface. Their width ranges between a few µm and 100 µm resulting in a ratio length/width ranging between 1:5 and >1:10. While the fiber-like crystals tend to be concentrated at the centre of the droplet, the platelets were mainly located at the boundaries of the droplet, where more material is concentrated and the solvent tends to evaporate slowly (coffee still effect).[33]

When NT3N is deposited from chloroform solution in a vapour-saturated environment, which shrank more than 2 times faster than toluene in air, a significant quantity of platelets is still observed (~60%, estimated value) but with a mean size reduced to few micrometres. Moreover, if the same solution is deposited in air, where the shrinking rate is about 10 time faster than toluene, the fibers represent more than 95% of the total. Thus, fibers are kinetically favoured while platelets represent the most thermodynamically stable phase. Reducing the concentration, the mean size of the crystals tends to be proportionally reduced.

Both platelet-like and fiber-like structures show birefringence under POM (figure 40b). The platelet-like crystals appear homogeneously coloured, indicating an almost constant thickness over the entire stripe, and extinguish in four positions at intervals of 90° when the polarizers are oriented 45° with respect the longer axis. The occurrence of light extinction at the same orientations in all positions of each crystal suggests the same orientation of growth of the crystalline domains or their single crystal nature. On the other hand, the fiber-like crystals appear multicoloured and they don't extinguish at any directions, a behaviour suggesting the polycrystalline nature of such structures. Strong fluorescence was observed from both fiber-like

crystals (yellow emission at room temperature) and platelet-like crystals (green emission) (inset in figure 40a and figure 41b).

To gain an insight on the morphology-dependent fluorescence of NT3N thin deposits, X-Ray diffraction (XRD) and laser confocal scanning microscopy (LSCM) were performed on samples containing a majority of fibers (yellow emission) or a majority of platelets (green emission). Low-angle XRD analysis revealed two different diffraction profiles with the main peak at an angle corresponding to interplanar distances of 2.2 nm (green profile, figure 41a) and 2.1 nm (orange profile, figure 41a) for films of NT3N containing a majority of platelets or fibers respectively. As confirmation, in a film showing both type of crystals both sequences of reflexes can be found (blue profile, figure 41a).

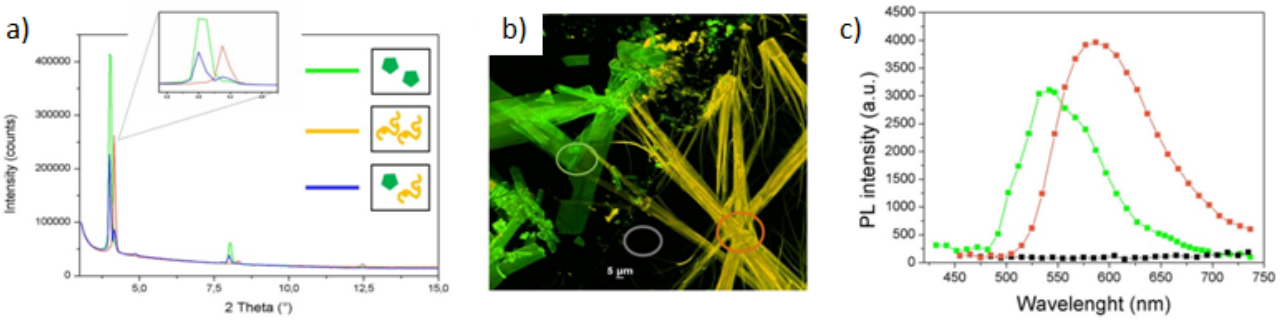

Figure 41. a) Diffraction patterns of three different films on a Si/SiO_2 having a majority of platelet crystals (green curve) or fibers (yellow curves) and of a mixture of the two crystals (blue curve). b) Confocal fluorescence microscopy images of NT3N crystals and fibers, the image is a merge of fluorescence collected with two PMT with bandpass filters 525/50 nm and 595/50 nm. c) PL spectra measured for the background region (black), the platelet-like crystals (green) and the fiber-like crystals (orange), indicated in b) by the circles.

The confocal microscopy image of platelets and fibers of NT3N is shown in figure 41b and the corresponding PL spectra obtained from the different regions evidenced by circles, is shown in figure 41c. PL spectra confirm the FM image showing an emission centered at 542 nm for the platelets and at 585 nm for fiber-like crystals.

Interestingly, a thermal treatment allows to achieve control over the morphology and emission frequency of the thin deposits (figure 42). Heating the sample up to 200°C followed by cooling down to rt does not affect the emission features since both green and yellow emission are preserved (figure 42 path b). However, if the sample is heated over the melting point (K→LC, 200°C<T<205°C) or up to the clearing point (LC→L, 205°C) and then recrystallized, the yellow emission will be irreversibly lost (figure 42 path c and d). Moreover, while platelet-like crystals almost preserve their shape upon heating beyond 200°C, the fiber-like crystals become irreversibly

larger (about +20% in size) and flatter. By crystallizing the melt (>205°C→rt) all the droplets solidify forming large crystals originating by the coalescence of the liquid droplets.

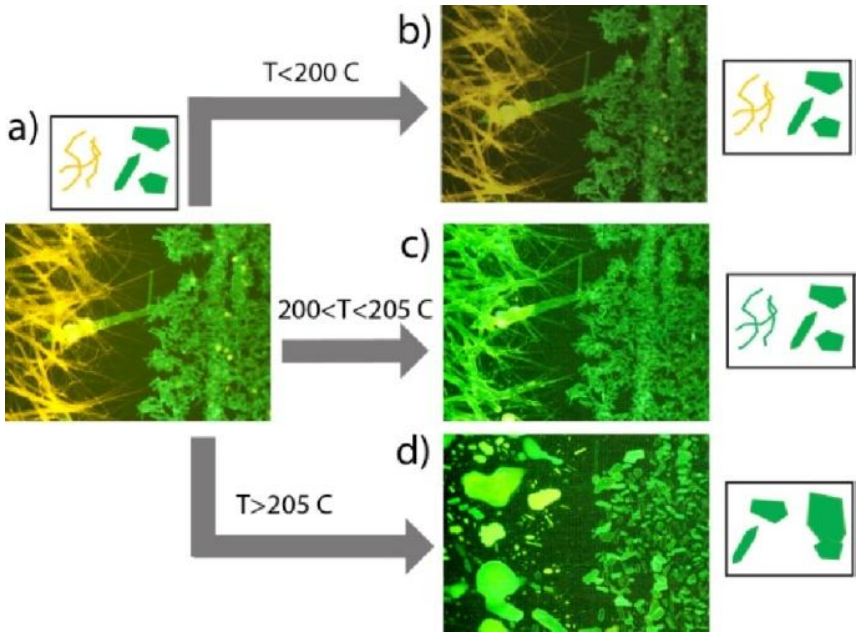

Figure 42. Sketch of the thermal processes to control the emission features of NT3N crystals. a) cast film at rt. The images show the same area of the thin deposit b) after heating up to 200°C and cooling down to rt; c) after heating at temperature between 200 and 205°C and cooling down to rt and d) after melting and slow cooling to rt.

The polymorphic behaviour (usually considered detrimental for applications in OFETs, OLEDs and OLETs) found in NT3N, has been exploited to fabricate a device named time temperature integrator (TTI), i.e. an electronic device capable of recording the thermal history of one system.[34] The development of TTIs represents a matter of high interest for the traceability of perishable products, whose temperature must be maintained throughout a shipping or life cycle (e.g. food, drugs, but also some electronic devices). To date, the most reliable TTIs are based on electronic sensors which present high cost and complexity limiting their large-scale industrial production, or on systems efficient for a single threshold temperature but not for monitoring a larger spectrum of temperatures.[35] In this present case, the temperature dependence of fluorescence together to the highly processability of NT3N in solution, made it an ideal candidate for TTI applications.

The TTI was built by patterning a data matrix made of micrometric structures of NT3N on silicon substrates (figure 43a). In particular, a logic pattern containing information in a binary code formed by micrometer-size pixels detectable by a conventional optical microscope has been fabricated. The targeted pattern presented a regular distribution of holes with 18x18 μm^2 lateral

size and 1 µm depth (pixels) on a substrate of SiO_2. Thin deposits were obtained by drop casting a chloroform solution of NT3N on the patterned substrate (20 µl/cm^2) in air. As the solvent shrank and its volume became comparable with the volume of the pixels, the solution remained preferentially constrained in correspondence of the pixels due to the higher surface tension. When the solution reached the supersaturation it precipitated into the pixels, forming a perfectly regular pattern. With a solution of concentration 2< c <4 mg/ml all pixels were completely filled by NT3N while with a lower concentration, the material was inhomogeneously distributed inside the pixel and accumulated at the pixel corners.

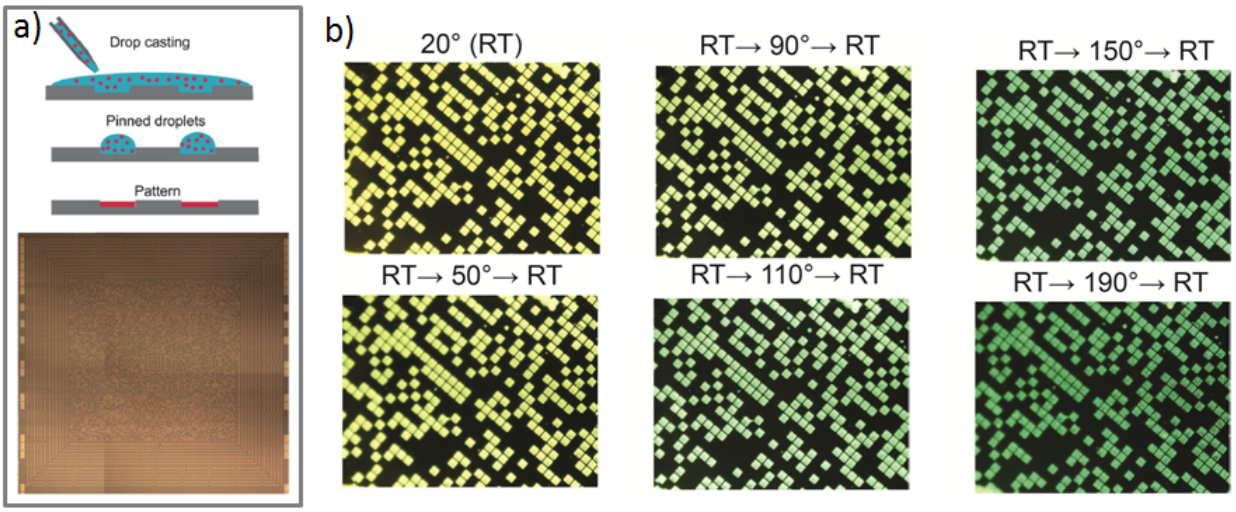

Figure 43. a) Scheme of the drop-cast based process, with the optical micrograph of the pattern representing a data matrix (total size of the matrix 3x3 mm^2, each pixel 18x18x1 µm^3). b) Fluorescence colour of the pattern evolution as a consequence of an irreversible phase variation driven by the temperature.

In figure 43b an image of the pattern employed, formed by polycrystals with yellow colour under FM (figure 43b, RT) is shown. Heating the sample, a progressive change of the fluorescence colour from yellow to green in the temperature range 20-200°C is observed, and by keeping the heating temperature constant for more than 30 s, the change becomes irreversible.

In conclusion, two usual drawbacks for technological applications, such as polymorphism and recrystallization have been successfully exploited for the fabrication of a TTI working on the different response of a single active material in an impressive range of temperatures. The feasibility of the approach by a simple fabrication method and the easy processing of the TBI based material, combined with the possibility of monitoring the device by optical techniques, make this approach appealing for the development of new generation low-cost TTIs.

3.5.3 Polymorphism control by unsaturated bridges insertion in TBI based systems

Inner constraints were introduced into the π-conjugated core of TBI based compounds in order to investigate their effect on molecular conformation and overall aromaticity and thus on the functional optoelectronic and morphological properties of the obtained materials, polymorphism among the others. Three new 2,3-thieno(bis)imide ended oligothiophenes bearing unsaturated ethylene (E), azomethine (I) and ethinyl (A) inner bridges (named NTE **30**, NTI **31** and NTA **32** respectively, depicted in chart 12) have been synthesized and characterized.[36]

From literature, it is known that ethylene bridge insertion in oligothiophenes is associated to a reduced band gap derived from enhanced molecular planarity and a lower overall aromatic character than oligothiophenes containing the same number of sp^2 carbons.[37] Similarly, an azomethine bridge promotes an even greater bathocromic effect and has also been investigated as a structural tool to tune the electronic properties of oligothiophenes.[38] Contrarily, the main effect observed for acetylenic bridged oligothiophenes with respect to their fully sp^2 carbon based π-conjugated analogues is an increased band gap originating from the mismatch of the sp carbon orbitals with the π-delocalized system.[39] The effect of the unsaturated bridges in NTE, NTI and NTA on the functional properties has been evaluated and compared to those of conventional oligothiophenes or to the bridge-free NT4N.

Chart 12. Molecular structure of materials NTE **30**, NTI **31** and NTA **32**.

Scheme 9 displays the synthetic route to NTE (**30**). The material was prepared starting from commercial 2-thiophenecarboxaldehyde **33**. Compound **33** was converted into (E)-1,2-di(thiophen-2-yl)-ethene **34** in a McMurry coupling involving a low-valent titanium reagent prepared from $TiCl_4$ and Zn°, in boiling THF according to an already reported procedure leading to the E isomer as major product (Y = 57%).[40]

Compound **34** was then bis-stannylated under conventional conditions (*n*-BuLi, Bu_3SnCl, THF) to give derivative **35** in 98% yield. A subsequent classical Stille cross-coupling with syntesized brominated thienoimide **28c** afforded the target NTE in 57% isolated yield after purification by flash chromatography on silica gel and a following crystallization from hot toluene.

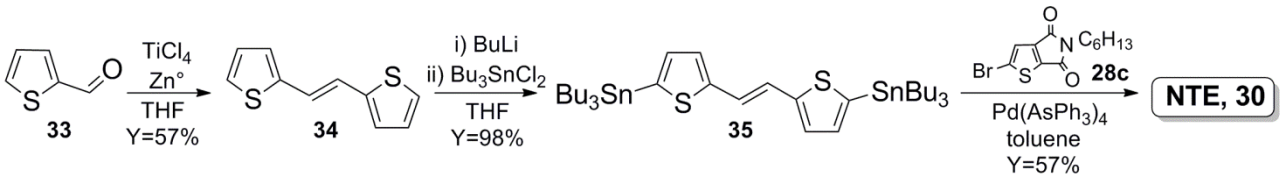

Scheme 9. Synthesis to the target compound NTE.

The synthesis of NTI (**31**) required a longer procedure, which is depicted in scheme 10.

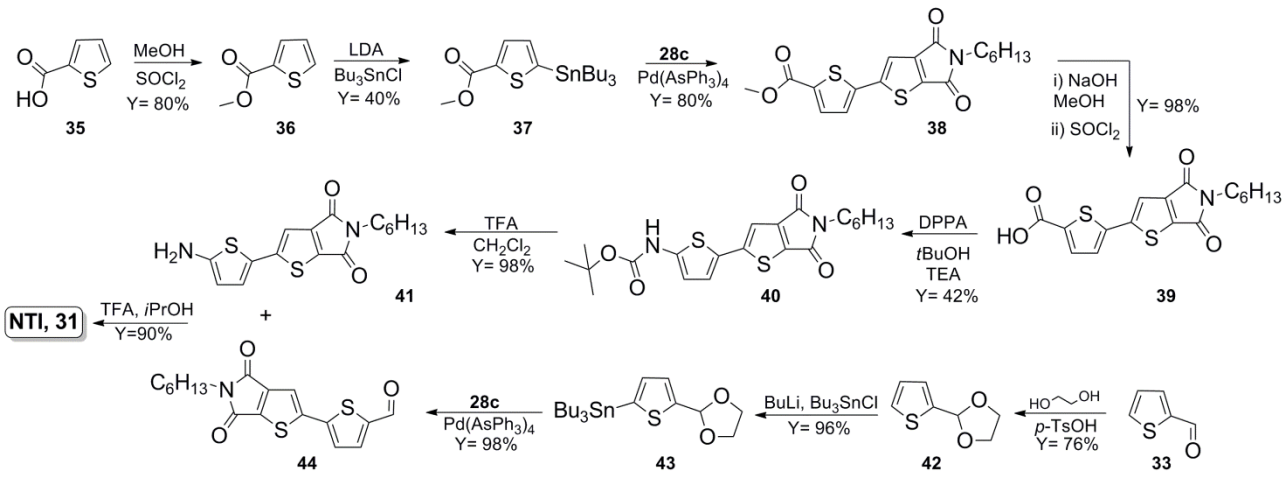

Scheme 10. Synthetic route to NTI material.

The target material was obtained in nearly quantitative yield by forming the imine bridge between the dimeric compound **41**, bearing an amino end group and the formyl ended dimer **44**.

Firstly, 2-thiophenecarboxylic acid **35**, was protected as methyl ester (**36**) in 80% yield and then stannylated under classical conditions with lithium diisopropylamide (LDA) and Bu_3SnCl to give derivative **37** in 40% yield. A $Pd(AsPh_3)_4$ catalyzed conventional Stille cross-coupling reaction between **37** and the brominated 2,3-thienoimide **28c** gave the dimeric species **38** in 80% yield. The hydrolysis of the methyl ester occurred by treating compound **38** with NaOH, and by reacting the resulting crude with $SOCl_2$. Besides hydrolyzing the ester, the strongly basic treatment also opened the thienoimide ring, so $SOCl_2$ was used in order to dehydrate the intermediate and thus close again the thienoimide, giving compound **39** in a semi-quantitative yield. By using diphenyl phosphoryl azide (DPPA), compound **39** was then converted into its azide derivative, which underwent Curtius rearrangement to the corresponding isocyanate. Since the reaction was carried out in the presence of *tert*-butanol, the final product of this synthetic step was the corresponding *tert*-butyl carbamate **40**. This compound was obtained in 42% yield and converted to compound **41** by TFA treatment (99% yield).

Conversely, dimer **44** was prepared starting from 2-thiophenecarboxaldehyde **33** that was first protected as acetale by using ethylene glycol in the presence of p-toluenesulfonic acid and then stannylated (*n*-BuLi, Bu_3SnCl, THF) to give the organotin derivative **43**.[41] Then, a Stille cross-coupling reaction catalyzed by in situ prepared $Pd(AsPh_3)_4$ between compound **43** and the synthesized brominated thienoimide **28c** gave dimer **44** in almost quantitative yield (Y= 98%). Finally, the two dimeric species **41** and **44** were coupled[38a] in *i*-PrOH in the presence of catalytic amounts of TFA to give the target azomethine functionalized NTI **31** in 90% of isolated yield after purification. This synthetic route generally led to the trans isomer. Accordingly, DFT calculations show a good match between experimental and calculated HOMO and LUMO energy levels for the trans isomer (table 1) (in fact HOMO and LUMO energy levels for the cis isomer are shifted by about 0.10 eV (-5.81 eV and -3.46 eV).

In scheme 11 is described the synthetic way to NTA (**32**) material.

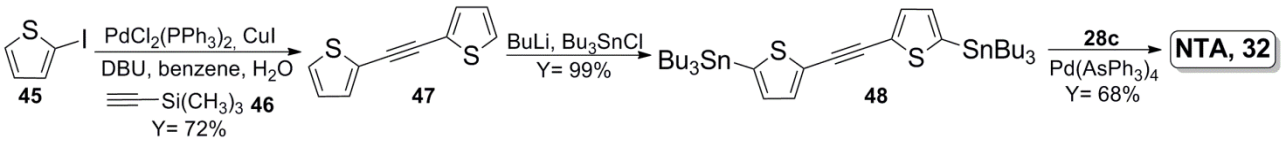

Scheme 11. Synthesis of NTA.

NTA (**32**) was synthesized in a three-step synthetic protocol starting from commercial 2-iodothiophene **45**. Compound **45** was made react with trimethylsilylacetylene **46** in a modified Sonogashira coupling affording the bithiophene derivative **47** in 72% yield by following an already reported procedure.[42] After a stannylation reaction to achieve compound **48** in semi-quantitative yield, a Stille cross-coupling catalyzed by $Pd(AsPh_3)_4$ between stannilated derivative **48**[43] and the brominated thienoimide **28c** provided the target material NTA in 68% yield after purification by flash chromatography on silica gel and subsequent crystallization from hot toluene.

The electronic properties of the three synthesized materials were investigated by combined optical, electrochemical and theoretical analysis and compared to those of a reference 2,3-thieno(bis)imide bridge-free system having the same number of thienyl rings, named C6-NT4N (see previous section).The data are summarized in table 13.

Table 13. Optoelectronic properties of the synthesized compounds NTE, NTI and NTA. [a]Excitation at the maximum absorption wavelength.

Compound	λ_{abs} (nm)	λ_{em} [a] (nm)	$E°_{ox}$ (V)	$E°_{red}$ (V)	HOMO (eV) exp/th	LUMO (eV) exp/th	E_g (eV) exp/th
C6-NT4N[b]	451	568	-	-	-5.69[c]/-5.77	-3.16[c]/-3.34	2.53/2.44
NTE	465	588	1.17, 1.41[d]	-1.21	-5.54/-5.57	-3.16/-3.21	2.38/2.36
NTI	471	544	1.28[d], 1.43[c]	-1.09, -1.49	-5.65/-5.73	-3.28/-3.36	2.37/2.37
NTA	433	547	1.46[e]	-1.20	-5.83/-5.74	-3.17/-3.27	2.66/2.46

[b]Taken from ref. 26 and corrected by CH_2Cl_2/H_2O liquid junction. [c]No difference between butyl and hexyl ends is expected. [d]Half-wave potential. [e]Peak potential at 0.1 $V \cdot s^{-1}$.

Absorption spectra (figure 44a) show a red shift of the absorption maxima from 433 nm to 465 nm and to 471 nm on going from NTA to NTE to NTI. On the other hand, the emission maximum of NTE (588 nm) is strongly red shifted with respect to those of NTA (547 nm) and NTI (544 nm). Similarly, a strong red shift of both absorption and emission is observed for NTE and NTI in comparison to C6-NT4N (465 nm, 471 nm vs. 451 nm for C6-NT4N) while a blue shift is observed for NTA with respect to C6-NT4N (433 nm vs. 451 nm). This behaviour can be ascribed to the lower overlap with the π-conjugated system of the (sp) C≡C than that achieved by (sp^2) C=C and C=N moieties. Regarding emission spectra, NTE emission is red-shifted with respect to C6-NT4N (588 nm vs. 568 nm), NTI and NTA compound. The quantum efficiencies (PLQY) in solution were also measured. NTE and NTA displayed comparable PLQY, i.e. 19% and 20%, respectively, while a lower value was found for NTI (2%).

Cyclic voltammetry analysis results are reported in figure 44b and table 13. The voltammogram of NTE shows two quasi-reversible oxidation waves (1.17, 1.41 V vs. SCE) and a reduction one centred at -1.21 V. The replacement of ethylene by azomethine induces the shift of the first oxidation wave that partially overlaps the second one generating an irreversible process.

On the other hand, the reduction wave shifts to less negative potentials (-1.09 V) and a second reduction process appears into the electrochemical window (-1.49 V) indicating the possibility to host two electrons in the LUMO. Finally, NTA not only shows an irreversible oxidation wave shifted to the highest potential (1.46 V), but also a quasi-reversible reduction wave at the potential characteristic of the TBI moiety (about -1.2 V).

The HOMO energy levels decrease in the order NTE > NTI > NTA. On the other hand, the LUMOs of NTE and NTA have almost the same energy, but that of NTI is about 0.1 eV lower, likely due to the electron withdrawing effect of the azomethine moiety. In agreement with the spectroscopic data, the energy gap (E_g) of NTA is significantly larger than that of NTE and NTI.

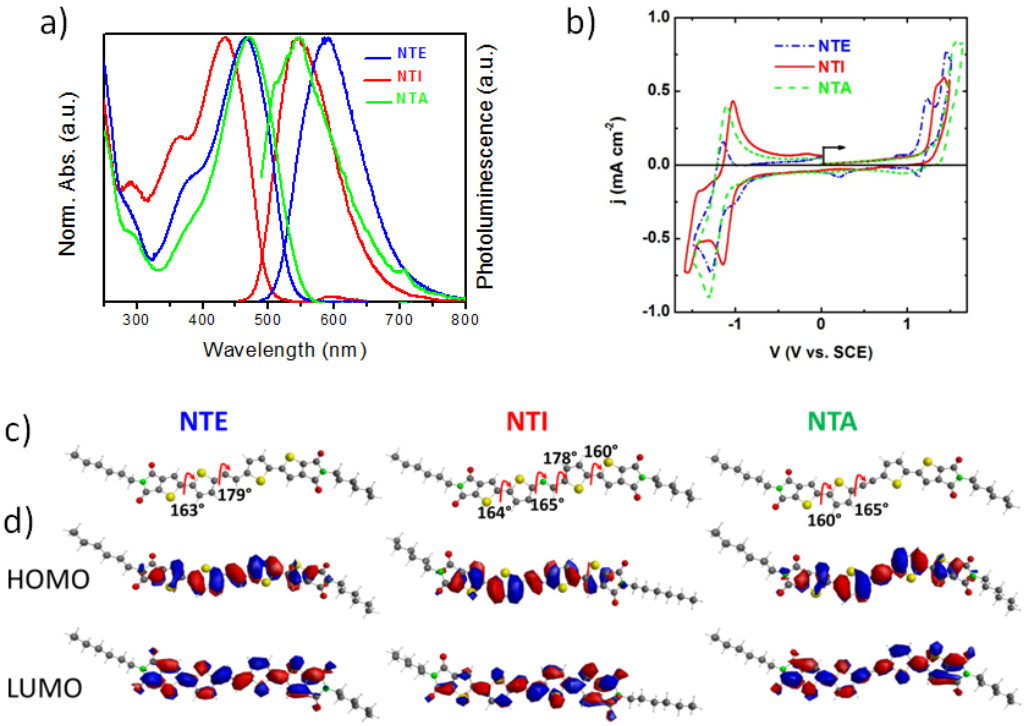

Figure 44. a) UV-Vis and PL spectra of the three synthesized materials NTE, NTI and NTA in CH_2Cl_2. b) voltammograms in CH_2Cl_2 0.1 mol·l^{-1} $(C_4H_9)_4NClO_4$ of the three compounds (1 mmol·l^{-1}). c) molecular structures with dihedral angles and d) frontier orbitals isodensity plots and energy values of NTE, NTI, NTA.

To gain an insight on the optoelectronic properties, theoretical calculations were performed (figure 44c-d). Firstly, the most stable molecular conformation and the HOMO and LUMO energy levels and charge distribution of the new compounds were investigated by DFT calculations. All the molecules adopt an almost planar conformation with dihedral angles between the TI moiety and the inner thiophene ring of about 160° and between the thiophene ring and the inner spacer of about 180° (NTE) and 165° (NTA). While NTE and NTA are centrosymmetric (Ci point group), NTI is non-centrosymmetric because of the azomethine spacer (figure 44c). This results in an asymmetric set of dihedral angles and in a charge distribution of frontier molecular orbitals. In NTE and NTA, the HOMO orbital is homogeneously distributed over the inner conjugated thiophene rings, while the LUMO orbital extends also to the electron deficient thienoimide units (figure 44d), in agreement with what is generally observed for TI-ended systems as the reference C6-NT4N compound. On the contrary, for the nonsymmetric NTI molecule, the LUMO is mainly localized on the thienoimide unit of the NC-bound molecular branch. DFT calculations, in agreement with experimental data, show a lower band gap for the NTE and NTI with respect to C6-NT4N. On the other hand, NTA shows a higher band gap and a significant shift of the HOMO level, likely due to a

lower overlap of the sp carbons with the π-conjugated system, while the LUMO levels are much less affected by the unsaturated bridges since they are mainly located on the 2,3-thienoimide groups. This behaviour is in good accordance to that observed for ethylene,[37a] azomethine[38] and acetylene[39] bridged oligothiophenes without 2,3-thienoimide end groups.

Thin deposits of NTE, NTI and NTA, were grown by drop casting on silicon and glass surfaces in air. When deposited on a surface, all compounds exhibited a strong propensity to form large crystals. All thin deposits exhibit crystalline microstructure with strong birefringence under polarized optical microscopy and an intense photoluminescence. Interestingly, concomitant polymorphs with markedly different fluorescence colour emission were clearly evident for all compounds (figure 45, top).

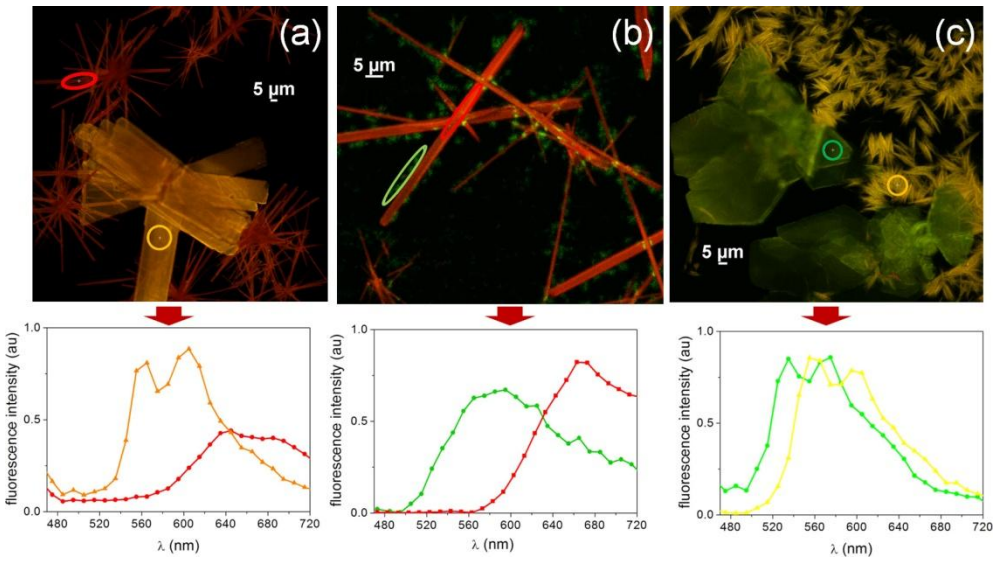

Figure 45. Fluorescence confocal images of the films of a) NTE, b) NTI, and c) NTA obtained upon evaporation of 0.5 mg/ml toluene solutions on glass. Top: images are a merge of the fluorescence collected on three PMT with bandpass filters 525/25 nm, 595/50 nm and 700/70 nm. Bottom: confocal fluorescence spectra collected for ROI indicated by the circles.

When deposited from toluene, NTE forms a mixture of rod-like and platelet-like crystals (figure 45a, top, red emitting and orange emitting polymorphs, respectively). Rod-like crystals appear as long crystallites (≤100 µm) randomly distributed on the surface with a width ranging from 5 µm to 10 µm. Platelet-like crystals show a regular shape with a long axis from 20 µm to 100 µm (a rod-like majority was obtained from the saturated solution, while a platelets-like majority from the diluted solution). Both polymorphs exhibit a strong birefringence under POM with the characteristic behaviour of optically anisotropic materials with extinction at precise orientations (rod-like crystals extinguish when the polarizers are oriented parallel or perpendicular to the long

axis of the crystal, while platelets-like crystals extinguish when the polarizers are oriented along parallel or perpendicular directions to the border of the crystal). The evidence of light extinction at the same orientations in each crystal implies that they are either single crystals or formed by iso-oriented domains.

Fluorescence spectra of NTE performed by confocal microscopy (figure 45a, bottom) show a luminescence spectrum peaking at 640 nm for the rod-polymorph and two emission peaks at 560 nm and 600 nm for the platelet polymorph. The polymorphic nature of platelets- and rod-like crystals was confirmed by XRD analysis carried out on samples specifically prepared in different conditions in order to strongly enhance the presence of one of the two forms. Rod- and platelets-like crystals show different patterns with the most intense peaks at 6.1°, 18.3° and 24.5° for the former and at 2.7°, 5.4°and 8.1°for the latter (figure 46).

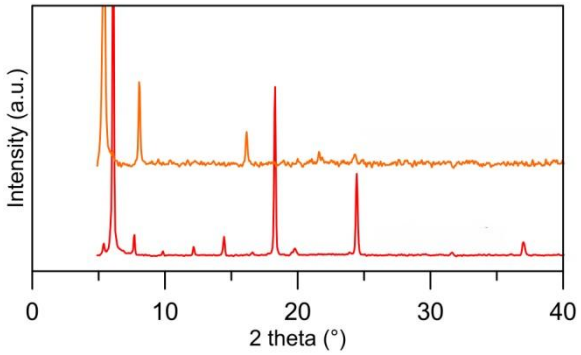

Figure 46. XRD profile for rod-like (red) and platelet-like crystals (orange) of NTE material.

NTI deposits (figure 45b, top) show needle shaped crystals (red emission colour, length < 500 mm) randomly distributed on the surface. Their width ranges from 10 µm to 100 µm resulting in an aspect ratio (length/width) between 1 : 5 and 1 : 50. Occasionally, some small aggregates (green emission colour, size < 2 µm) appear on the surfaces decorating the rod-like crystals. Crystals exhibit a strong birefringence under POM with the typical behaviour of optically anisotropic materials with extinction at precise orientations meaning that they are either single crystals or formed by domains oriented in the same direction. The fluorescent image (figure 45b, bottom) shows a strong red emission peaked at 660 nm from rod-like crystals, while the decorating aggregates emit in the green region.

Furthermore, NTA films show two polymorphs, i.e. fiber-like (yellow emission colour) and rhombohedral (green emission colour) crystals (figure 45c, top). The rhombohedral crystals show extinction when the long axis of the crystal is oriented 45 with respect to the polarizers, typical behaviour of optically anisotropic materials. The fiber-like crystals exhibit a strong birefringence,

but they appear multicoloured and do not extinguish at any directions, indicating their polycrystalline nature. Both polymorphs exhibit a strong fluorescence (figure 45c, bottom) with two peaks at 535 and 575 nm for the crystals and two maxima at 560 and 600 nm for the bundle of fibers.

The emission of all compounds in thin deposits was also investigated by conventional PL spectroscopy indicative of the macroscopic film (spectra not reported herein). According to the space resolved PL spectra (figure 45, bottom), red shifted emission was observed for NTE and NTI with respect to NTA. The PLQY for NTE and NTA thin deposits was 6% and 10%, respectively, thus lower than those observed in solution, and 4% for NTI.

DFT calculations were exploited to tentatively explain the origin of the observed polymorphism. In particular, the possibility of conformational polymorphism was considered. The conformation energy plot computed by varying the dihedral angle (θ) between the thienoimide moiety and the inner thiophene ring (figure 46) shows two minima corresponding to the anti and the syn conformers with a small energy difference (about 2 kcal·mol^{-1}). The conformation energy plot has been obtained from single point calculations starting from the optimized geometry at varying the dihedral angle between 2,3-thienoimide moiety and the inner thiophene ring and keeping the symmetry point group (resulting in concomitant rotation of two symmetric dihedral angles).

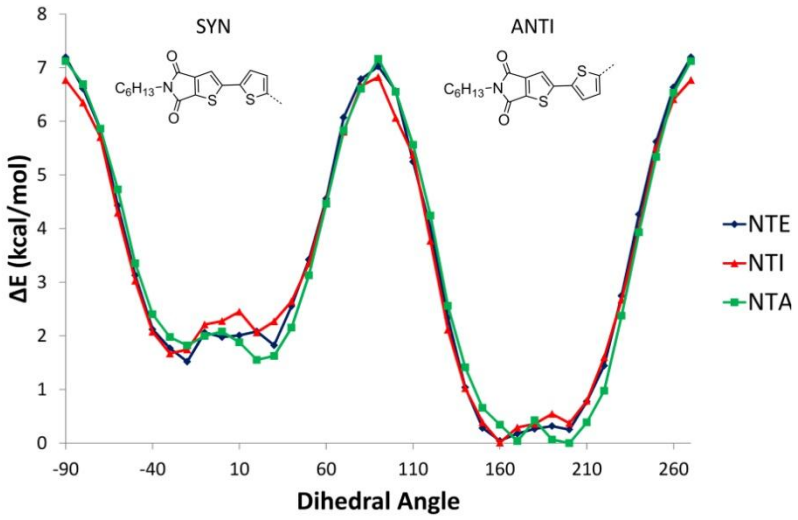

Figure 46. Conformation energy plot as a function of the dihedral angle between the thienoimide end moiety and the inner thiophene ring.

This, in combination with the already observed crystallization of thienoimide-based molecules in both anti and syn forms, suggests that the observed concomitant polymorphs might be due to the crystallization of both conformers. Moreover, calculations were exploited to investigate the effect of the aromaticity variation, induced by the unsaturated bridge substitution, on molecular π-

stacking, through the computation of the overlap integrals S_h and S_e for HOMO and LUMO orbitals, respectively. The overlap integrals were computed for a molecular pair, 4 Å-spaced perpendicular to molecular axis. A dramatic decrease in the LUMOs overlap is observed for all the synthesized molecules bearing the unsaturated bridge NTE, NTI and NTA (381, 588 and 283 meV respectively) with respect to C6-NT4N (767 meV). In particular, as expected, NTA, having the acetylenic spacer and the most reduced aromatic character, shows the worst LUMO overlap. A reduced effect is observed for NTE, NTI and NTA HOMOs overlaps (702, 599 and 688 meV) that, however, are lower with respect to C6-NT4N one (707 meV). These preliminary calculations confirm that decreasing the aromaticity of the molecules may cause a decreasing of the intermolecular interactions.

The behaviour of thin deposits upon thermal annealing was explored for all compounds. Figure 47a-b shows the fluorescence microscopy images of NTE films before and after the thermal cycle rt→200°C→rt.

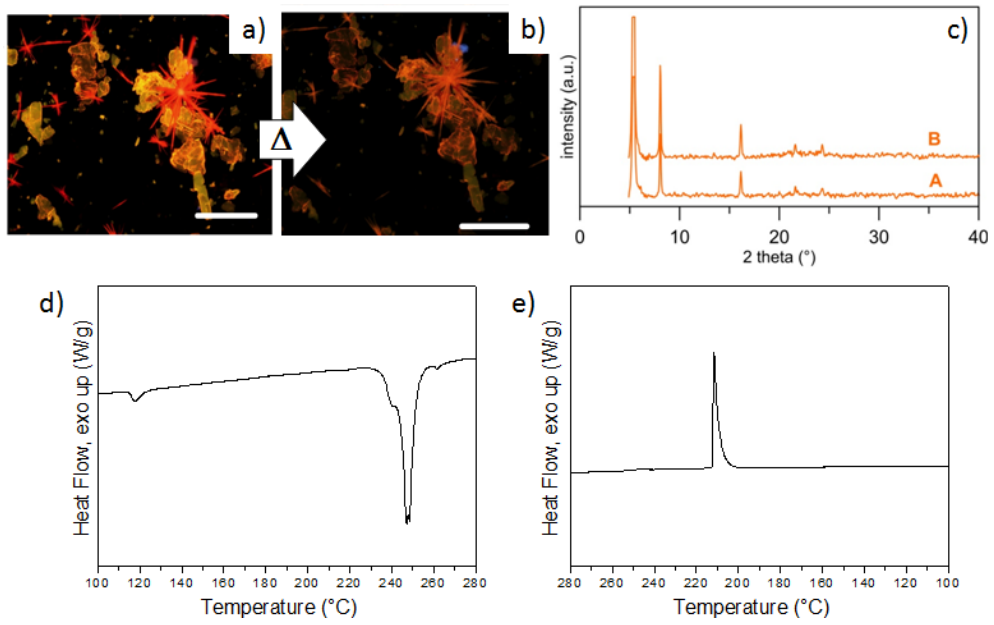

Figure 47. a) Fluorescence microscopy image of a drop-cast thin deposit of NTE (toluene 1 mg/ml on Si/SiO_2 wafer; scale bar 100 µm). b) The same image after thermal treatment of the sample at 200°C for 30 s. c) XRD profile of the same sample of figure 46 after thermal cycle. The B curve is that of the platelet-like crystals shown in figure 43. d-e) Thermograms of d) heating and e) cooling, of NTE under nitrogen atmosphere (20°C/min). This sample is mainly formed by rod-like crystal phase.

Upon thermal annealing, the two polymorphs of NTE exhibit a different behaviour. While the platelet-like crystals persisted till the melting point (~260°C, DSC, figure 47d-e), the rod-like crystals showed an irreversible change of the emission, that progressively changed from red to orange, which corresponded to the emission of platelet-like crystals. The transition is observed

also in the DSC curve of the rod-like crystals which presents an endothermic peak at ~120°C, corresponding to the solid-solid transition at the platelet-like crystal phase. The transition was irreversible and no morphological changes were observed in the crystals shape but the POM analysis confirmed the presence of a polycrystalline compound (figure 47b). The structural evolution associated to the thermal treatment was investigated by XRD that confirmed the evolution from one polymorph into the other (figure 47c). The same approach was also used for a NTA thin deposit which was heated to 200°C and then cooled down to room temperature. Upon this treatment, while the morphology and emission features of rhombohedral crystals remained apparently almost unaltered, the fiber-like crystals exhibited an irreversible change in PL, which switched irreversibly from yellow to green (figure 48a-b). Although a thin deposits with only one polymorph was not achieved, XRD were performed on NTA thin deposits at room temperature and after the thermal cycle rt→200°C→rt (figure 48e).

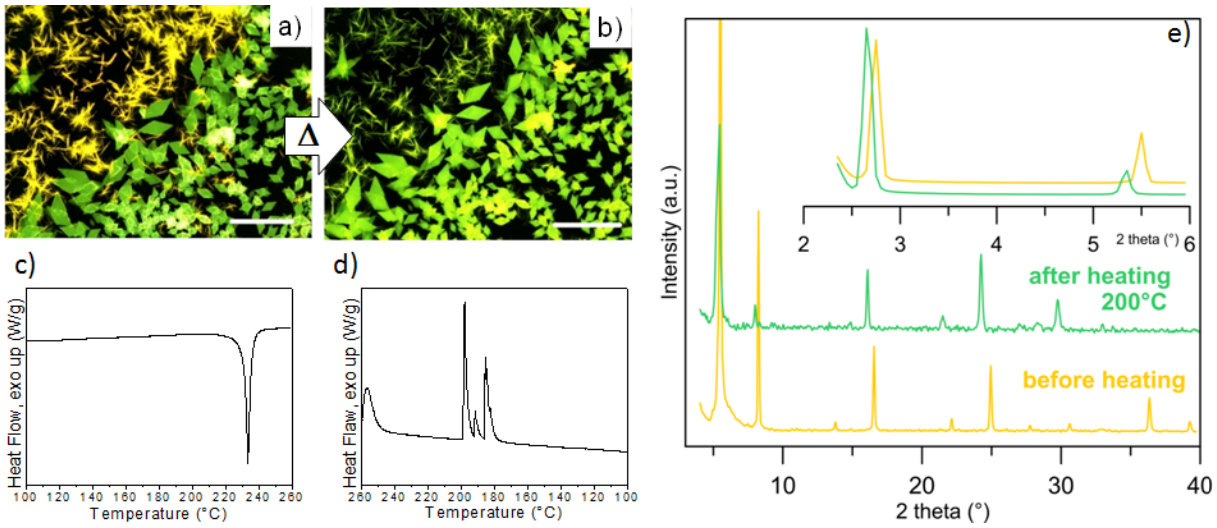

Figure 48. a) Fluorescence microscopy image of a drop cast thin deposit of NTA (toluene 1 mg/ml on Si/SiO_2 wafer; scale bar 100 µm). b) The same image after thermal treatment at 200°C for 30 s. c-d) Thermograms of c) heating and d) cooling, of NTA under nitrogen atmosphere (20°C/min). e) XRD patterns of NTA sample before and after the thermal cycle.

The XRD profiles show significant differences, and in particular the disappearing of some reflections after the thermal cycle, support the polymorphic conversion observed by optical microscopy.

Finally, azomethine NTI did not show detectable fluorescence differences upon thermal treatment before the melting point. However in POM, a solid state transition is observed for the rod-like crystals, which is consistent with the solid-solid transition at 170°C, observed in the DSC curve (figure 49).

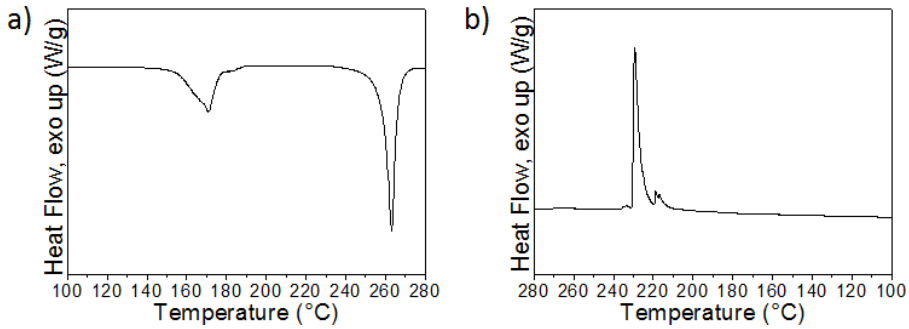

Figure 49. Thermograms of a) heating and b) cooling of NTI under nitrogen atmosphere (20°C/min).

The polymorphism of NTE was exploited for the fabrication of a TTI device (see 3.5.2 section), monitoring the evolution of temperature-dependent fluorescence properties. A commercial charge-coupled device (CCD, details not reported herein) recorded the fluorescence images during the thermal treatment. Figure 50 shows the number of counts (NCs) of the red, green and blue components recorded by the CCD as a function of the temperature at which the device was exposed for 30 s (details are not reported herein).

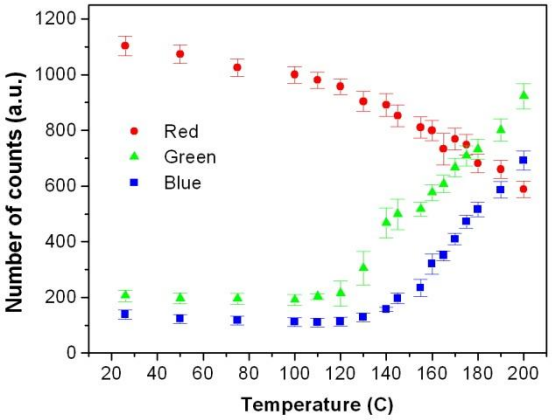

Figure 50. Quantitative analysis of the fluorescence images. A commercial CCD recorded fluorescence images. The colours of the graphs correspond to the colour components of the CCD (red, blue, green). The figure shows the number of counts versus temperature obtained using a filter Ex 420, DM 435, BA 475, which enables the transmission of all visible components except a slight portion of the blue.

The quantitative analysis of the CCD counts shows that for each temperature, the colour recorded is formed by a unique and defined combination of red, green and blue (RGB) components. Therefore, the temperature at which the device was exposed can be analytically derived from the colour composition of the PL image. It should be noted that for NTE in the range between rt and 120°C (i.e. below the transition temperature between the two polymorphs, therefore independent

from polymorphism), higher sensitivity is obtained from the red component with an accuracy of ±5°C. On the other hand, for temperatures higher than 120°C, i.e. above the transition temperature of the polymorphs, the best accuracy can be extracted from the blue component with an accuracy of <±2°C, i.e. two times better than the interval rt-120°C. This behaviour suggests that the sensitivity to temperature exposure in TTI devices based on this class of materials can be improved by polymorphic transition and therefore tailored by chemical design.

3.6 Synthetic issues

A direct arylation based protocol has been investigated as alternative approach to conventional Stille cross-coupling methodologies in the synthesis of functional molecular materials with complex structures. In particular, this alternative route has been focused on thiophene based systems with 2,3-thienoimide ends as well as anthracene or 3,4-thienoimide cores (figure 51).

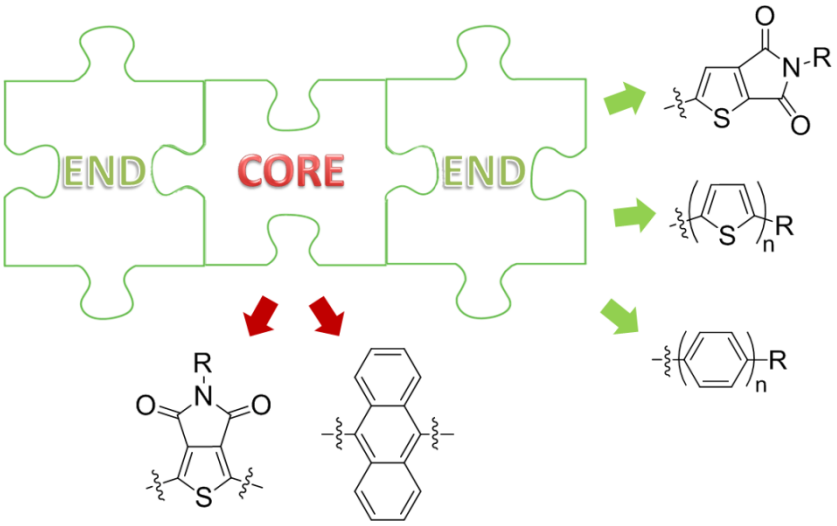

Figure 51. Schematic representation of the substrates used as building blocks of materials synthesized by direct arylation reactions.

3.6.1 Synthesis of thienoimide based materials by direct arylation reactions

The direct arylation route under Fagnou's conditions has been applied to synthesize materials NT3N and NT5N described in section 3.3, comparing this synthetic way to the conventional Stille cross-coupling based protocol (scheme 12).[19] An advantage of the direct arylation reaction (besides avoiding the use of the organometallic reagent and thus also its preparation), relies in the direct use of the 2,3-thienoimide moiety, thus avoiding its bromination to get compound **4** (scheme 12), which requires harsh conditions, long times and that generally results sensitive to the scale-up.

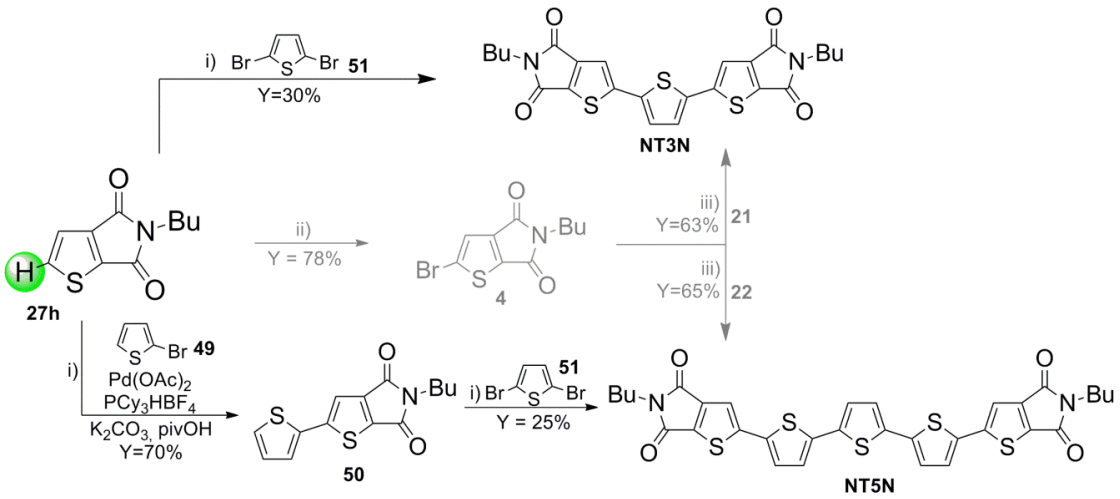

Scheme 12. Synthesis of materials NT3N and NT5N by direct arylation reaction (balck path) and comparison with Stille cross-coupling (grey path). i) toluene, reflux 24 h. ii) NBS, TFA, H_2SO_4, 48 h. iii) Refluxing toluene, in situ $Pd(AsPh_3)_4$, 24 h.

The direct approach for the synthesis of NT5N involves in a first step the coupling between 2,3-TI **27h** and commercial 2-bromothiophene **49** ($Pd(OAc)_2$, PCy_3HBF_4, K_2CO_3) in refluxing toluene and in the presence of 30% pivOH, obtaining the dimer **50** in satisfying yield (70%). However, just a moderate yield (25%) was achieved in the double coupling of **50** with 2,5-dibromothiophene **51** to get NT5N material. The reaction between 2,3-TI and **51** showed the same trend, achieving NT3N in 30% yield. The reason of the partial conversion is still not clear even if the poorer solubility of the brominated intermediate (deriving from a single coupling of the TI on the dibrominated species) could play a major role.

Different reactivity is shown instead by the regioisomer 3,4-thienoimide. In fact, as reported in Leclerc's work,[44] this molecule resulted highly reactive through the direct arylation. In scheme 13 the synthesis of three new derivatives (**52a-c**) is described.

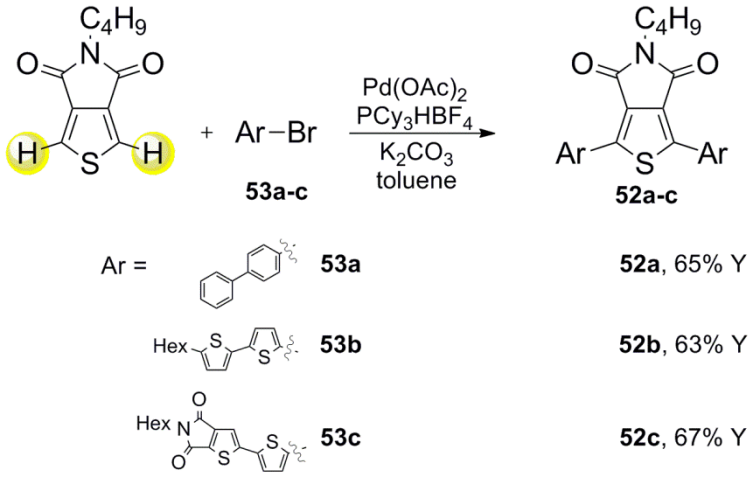

Scheme 13. Synthesis of materials **52a-c** by direct arylation reaction.

A direct arylation between 3,4-TI and the proper bromoinated derivative **53a-c** afforded the target materials **52a**-**c** with yields ranging from 63 and 67% after purification by flash chromatography and following crystallization. The reaction involved the use of a Pd(0) catalyst and K_2CO_3 as base, without using pivalic acid, since the oxygen atom of the imide moiety acts as orienting and activating group for the hydrogen atoms.[44] While 4-bromobiphenyl **53a** and 5-bromo-5'-hexyl-2,2'-bithiophene **53b** are commercial, compound **53c** was synthesized by a direct arylation between 2,3-TI **28c** and commercial 2-bromothiophene **49** followed by a conventional bromination reaction of the resulting dimer with NBS.

The different position of the carbonyl groups in 3,4-thienoimide moiety with respect the regioisomeric 2,3-TI, represent the reason of its enhanced reactivity towards direct arylation reactions. Indeed, since 2,3-thienoimide is a less reactive substrate, it needs the presence of a proton shuttle as pivalic acid promoting the cleavage of the C-H bond and the subsequent aryl-aryl coupling.

Deeper studies on the optimization of the direct arylation route with 2,3-TI based systems are currently on going, mainly investigating the influence of different solvents or bases and performing the reaction under MW assistance.

3.6.2 Synthesis of anthracene based materials by MW-assisted direct arylation

As already introduced the direct arylation approach has been applied also to the synthesis of anthracene based materials, for the development of new synthetic strategies involving the MW assistance as well as of new classes of functional materials.

In this line, a double direct arylation combined to MWs, was exploited to synthesize a family of 9,10-dithienylanthracene materials (**54a-f**), in overall yields higher than those achieved by Stille cross-couplings taken as reference conventional approach and very short times of reaction (5 minutes).[45] Scheme 14 (black path) shows the double direct arylation route adopted for the synthesis of the target materials. 9,10-dibromoanthracene **55** was used as starting materials together with unsubstituted thiophene **56** and bithiophene **59** or end-substituted analogues (**57**, **58** and **60**, **61**). The reaction follows Fagnou's conditions (with Kappe's modifications),[46] involving a sub-stoichiometric amount of pivOH and an excess of K_2CO_3, with stoichiometric thienyl derivatives. Only in the reactions with unsubstituted thiophene and bithiophene as

dibromoanthracene coupling partners (having two possible C-H active sites), a large excess of thiophene-based units (5 equiv) with respect to the anthracene counterpart was used in order to promote selective formation of the target systems.[47] By exploiting the approach depicted in scheme 14 (black path) the target anthracene based materials (DTA, H-DTA, F-DTA, DTTA, H-DTTA, F-DTTA) were isolated in yields ranging from 31% to 81%, in only 5 min of MW irradiation, after purification by flash chromatography and following crystallization from toluene.

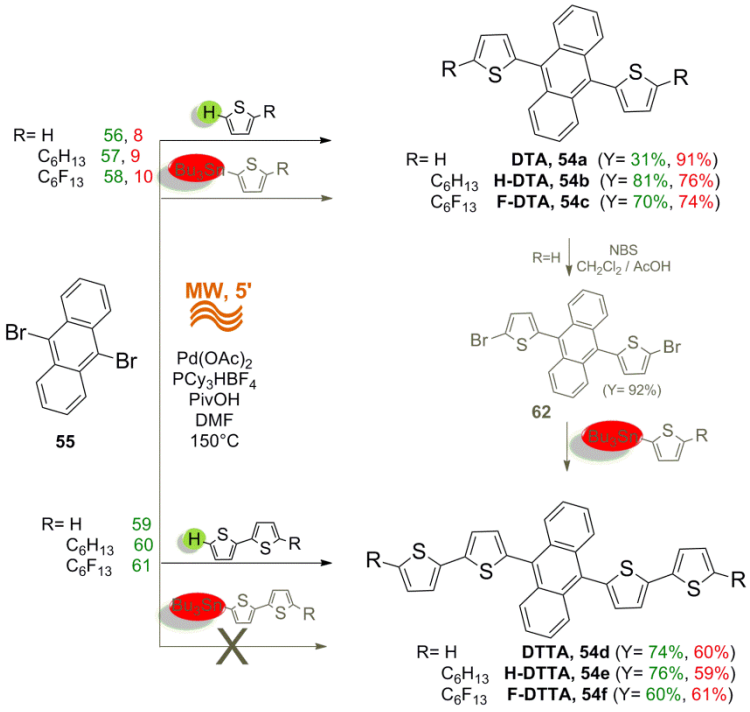

Scheme 14. Synthetic route to 9,10-diarylanthracene materials 56a-f by MW-assisted direct arylation (black path) and comparison with Stille cross-coupling based procedure (grey path).

For comparison, the same reactions were performed without the aid of MW. Interestingly, comparable yields were achieved only after 24 h at 110°C rather than 5 min. Moreover, in order to assess the convenience of the direct arylation reaction, the target compounds were also prepared by following an already reported Stille coupling based procedure (scheme 14 grey path).[48] All tributylstannyl precursors were synthesized according to conventional stannylation procedures. Then, they were coupled to compound **55** (toluene, reflux, 24 h) to give anthracene compounds DTA, H-DTA, and F-DTA in 91%, 76% and 74% yields, respectively. Remarkably, the equivalent one-step approach based on the coupling of compound **55** directly with stannylbithiophenes, led to DTTA, H-DTTA, and F-DTTA in unsatisfied yields. This low reactivity was ascribed to the side homocoupling reaction of the stannylbithiophene derivatives to give quaterthiophene by-products, difficult to remove from the target materials. Consequently, for the preparation of these

materials a multi-step synthesis was carried out. To this aim, DTA was first dibrominated with NBS (to give compound **62**, Y= 92%) and then reacted with tributylstannyl derivatives **8-10**, affording compounds DTTA, H-DTTA, and F-DTTA in 60, 59, and 61% yields, respectively (scheme 14 grey path). Collectively, beside the advantage of reduced reaction times, the Stille overall yields (50, 49, and 51% for DTTA, H-DTTA, and F-DTTA, respectively, three steps) compare unfavorably to the direct arylation ones, making the latter a convenient approach for anthracene 9,10-diarylation.

The synthesized materials have been fully characterized (details not reported herein)[45] and the effect of the different side-arms substitution has been investigated on i) self-assembly at surface, ii) fluorescence and ii) charge transport capability. For systems with better film-forming and self-assembling properties, i.e. shorter oligomers and bearing perfluorohexyl groups, higher hole mobilities have been estimated.

The described approach thus represents a convenient atom economically and fast alternative to cross-coupling reactions for the preparation of anthracene based materials, whose side arms tailoring is responsible of their functional properties tuning.

References

[1] A. Facchetti, M. H. Yoon, C. L. Stern, G. R. Hutchison, M. A. Ratner and T. J. Marks, *J. Am. Chem. Soc.* **2004**, *126*, 13480-13501.

[2] M. Melucci, L. Favaretto, M. Zambianchi, M. Durso, M. Gazzano, A. Zanelli, M. Monari, M. G. Lobello, F. De Angelis, V. Biondo, G. Generali, S. Troisi, W. Koopman, S. Toffanin, R. Capelli and M, Muccini, *Chem. Mater.* **2013**, *25*, 668-676.

[3] a) S. Trasatti, *Pure Appl. Chem.* **1986**, *58*, 955-966; b) G. Gratzner and J. Kuta, *Pure Appl. Chem.* **1984**, *56*, 461-466.

[4] a) G. Zotti, G. Schiavon, A. Berlin and G. Pagani, *Chem. Mater.* **1993**, *5*, 620-624.; b) G. Zotti, G. Schiavon, A. Berlin and G. Pagani, *Chem. Mater.* **1993**, *5*, 430-436; c) G. Zotti, G. Schiavon, A. Berlin and G. Pagani, *Synth. Met.* **1993**, *61*, 81-87.

[5] R. Capelli, S. Toffanin, G. Generali, H. Usta, A. Facchetti and M. Muccini, *Nat. Mater.* **2010**, *9*, 496-503.

[6] J. L. Bredas, J. P. Calbert, F. D.-S. Filho and J. Cornil, *J. Proc. Natl. Acad. Sci.* **2002**, *99*, 5804-5809.

[7] M. D. Curtis, J. Cao and J. W. Kampf, *J. Am. Chem. Soc.* **2004**, *126*, 4318-4328.

[8] J. Zaumseil, C. R. McNeill, M. Bird, D. L. Smith, P. P. Ruden, M. Roberts, M. J. McKiernan, R. H. Friend and H. Sirringhaus, *J. Appl. Phys.* **2008**, *103*, 064517.

[9] M. Durso, D. Gentili, C. Bettini, A. Zanelli, M. Cavallini, F. De Angelis, M. G. Lobello, V. Biondo, M. Muccini, R. Capelli and M. Melucci, *Chem. Commun.* **2013**, *49*, 4298-4300.

[10] S. Oku, K. Takamiya, D. Adachi, S. Ishikawa, S. Nagamatsu, W. Takashima, S. Hayase and K. Kaneto, *Chem. Lett.* **2010**, *39*, 1315-1316.

[11] W. Li,H. E. Katz, A. J. Lovinger and J.G. Laquindanum, *Chem. Mater.* **1999**, *11*, 458-465.

[12] J. Roncali, *Macromol. Rapid Commun.* **2007**, *28*, 1761-1775.

[13] A. D. Becke, *J. Chem. Phys.* **1993**, *98*, 5648-5652.

[14] C. Wang, H. Dong, W. Hu, Y. Liu and D. Zhu, *Chem. Rev.* **2012**, *112*, 2208-2267

[15] J. Heinze, B. A. Frontana-Uribe and S. Ludwigs, *Chem. Rev.* **2010**, *110*, 4724-4771.

[16] M. Cavallini, *J. Mater. Chem.* **2009**, *19*, 6085-6092. a) M. Cavallini, C. Albonetti and F. Biscarini, *Adv. Mater.* **2009**, *21*, 1043-1053; b) M. Cavallini, D. Gentili, P. Greco, F. Valle and F. Biscarini, *Nat. Protocols* **2012**, *7*, 1668-1676.

[17] a) M. Cavallini, C. Albonetti and F. Biscarini, *Adv. Mater.* **2009**, *21*, 1043-1053; b) M. Cavallini, D. Gentili, P. Greco, F. Valle and F. Biscarini, *Nat. Protocols* **2012**, *7*, 1668-1676.

[18] a) M.-H. Yoon, S. A. Di Benedetto, A. Facchetti and T. J. Marks, *J. Am. Chem. Soc.* **2005**, *127*, 1348-1349; c) J. A. Letizia, S. Cronin, R. P.Ortiz, A. Facchetti, M. A. Ratner and T. Marks, *Chem. Eur. J.* **2010**, *16*, 1911-1928; d) M.-H. Yoon, S. A. Di Benedetto, M. T. Russell, A. Facchetti and T. J. Marks, *Chem. Mater.* **2007**, *19*, 4864-4881.

[19] M. Durso,C. Bettini, A. Zanelli, M. Gazzano, M. G. Lobello, F. De Angelis, V. Biondo, D. Gentili, R. Capelli, M. Cavallini, S. Toffanin, M. Muccini and M., Melucci, *Org. Electron.* **2013**, *14*, 3089-3097.

[20] a) A. Yassar, C. Videlot and A. Jaafari, *Sol. Energy Mater. Sol. Cells* **2006**, *90*, 916-922; b) I. Viola, F. Della Sala, M. Piacenza, L. Favaretto, M. Gazzano, M. Anni, G. Barbarella, R. Cingolani and G. Gigli, *Adv. Mater.* **2007**, *19*, 1597-1602.

[21] a) M. Melucci, M. Gazzano, G. Barbarella, M. Cavallini, F. Biscarini, P. Maccagnani and P. Ostoja, *J. Am. Chem. Soc.* **2003**, *125*, 10266-10274; b) M. Melucci, L. Favaretto, C. Bettini, M. Gazzano, N. Camaioni, P. Maccagnani, P. Ostoja, M. Monari and G. Barbarella, *Chem. Eur. J.* **2007**, *13*, 10046-10054.

[22] K. Meerholz and J. Heinze, *Electrochim. Acta* **1996**, *41*, 1839-1854.

[23] D. Fichou (Ed.), *The Handbook of Oligo-and Polythiophenes*, Wiley-VCH Verlag GmbH, Weinheim, Germany, **1999**.
[24] S. Handa, E. Miyazaki, K. Takimiya and Y. Kunugi, *J. Am. Chem. Soc.* **2007**, *129*, 11684-11685.
[25] a) A. Facchetti, M. Mushrush, H.E. Katz and T.J. Marks, *Adv. Mater.* **2003**, *15*, 33-38 ; b) R.J. Chesterfield, C.R. Newman, T.M. Pappenfus, P.C. Ewbank, M.H. Haukaas, K.R. Mann, L.L. Miller and C.D. Frisbie, *Adv. Mater.* **2003**, *15*, 1278-1282.
[26] M. Melucci, M. Zambianchi, L. Favaretto, M. Gazzano, A. Zanelli, M. Monari, R. Capelli, S. Troisi, S. Toffanin and M. Muccini, *Chem. Commun.* **2011**, *47*, 11840-11842.
[27] M. Melucci, M. Durso, C. Bettini, M. Gazzano, L. Maini, S. Toffanin, S. Cavallini, M. Cavallini, D. Gentili, V. Biondo, G. Generali, F. Gallino, R. Capelli and M. Muccini, *J. Mater. Chem. C* **2014**, *2*, 3448-3456.
[28] M. A. Spackman and A. S. Mitchell, *Phys. Chem. Chem. Phys.* **2001**, *3*, 1518-1523.
[29] a) M. M. Labes and A. Weissberger, *Physics and Chemistry of the Organic Solid State*, ed. D. Fox, Interscience Publishers, London, **1965**; b) J. Bernstein, *Polymorphism in Molecular Crystals*, Clarendon Press, Oxford, **2002**; c) A. J. Cruz-Cabeza and J. Bernstein, *Chem. Rev.* **2014**, *114*, 2170-2191.
[30] a) W.-Y. Chou, M.-H. Chang, H.-L. Cheng, Y.-C. Lee, C.-C. Chang and H.-S. Sheu, *J. Phys. Chem. C* **2012**, *116*, 8619-8626; b) A. Moser, I. Salzmann, M. Oehzelt, A. Neuhold, H.-G. Flesch, J. Ivanco, S. Pop, T. Toader, D. R. T. Zahn, D.-M. Smilgies and R. Resel, *Chem. Phys. Lett.* **2013**, *574*, 51-55; c) T. Siegrist, C.Kloc, R. A. Laudise, H. E. Katz and R.C. Haddon, *Adv. Mater.* **1998**, *10*, 379-382; d) O. D. Jurchescu, A. Meetsma and T. T. M. Palstra, *Acta Crystallogr., Sect. B: Struct. Sci.* **2006**, *62*, 330-334.
[31] a) O. Jurchescu, D. Mourey, S. Subramanian, S. Parkin, B. Vogel, J. Anthony, T. Jackson and D. Gundlach, *Phys. Rev. B* **2009**, *80*, 085201; b) S. T. Salammal, J.-Y. Balandier, J.-B. Arlin, Y. Olivier, V. Lemaur, L. Wang, D. Beljonne, J. Cornil, A. R. Kennedy, Y. H. Geerts and B. Chattopadhyay, *J. Phys. Chem. C* **2014**, *118*, 657-669; c) K. Wang, H. Zhang, S. Chen, G. Yang, J. Zhang, W. Tian, Z. Su and Y. Wang, *Adv. Mater.* **2014**, *26*, 6168-6173; d) H. B. Akkerman, S. C. B. Mannsfeld, A. P. Kaushik, E. Verploegen, L. Burnier, A. P. Zoombelt, J. D. Saathoff, S. Hong, S. Atahan-Evrenk, X. Liu, A. Aspuru-Guzik, M. F. Toney, P. Clancy and Z. Bao, *J. Am. Chem. Soc.* **2013**, *135*, 11006-11014.
[32] L. Maini, F. Gallino, M. Zambianchi, M. Durso, M. Gazzano, K. Rubini, D. Gentili, I. Manet, M. Muccini, S. Toffanin, M. Cavallini and M. Melucci, *Chem. Commun.* **2015**, *51*, 2033-2035.
[33] R. D. Deegan, O. Bakajin, T. F. Dupont, G. Huber, S. R. Nagel and T. A. Witten, *Nature* **1997**, *389*, 827-829.
[34] D. Gentili, M. Durso, C. Bettini, I. Manet, M. Gazzano, R. Capelli, M. Muccini, M. Melucci and M. Cavallini, *Sci. Rep.* **2013**, *3* : 2581.
[35] a) W. J. Manske, *Selected time interval indicating device*. US Patents **1976**, 3, 954, 011; b) P. S. Taoukis and T. P. Labuza, *J. Food Sci.* **1989**, *54*, 783-788; c) M. Cavallini, A. Calò, P. Stoliar, J. C. Kengne, S. Martins, F. C. Matacotta, F. Quist, G. Gbabode, N. Dumont, Y. H. Geerts and F. Biscarini, *Adv. Mater.* **2009**, *21*, 4688-4691; d) A. Calò, P. Stoliar, F. C. Matacotta, M. Cavallini and F. Biscarini, *Langmuir* **2010**, *26*, 5312-5315.
[36] M. Zambianchi, L. Favaretto, M. Durso, C. Bettini, A. Zanelli, I. Manet, M. Gazzano, L. Maini, D. Gentili, S. Toffanin, F. Gallino, M. Muccini, M. Cavallini and M. Melucci, *J. Mater. Chem. C* **2015**, *3*, 121-131.
[37] a) P. Frère, J.-M. Raimundo, P. Blanchard, J. Delaunay, P. Richomme, J.-L. Sauvajol, J. Orduna, J. Garin and J. Roncali, *J. Org. Chem.* **2003**, *68*, 7254-7265; b) G. Neculqueo, V. Rojas Fuentes, A. Lopez, R. Matute, S. O. Vasquez and F. Martinez, *Struct. Chem.* **2012**, *23*, 1751-1760.

[38] a) S. Dufresne, M. Bourgeaux and W. G. Skene, *J. Mater. Chem.* **2007**, *17*, 1166-1177; b) N. Kiriy, V. Bocharova, A. Kiriy, M. Stamm, F. C. Krebs and H.-J. Adler, *Chem. Mater.* **2004**, *16*, 4765-4771; c) Y. Dong, D. Navarathne, A. Bolduc, N. McGregor and W. G. Skene, *J. Org. Chem.* **2012**, *77*, 5429-5433.

[39] M. Melucci, G. Barbarella, M. Zambianchi, P. Di Pietro and A. Bongini, *J. Org. Chem.* **2004**, *69*, 4821-4828.

[40] K. Starcevic, D. W. Boykin and G. Karminski-Zamola, *Heteroat. Chem.* **2003**, *14*, 218-222.

[41] E.T.C. S.r.l., M. Melucci; L. Favaretto, M. Zambianchi, R. Capelli, M. Muccini, Patent: WO2014076650 A1, pg. 31.

[42] M. J. Mio, L. C. Kopel, J. B. Braun, T. L. Gadzikwa, K. L. Hull, R. G. Brisbois, C. J. Markworth and P. A. Grieco, *Org. Lett.* **2002**, *4*, 3199-3203.

[43] E.T.C. S.r.l., M. Melucci; L. Favaretto, M. Zambianchi, R. Capelli, M. Muccini, Patent: WO2014076662 A1, pg. 24.

[44] P. Berrouard, A. Najari, A. Pron, D. Gendron, P.-O. Morin, J.-R. Pouliot, J. Veilleux and M. Leclerc, *Angew. Chem. Int. Ed.* **2012**, *51*, 2078-2071.

[45] M. Durso, M. Zambianchi, A. Zanelli, M. G. LoBello, F. De Angelis, S. Toffanin, S. Cavallini, D. Gentili, F. Tinti, M. Cavallini, N. Camaioni and M. Melucci, *Tetrahedron* **2014**, *70*, 6222-6228.

[46] M. Baghbanzadeh, C. Pilger and C. O. Kappe, *J. Org. Chem.* **2011**, *76*, 8138-8142.

[47] D. J. Schipper and K. Fagnou, *Chem. Mater.* **2011**, *23*, 1594-1600.

[48] a) J. H. Choi, D. W. Cho, S. H. Jin and U. C. Yoon, *Bull. Korean Chem. Soc.* **2007**, *28*, 1175-1182; b) J. H. Choi, D. W. Cho, N. K. Sung, S. H. Jin and U. C. Yoon, *Bull. Korean Chem. Soc.* **2007**, *28*, 1931-1938;c) S. Kotha, A. K. Ghosh and K. D. Deodhar, *Synthesis* **2004**, *4*, 549-557.

Chapter 4

Conclusions

In this thesis work, the molecular structure of NT4N was finely tailored by following precise **design strategies**, with the aim of tuning and enhancing its charge transport and electroluminescence properties. Moreover, structure-properties relationships investigations were performed on the newly developed materials.

In particular, the effect of different π-conjugated cores (heterocycles, length) and alkyl end chain (shape, length) changes have been deeply studied.

The conclusions are summarized in the following points, schematized in figure 52.

a) Desymmetrization of NT4N (i.e. by introducing one TI end in oligothiophene based semiconductors) revealed that, while the symmetric system shows a π-stacking packing, contrarily non-symmetric derivatives display a herringbone like packing. Despite this, comparable electroluminescence and ambipolarity were found for both symmetric NT4N and non-symmetric HT4N and FT4N, while no electroluminescence and unipolar charge transport were found for conventional T4 based materials. Moreover, non-symmetric systems bearing EWG alkyl ends opposite to the TI unit display major n-type contribute. Conversely, systems with EDG groups show major p-type contribute, highlighting this strategy as a tool to tune the ambipolarity by molecular design.

b) Replacing the bithiophene unit of NT4N with more e^- deficient cores, electron charge mobilities up to 0.3 $cm^2/V \cdot s$ have been reached (in not optimized devices), while by changing the thiopene-based core length enhanced electron mobility with unaltered hole mobility has been achieved.

c) The study of Cx-NT4N with x = C1–C8 allowed us to assert that, contrarily to what generally observed for oligothiophenes, different alkyl end chains didn't affect significantly the electrical properties in TBI based materials but they selectively tuned the electroluminescence, which increases together with the chain length.

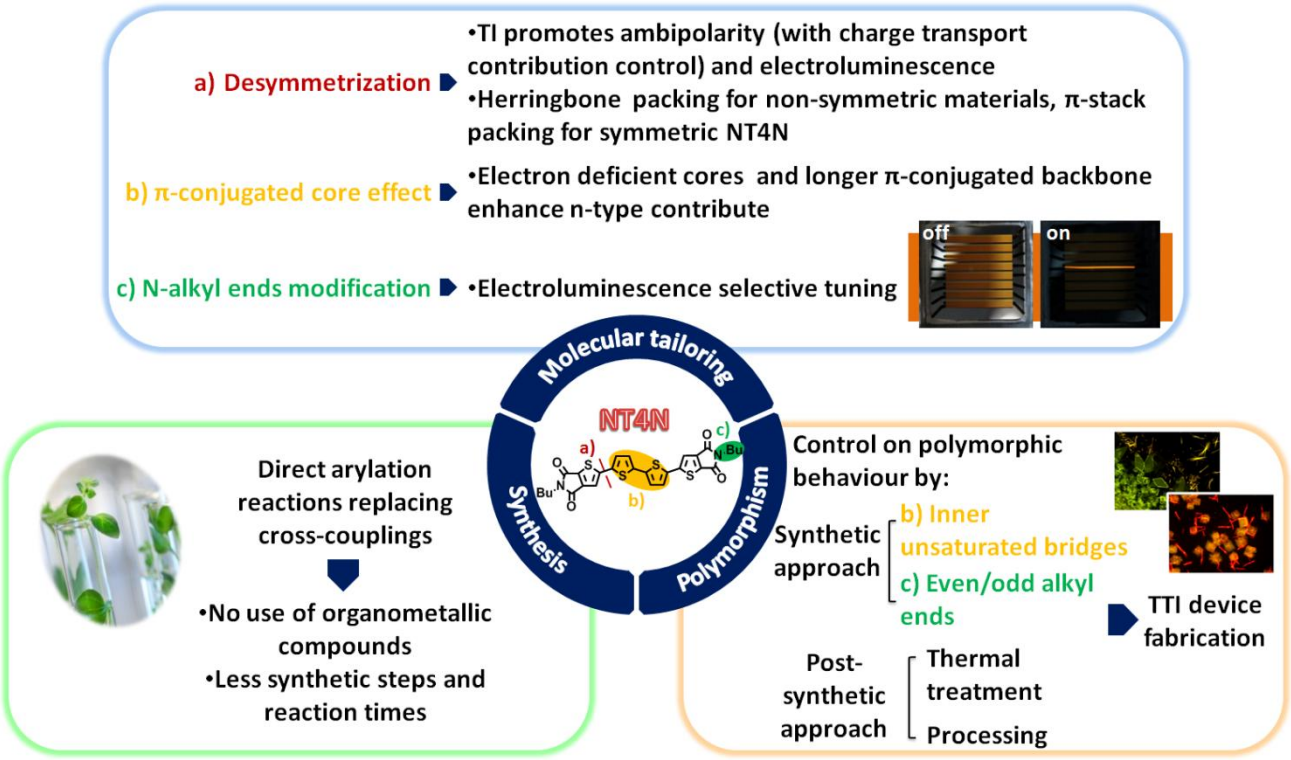

Figure 52. Schematic summary of the work described in the thesis.

The unprecedented properties featuring such molecular materials allowed to realize devices with simpler architectures based on a single organic multifunctional material (ambipolar and electroluminescent, with EQE up to 0.2% and EP up to 180 nW) rather than different monofunctional materials. Further molecular tailoring approaches are currently under investigation in order to improve the mobility values, balance p and n transport capabilities and enhance the electroluminescence at the solid state.

Interestingly, NT4N as well as other TBI derivatives showed **polymorphic behaviour**. Starting from C4 alkyl ended NT4N and tuning the alkyl end chain, we found that the odd/even symmetry of the N-alkyl chains and the insertion of different inner unsaturated bridges revealed good

strategies to define the packing mode and the geometry of TBI compounds, becoming interesting tools to control the conformational polymorphism of these materials.

The polymorphic temperature dependant nature characterizing some TBI materials, usually detrimental for electronic applications, has been exploited to build a different kind of organic device, called time temperature integrator. Based on a change in fluorescence colour detectable by optical microscopy after a thermal treatment, it can be used to monitor the temperature exposure of products like perishable goods and drugs.

Being the control of the polymorphism an 'atom economically' way to tuning the morphological and optical properties of TBI based materials, further investigations are carried out in our laboratory with the aim of controlling the electrical behaviour in charge transport based devices as well as to enable new applications.

Finally, with the aim of obtaining a high purity level in the synthesized materials, new synthetic procedures have been investigated in order to simplify the purification steps and avoid organometallic residues, harmful for the correct performance of the electronic device. Indeed, a **direct arylation** approach has been introduced in order to replace the conventional cross-coupling reactions (i.e. Stille and Suzuki couplings among the others), thus avoiding the stoichiometric use of organometallic reagents. The method was successfully applied to different classes of molecules, bearing thienoimidic core or ends, as well as thiophene and anthracene derivatives, achieving good yields and exploiting also MW assistance. The procedure thus represents a valid clean alternative for the synthesis of several molecular materials. The optimization of the synthesis of TBI materials by direct arylation is currently on going in the laboratory.

In conclusion, the results here described contribute to the development of novel multifunctional molecular materials enabling the fabrication of simple-architecture low-cost single layer OFET/OLET as well as TTI devices. Moreover, the combination of experimental data and theoretical calculations allowed a wide investigation on the structure-properties relationships in the synthesized 2,3-thienoimide based materials that can be useful to develop new property-specific materials.

Chapter 5

Experimental section

5.1 General methods

All commercial reagents were purchased as reagent grade from Sigma-Aldrich, Alfa Aesar, Acros Organics, and used as received. MW-assisted reactions were carried out in a CEM DISCOVER SP reactor in a closed vessels (200W, fixed temperature at 150°C, maximum pressure reached 15-20 psi, air, medium stirring rate). Thin layer chromatography (TLC) was carried out on Merk silica gel 60 F254 plates. Flash chromatography was performed by using glass columns packed with Merk silica gel 60 (230-400 mesh), or by using a CombiFlash® Rf 200 system (Teledyne-Isco, Lincoln, NE, USA) using RediSep Rf normal-phase silica columns. All NMR spectra were recorded at room temperature using a Varian Mercury 400 spectrometer (^{1}H: 400 MHz; ^{13}C: 100 MHz; ^{19}F: 376 MHz). Chemical shifts were calibrated with the internal $CDCl_3$ resonance, referenced to TMS. For ^{19}F-NMR spectra, 0.2% of fluorobenzene (referenced to $CFCl_3$) was added as internal standard. Mass spectra were obtained with a Trace 1300 GC coupled to an ISQ mass spectrometer (Thermo Scientific) controlled by a computer running XCalibur software. According to the mass to be detected two different analytical approaches were employed, gas chromatography mass spectrometry (GC-MS) or direct exposure electron ionization mass spectrometry (DE-MS). Melting points were determined on a 'hot-stage' apparatus where the melting process was observed with the aid of a microscope. Differential scanning calorimetry (DSC) analysis was performed by using a Thass DSC-XP-10 instrument under atmospheric conditions or nitrogen atmosphere if specified.

UV-Vis spectra were recorded using a Perkin Elmer Lambda 20 spectrometer. Photoluminescence spectra were obtained with a Perkin Elmer LS50B spectrofluorometer by using an excitation wavelength corresponding to the maximum absorption lambda.

5.2 Synthesis and characterization

Compounds **9**, **10**, **14**, **22**, were prepared according to already reported procedures. [1]

5.2.1 Synthesis of compounds 1-7

General Stille cross-coupling reaction for the synthesis of compounds 1-3, 6

To a refluxing toluene solution (0.05 M) of the brominated derivative **7** (or **4**, 1 mmol) and in situ-prepared $Pd(AsPh_3)_4$ [8 mol%, Pd_2dba_3 (0.04 mmol), $AsPh_3$ (0.32 mmol)] under N_2 atmosphere, the proper stannylated derivative **8**-**10** (or **5**, 1.05 mmol) in dry toluene (0.1 M), was added dropwise. The solution was refluxed for 8 h then the solvent was removed under vacuum and the crude product purified by flash chromatography on silica gel. A following crystallization from hot toluene provided the target compound as a powder.

2-(2,2':5',2"-Terthiophene-5-yl)-5-butyl-5H-thieno[3,2-c]pyrrole-4,6-dione, **T4N**, **1**.

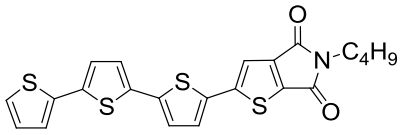

Orange powder (55% yield). M.p. 203° (K → LC), 226 °C. MS (70 eV, EI): m/z 455 ($M^{\cdot+}$). ^{1}H-NMR (CD_2Cl_2, TMS/ppm): δ 7.34 (s, 1H), 7.30 (m, 2H), 7.25 (dd, *J* = 3.6, 1.2 Hz, 1H), 7.19 (d, *J* = 3.6 Hz, 1H), 7.18 (d, *J* = 4.0 Hz, 1H), 7.15 (d, *J* = 4.0 Hz, 1H), 7.07 (dd, *J* = 3.2 Hz, 1.6 1H), 3.60 (t, 2H), 1.63 (m, 2H), 1.36 (m, 2H), 0.96 (t, 3H). ^{13}C-NMR ($CDCl_3$, TMS/ppm): δ 163.9, 162.8, 149.8, 145.3, 139.0, 137.5, 137.1, 136.7, 134.7, 133.6, 128.0, 126.8, 125.3, 125.0, 124.5, 124.4, 124.1, 116.3, 38.3, 30.8, 20.0, 13.6. λ_{max} (CH_2Cl_2), 441 nm. λ_{em} (CH_2Cl_2), 606 nm.

2-(5"-Hexyl-2,2':5',2"-terthiophene-5-yl)-5-butyl-5H-thieno[3,2-c]pyrrole-4,6-dione, **HT4N**, **2**.

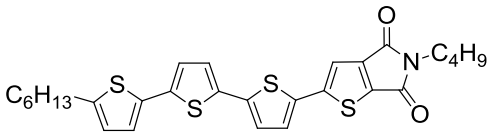

Orange powder (68% yield). M.p. 178° (K → LC), 260 °C. MS (70 eV, EI): m/z 539 ($M^{\cdot+}$). ^{1}H-NMR ($CDCl_3$, TMS/ppm): δ 7.28 (s, 1H), 7.22 (d, *J* = 3.6 Hz, 1H), 7.10 (d, *J* = 3.6 Hz, 1H), 7.09 (d, *J* = 4.0 Hz, 1H), 7.01 (d, *J* = 4.0 Hz, 1H), 7.00 (d, *J* = 3.6 Hz, 1H), 7.69 (d, *J* = 3.6 Hz, 1H), 3.60 (t, 2H), 2.80 (t, 2H), 1.66 (m, 4H), 1.35 (m, 8H), 0.92 (m, 6H). ^{13}C-NMR (CDCl3, TMS/ppm): δ 163.9, 162.8, 149.9, 146.2, 145.3, 139.2, 138.2, 137.0, 134.0, 133.3, 126.7, 125.2, 124.9, 124.2, 123.8, 123.7,116.2, 38.3, 31.5, 30.9, 30.2, 28.7, 22.6, 20.0, 14.1, 13.6. λ_{max} (CH_2Cl_2), 447 nm. λ_{em} (CH_2Cl_2), 631 nm.

2-(5”-(Perfluorohexyl)-2,2’:5’,2”-terthiophene-5-yl)-5-butyl-5Hthieno[3,2-c]pyrrole-4,6-dione, **FT4N**, **3**.

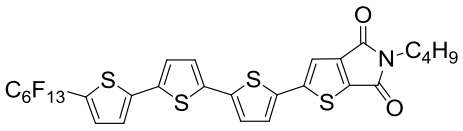

Orange powder (74% yield). M.p. 182° (K → LC), 320 °C. MS (70 eV, EI): m/z 773 ($M^{\cdot+}$). ^{1}H-NMR ($CDCl_3$, TMS/ppm): δ 7.36 (d, *J* = 3.6 Hz 1 H), 7.31 (s, 1H), 7.25 (d, *J* = 4.4 Hz, 1H), 7.17 (m, 4H), 3.61 (t, 2H), 1.63 (m, 2H), 1.36 (m, 2H), 0.95 (t, 3H). ^{13}C-NMR (CDCl3, TMS/ppm): δ 163.9, 162.7, 149.5, 145.3, 141.8, 138.3, 137.5, 136.7, 135.1, 134.3, 131.1, 126.8, 126.1, 125.4, 125.0, 123.7, 116.5, 38.4, 30.8, 20.0, 13.6. ^{19}F-NMR ($CDCl_3$, C_6H_5F/ppm): δ −80.2 (t, 3F), −100.8 (m, 2F), −121.0 (m, 4F), −122.3 (broad singlet, 2F), −125.6 (m, 2F). λ_{max} (CH_2Cl_2), 433 nm. λ_{em} (CH_2Cl_2), 580 nm.

2-([2,2’-Bithiophen]-5-yl)-5-butyl-4H-thieno[2,3-c]pyrrole-4,6(5H)-dione, **6**.

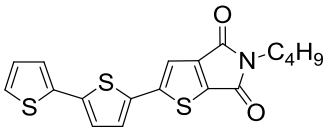

Orange powder (80% yield). MS (70 eV, EI): m/z 373 ($M^{\cdot+}$). ^{1}H-NMR ($CDCl_3$, TMS/ppm): δ 7.29 (s, 1H), 7.28 (dd, *J* = 5.2, 1.2, 1H), 7.23 (m, 2H), 7.12 (d, *J* = 3,6 Hz 1H), 7.05 (dd, *J* = 5.2, 4.8, 1H), 3.60 (t, 2H), 1.63 (m, 2H), 1.36 (m, 2H), 0.95 (t, 3H). ^{13}C-NMR ($CDCl_3$, TMS/ppm): δ 163.9, 162.8, 149.9, 145.2, 139.3, 137.1, 136.1, 133.6, 128.1, 126.7,125.5, 124.7,124.5, 116.3, 38.3, 30.8, 20.0, 13.6.

Bromination reaction under mild conditions

2-(5’-Bromo-[2,2’-bithiophen]-5-yl)-5-butyl-4H-thieno[2,3-c]-pyrrole-4,6(5H)-dione, **7**.

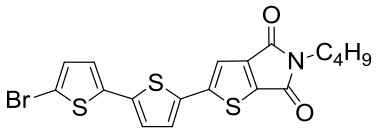

The starting material (SM) **6** (1 mmol) was dissolved in a 1:1 mixture of CH_2Cl_2 and AcOH solution (0.03 M). NBS (1.15 mmol) was added at 0 °C, and the reaction mixture was stirred at rt overnight in darkness. The solution was diluted with water, extracted with CH_2Cl_2, washed with 10% $NaHCO_3$ and then water. The organic phase was dried over anhydrous Na_2SO_4, filtered, evaporated under vacuum and the crude product purified by flash chromatography on silica gel. The so obtained brominated target material (TM) was isolated as an orange powder (97% yield). M.p. 153 °C. MS (70 eV, EI): m/z 451-453 ($M^{\cdot+}$). ^{1}H-NMR ($CDCl_3$, TMS/ppm): δ 7.29 (s, 1H), 7.21 (d, *J* = 4.0 Hz, 1H), 7.05 (d, *J* = 3.6 Hz, 1H), 7.00 (d, *J* = 4.0 Hz, 1H), 6.96 (d, *J* = 4.0 Hz, 1H), 3.60 (t, 2H), 1.62 (m, 2H), 1.36 (m, 2H), 0.95 (t, 3H). ^{13}C-NMR ($CDCl_3$, TMS/ppm): δ 163.9, 162.7, 149.5, 145.2, 138.1, 137.6, 137.4, 134.0, 130.9, 126.7, 124.8, 124.7, 116.5, 112.3, 38.3, 30.8, 20.0, 13.6.

5.2.2 Synthesis of compounds 11-16

General Stille cross-coupling reaction for the synthesis of compounds 11-13

To a refluxing toluene solution (0.03 M) of the brominated thienoimide **4** (1 mmol) and in situ-prepared $Pd(AsPh_3)_4$ [8 mol%, Pd_2dba_3 (0.04 mmol), $AsPh_3$ (0.32 mmol)] under N_2 atmosphere, the proper stannylated derivative **14**-**16** (0.55 mmol) in dry toluene (0.1 M), was added dropwise. The solution was refluxed for 8 h then the solvent was removed under vacuum and the crude product purified by flash chromatography on silica gel. A following crystallization from hot toluene provided the target compound as a powder.

2,2'-([2,2'-bithiazole]-5,5'-diyl)bis(5-butyl-4H-thieno[2,3-c]pyrrole-4,6(5H)-dione), **NTzN**, **11**.

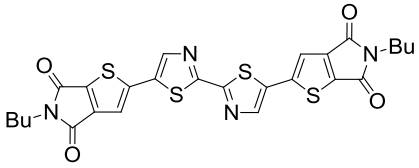

Orange powder (44% yield). M.p. >375 °C. MS (70 eV, EI): m/z 582 ($M^{\cdot+}$). ^{1}H-NMR ($CDCl_3$, TMS/ppm): δ 8.08 (s, 2 H), 7.44 (s, 2 H), 3.63 (t, 4H), 1.64 (m, 4H), 1.36 (m, 4H), 0.95 (t, 6H). ^{13}C-NMR ($CDCl_3$, TMS/ppm): δ 163.5, 162.3, 160.8, 145.2, 144.7, 141.7, 139.6, 133.2, 119.2, 38.5, 30.8, 20.0, 13.6. λ_{max} (CH_2Cl_2), 427nm. λ_{em} (CH_2Cl_2), 514nm, 488 nm.

2,2'-(thieno[3,2-b]thiophene-2,5-diyl)bis(5-butyl-4H-thieno[2,3-c]pyrrole-4,6(5H)-dione), **NThTN**, **12**.

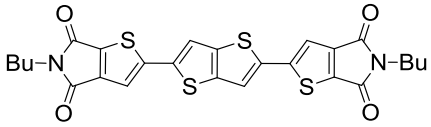

Orange powder (54% yield). M.p. >365 °C. MS (70 eV, EI): m/z 554 ($M^{\cdot+}$). ^{1}H-NMR ($CDCl_3$, TMS/ppm): δ 7.49 (s, 2 H), 7.38 (s, 2 H), 3.62 (t, 4H), 1.64 (m, 4H), 1.37 (m, 4H), 0.95 (t, 6H). λ_{max} (CH_2Cl_2), 441 nm. λ_{em} (CH_2Cl_2), 545 nm.

2,2'-(4,4'-dimethyl-[2,2'-bithiophene]-5,5'-diyl)bis(5-butyl-4H-thieno[2,3-c]pyrrole-4,6(5H)-dione), **NTMeN**, **13**.

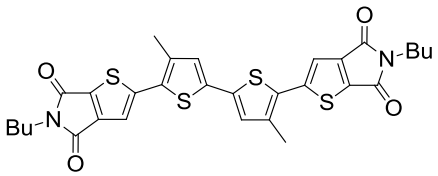

Red powder (64% yield). M.p. 248 °C. MS (70 eV, EI): m/z 608 ($M^{\cdot+}$). ^{1}H-NMR ($CDCl_3$, TMS/ppm): δ 7.30 (s, 2 H), 7.04 (s, 2 H), 3.62 (t, 4H), 2.43 (s, 6H), 1.64 (m, 4H), 1.36 (m, 4H), 0.95 (t, 6H). ^{13}C-NMR ($CDCl_3$, TMS/ppm): δ 164.1, 162.8, 148.9, 144.9 138.1, 137.6, 135.9, 128.9, 118.2, 38.3, 30.9, 20.0, 15.9, 13.6. λ_{max} (CH_2Cl_2), 449 nm. λ_{em} (CH_2Cl_2), 580 nm.

Stannylation reaction

(3,3'-dimethyl-[2,2'-bithiophene]-5,5'-diyl)bis(tributylstannane), **16**.

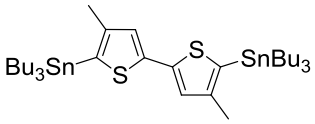

To an anhydrous solution of the brominated SM **17** (1 mmol) in Et_2O (0.1 M) under N_2 atmosphere, *n*-BuLi (2.5 M in hexane) was added dropwise (1.1 mmol) at -50° and the solution stirred for 2 h. Then Bu_3SnCl (0.9 mmol) was added dropwise and the solution stirred overnight. The reaction was quenched by adding water. The aqueous layer was extracted with Et_2O and the collected organic layers dried over Na_2SO_4. The solvent was removed under vacuum to give the TM **16** as a brown oil (96% yield). MS (70 eV, EI): m/z 770 ($M^{\cdot+}$). ^{1}H-NMR ($CDCl_3$, TMS/ppm): δ 7.08 (s, 2 H), 2.26 (s, 6H), 1.56 (m, 12H), 1.34 (m, 12H), 1.13 (t, 12H), 0.92 (t, 18H). ^{13}C-NMR ($CDCl_3$, TMS/ppm): δ 145.6, 142.7, 130.8, 127.1, 29.0, 27.3, 17.9, 13.6, 10.8.

5.2.3 Synthesis of compounds 19-20

Stille cross-coupling reaction for the synthesis of compounds 19-20

To a refluxing toluene solution (0.03 M) of the brominated thienoimide **4** (1 mmol) and in situ-prepared $Pd(AsPh_3)_4$ [10 mol%, Pd_2dba_3 (0.05 mmol), $AsPh_3$ (0.4 mmol)] under N_2 atmosphere, the proper stannylated derivative **21**-**22** (0.45 mmol) in dry toluene (0.2 M), was added dropwise. The solution was refluxed for 24 h then the solvent was removed under vacuum and the crude product purified by flash chromatography on silica gel. A following crystallization from hot toluene provided the target compound as a powder.

2,2'-(thiophene-2,5-diyl)bis(5-butyl-5Hthieno(3,2-c)pyrrole-4,6-dione), **NT3N**, **19**.

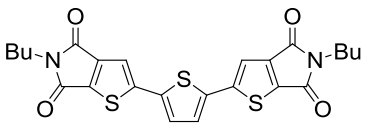

Orange powder (conventional Stille coupling: 65% yield; direct arylation: 30% yield). M.p. 210 °C. MS (70 eV, EI): m/z 498 ($M^{\cdot+}$). ^{1}H-NMR ($CDCl_3$, TMS/ppm): δ 7.36 (s, 2H), 7.29 (s, 2H), 3.62 (t, 4H), 1.63 (m, 4H), 1.37 (m, 4H), 0.95 (t, 6H); ^{13}C-NMR ($CDCl_3$, TMS/ppm): δ 163.7, 162.6, 148.5, 145.2, 138.3, 136.5, 126.9, 117.3, 38.4, 30.8, 20.0, 13.6. λ_{max} (CH_2Cl_2), 428 nm. λ_{em} (CH_2Cl_2), 526 nm.

2,2'-((2,2':5',2''-terthiophene)-5,5''-diyl)bis(5-butyl-4H-thieno(2,3-c)pyrrole-4,6(5H)-dione), **NT5N**, **20**.

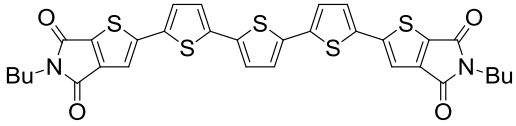

Dark red powder (conventional Stille coupling: 63% yield; direct arylation: 25% yield). M.p. 300 °C. MS (70 eV, EI): m/z 662 ($M^{\cdot+}$). ^{1}H-NMR ($CDCl_3$, TMS/ppm): δ 7.32 (s, 2H), 7.25 (d, *J* = 4.0 Hz, 2H), 7.17 (s, 2H), 7.15 (d, *J* = 4.0 Hz, 2H), 3.62 (t, 4H), 1.63 (m, 4H), 1.38 (m, 4H),0.97 (t, 6H). λ_{max} (CH_2Cl_2), 465 nm. λ_{em} (CH_2Cl_2), 599 nm.

5.2.4 Synthesis of compounds 24-28

Stille cross-coupling reaction for the synthesis of compounds 24a-g

To a refluxing toluene solution (0.05 M) of the brominated thienoimide **28a**-**f** (1 mmol) and in situ-prepared $Pd(AsPh_3)_4$ [6 mol%, Pd_2dba_3 (0.03 mmol), $AsPh_3$ (0.24 mmol)] under N_2 atmosphere, 5,5'-bis(tributylstannyl)-2,2'-bithiophene **29** (0.5 mmol) in dry toluene (0.1 M), was added dropwise. The solution was refluxed for 48 h, then *n*-pentane was added at rt and the precipitated solid was purified by flash chromatography on silica gel. A following crystallization from hot toluene provided the target compound as a powder.

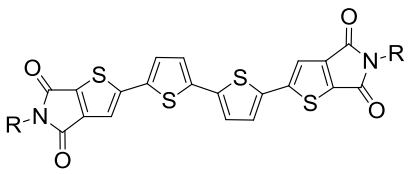

2,2'-(2,2'-Bithiophene-5,5'-diyl)bis(5-methyl-5H-thieno[3,2-c]-pyrrole-4,6-dione), **C1-NT4N**, **24a**.
Dark red powder (47% yield). M.p. >350 °C. MS (70 eV, EI): m/z 496 ($M^{\cdot+}$). ^{1}H-NMR (CD_2Cl_2, TMS/ppm): δ 7.37 (s, 2H), 7.33 (d, *J* = 3.6 Hz, 2H), 7.25 (d, *J* = 3.6 Hz, 2H), 3.10 (s, 6H). λ_{max} (CH_2Cl_2), 451 nm. λ_{em} (CH_2Cl_2), 572 nm.

2,2'-(2,2'-Bithiophene-5,5'-diyl)bis(5-propyl-5H-thieno[3,2-c]- pyrrole-4,6-dione), **C3-NT4N**, **24b**.
Red-orange powder (80% yield). M.p. 284 °C. MS (70 eV, EI): m/z 552 ($M^{\cdot+}$). ^{1}H-NMR ($CDCl_3$, TMS/ppm): δ 7.33 (s, 2H), 7.26 (d, *J* = 3.6 Hz, 2H), 7.18 (d, *J* = 4.0 Hz, 2H), 3.60 (t, 4H), 1.68 (m, 4H), 0.95 (t, 6H). ^{13}C-NMR ($CDCl_3$, TMS/ppm): δ 163.9, 162.7, 149.3, 145.2, 137.8, 137.6, 134.7, 126.8, 125.4, 116.7, 40.2, 22.1, 11.3. λ_{max} (CH_2Cl_2), 451 nm. λ_{em} (CH_2Cl_2), 572 nm.

2,2'-(2,2'-Bithiophene-5,5'-diyl)bis(5-hexyl-5H-thieno[3,2-c]-pyrrole-4,6-dione), **C6-NT4N**, **24c**.
Orange powder (78% yield). M.p. 283 °C. MS (70 eV, EI): m/z 636 ($M^{\cdot+}$). ^{1}H-NMR ($CDCl_3$, TMS/ppm): δ 7.32 (s, 2H), 7.26 (d, *J* = 3.6 Hz, 2H), 7.18 (d, *J* = 4.0 Hz), 3.60 (t, 4H), 1.64 (m, 4H),

1.31 (m, 12H), 0.95 (t, 6H). ^{13}C-NMR ($CDCl_3$, TMS/ppm): δ 163.8, 162.7, 149.3, 145.2, 137.8, 137.6, 134.7, 126.8, 125.4, 116.7, 38.6, 31.4, 28.8, 26.5, 22.5, 14.0. λ_{max} (CH_2Cl_2), 451 nm. λ_{em} (CH_2Cl_2), 571 nm.

2,2'-(2,2'-Bithiophene-5,5'-diyl)bis(5-cyclohexyl-5H-thieno-[3,2-c]pyrrole-4,6-dione), **C6cyc-NT4N**, **24d**.

Orange powder (40% yield). M.p. >300 °C. MS (70 eV, EI): m/z 632 ($M^{\cdot+}$). ^{1}H-NMR ($CDCl_3$, TMS/ppm): δ 7.31 (s, 2H), 7.25 (d, *J* = 4.0 Hz, 2H), 7.18 (d, *J* = 4.0 Hz), 4.00 (m, 2H), 2.14 (m, 4H), 1.79 (m, 12H), 1.30 (m, 4H). ^{13}C-NMR ($CDCl_3$, TMS/ppm): δ 163.9, 162.7,149.1, 145.1, 137.7, 126.7, 125.5, 125.3, 116.7, 116.5, 53.4, 51.5, 30.1, 29.7, 26.1, 25.1. λ_{max} (CH_2Cl_2), 444 nm. λ_{em} (CH_2Cl_2), 569 nm.

2,2'-(2,2'-Bithiophene-5,5'-diyl)bis(5-(2-ethylhexyl)-5H-thieno-[3,2-c]pyrrole-4,6-dione), **C6br-NT4N**, **24e**.

Red-orange solid (78% yield). M.p. 234 °C. (70 eV, EI): m/z 632 ($M^{\cdot+}$). ^{1}H-NMR ($CDCl_3$, TMS/ppm): δ 7.33 (s, 2H), 7.27 (d, *J* = 4.0 Hz, 2H), 7.19 (d, *J* = 4.0 Hz, 2H), 3.55 (t, 4H), 1.92 (m, 2H), 1.35 (m, 16H), 0.95 (m, 12H). ^{13}C-NMR ($CDCl_3$, TMS/ppm): δ 164.1, 162.9, 149.3, 145.2, 137.8, 137.6, 134.7, 126.8, 125.4, 116.7, 42.5, 38.4, 30.5, 28.5, 23.8, 23.0, 14.1, 10.4. λ_{max} (CH_2Cl_2), 451 nm. λ_{em} (CH_2Cl_2), 571 nm.

2,2'-([2,2'-Bithiophene]-5,5'-diyl)bis(5-octyl-4H-thieno[2,3-c]-pyrrole-4,6(5H)-dione), **C8-NT4N**, **24f**.

Orange powder (76% yield). M.p. 242 °C, MS (70 eV, EI): m/z 692 ($M^{\cdot+}$). ^{1}H-NMR ($CDCl_3$, TMS/ppm): δ 7.31 (s, 2H), 7.24 (d, *J* = 4.0 Hz, 2H), 7.16 (d, *J* = 3.6 Hz), 3.59 (t, 4H), 1.64 (m, 4H), 1.29 (m, 20H), 0.87 (t, 6H). ^{13}C-NMR ($CDCl_3$, TMS/ppm): δ 163.8, 162.6, 149.3, 145.2, 137.8, 137.6, 134.7, 126.8, 125.4, 116.6, 38.6, 31.8, 29.2, 29.1, 28.8, 26.8, 22.6, 14.1. λ_{max} (CH_2Cl_2), 450 nm. λ_{em} (CH_2Cl_2), 568 nm.

2,2'-(2,2'-bithiophene-5,5'-diyl)bis(5-pentyl-5H-thieno[3,2-c]pyrrole-4,6-dione), **C5-NT4N**, **24g**.

Orange powder (74% yield). M.p. 274 °C. MS (70 eV, EI): m/z 608 ($M^{\cdot+}$). ^{1}H-NMR ($CDCl_3$, TMS/ppm): δ 7.33 (s, 2H), 7.26 (d, *J* = 3.6 Hz, 2H), 7.18 (d, *J* = 4.0 Hz, 2H), 3.60 (t, 4H), 1.65 (m, 4H), 1.33 (m, 8H), 0.90 (t, 6H). ^{13}C-NMR ($CDCl_3$, TMS/ppm): δ 163.9, 162.7, 149.3, 145.3, 137.8, 137.6, 134.7, 126.8, 125.4, 116.7, 38.6, 28.9, 28.5, 22.3, 13.9. λ_{max} (CH_2Cl_2), 450 nm. λ_{em} (CH_2Cl_2), 570 nm.

General procedure for the synthesis of thienoimides 27a-g

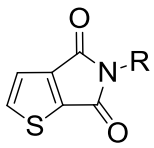

A solution of thieno[2,3-c]furan-4,6-dione (1 mmol) **25** and alkylamine **26a-f** (1.5 mmol) in toluene (0.1 M) was refluxed for 48 h then the solvent was removed. The solid so obtained (made by a mixture of the regioisomers 2-(alkylcarbamoyl)thiophene-3-carboxylic acid and 3- (alkylcarbamoyl)thiophene-2-carboxylic acid), was washed with pentane and used for the following intramolecular dehydration without further purification. The isomers mixture was refluxed for 5 h in $SOCl_2$, after that $SOCl_2$ was removed by distillation. The crude so obtained was purified by flash chromatography on silica gel to afford compounds **27a-f**.

5-Methyl-4H-thieno[2,3-c]pyrrole-4,6(5H)-dione, **27a**.

Pale beige solid (91% yield). MS (70 eV, EI): m/z 167 ($M\cdot^+$). ^{1}H-NMR ($CDCl_3$, TMS/ppm): δ 7.74 (d, *J* = 4.8 Hz, 1H), 7.30 (d, *J* = 4.8 Hz, 1H), 3.11 (s, 3H). ^{13}C-NMR ($CDCl_3$, TMS/ppm): δ 164.0, 162.8, 144.8, 140.9, 137.3, 121.1, 24.3.

5-Propyl-4H-thieno[2,3-c]pyrrole-4,6(5H)-dione, **27b**.

Pale beige solid (92% yield). MS (70 eV, EI): m/z 195 ($M\cdot^+$). ^{1}H-NMR ($CDCl_3$, TMS/ppm): δ 7.74 (d, *J* = 4.8 Hz, 1H), 7.30 (d, *J* = 4.8 Hz, 1H), 3.57 (t, 2H), 1.67 (m, 2H), 0.94 (t, 3H). ^{13}C-NMR ($CDCl_3$, TMS/ppm): δ 164.0, 162.8, 144.7, 140.9, 137.2, 121.1, 40.1, 22.1, 11.3.

5-Hexyl-4H-thieno[2,3-c]pyrrole-4,6(5H)-dione, **27c**.

Yellow oil (> 95% yield). MS (70 eV, EI): m/z 237 ($M\cdot^+$). ^{1}H-NMR ($CDCl_3$, TMS/ppm): δ 7.74 (d, *J* = 4.8 Hz, 1H), 7.29 (d, *J* = 4.8 Hz, 1H), 3.59 (t, 2H), 1.64 (m, 2H), 1.31 (m, 6H), 0.88 (t, 3H). ^{13}C-NMR ($CDCl_3$, TMS/ppm): δ 164.0, 162.8, 144.7, 140.9, 137.2, 121.1, 38.5, 31.4, 28.8, 26.5, 22.5, 14.0.

5-Cyclohexyl-4H-thieno[2,3-c]pyrrole-4,6(5H)-dione, **27d**.

White solid (83% yield). MS (70 eV, EI): m/z 235 ($M\cdot^+$). ^{1}H-NMR ($CDCl_3$, TMS/ppm): δ 7.71 (d, *J* = 4.8 Hz, 1H), 7.27 (d, *J* = 4.8 Hz, 1H), 3.99 (m, 1H), 2.13 (m, 2H), 1.77 (m, 2H), 1.74 (m, 3H), 1.33 (m, 3H). ^{13}C-NMR ($CDCl_3$, TMS/ppm): δ 164.0, 162.8, 144.5, 140.9, 137.0, 121.0, 51.3, 30.1, 26.0, 25.0.

5-2-ethylhexyl -4H-thieno[2,3-c]pyrrole-4,6(5H)-dione, **27e**.

Yellow oil (86% yield). MS (70 eV, EI): m/z 265 ($M\cdot^+$). ^{1}H-NMR ($CDCl_3$, TMS/ppm): δ 7.74 (d, *J* = 4.8 Hz, 1H), 7.30 (d, *J* = 4.8 Hz, 1H), 3.49 (d, *J* = 7.2 Hz, 2H), 1.78 (m, 1H), 1.30 (m, 8H), 0.89 (m, 6H). ^{13}C-NMR ($CDCl_3$, TMS/ppm): δ 164.5, 163.3, 144.9, 137.5, 137.3, 121.6, 121.1, 42.6, 38.5, 30.7, 28.7, 24.0, 23.2, 14.3, 10.7.

5-Octyl-4H-thieno[2,3-c]pyrrole-4,6(5H)-dione, **27f**.

Yellow oil (67% yield). MS (70 eV, EI): m/z 265 ($M^{\cdot+}$). ^{1}H-NMR ($CDCl_3$, TMS/ppm): δ 7.34 (d, *J* = 4.8 Hz, 1H), 7.30 (d, *J* = 4.8 Hz, 1H), 3.60 (t, 2H), 1.64 (m, 2H), 1.29 (m, 10H), 0.87 (t, 3H). ^{13}C-NMR ($CDCl_3$, TMS/ppm): δ 164.0, 162.8, 144.7, 140.9, 137.2, 121.1, 38.5, 31.8, 29.2, 28.8, 26.8, 22.6, 14.1.

5-pentyl-5H-thieno[2,3-c]pyrrole-4,6-dione, **27g**.

Yellow oil (89% yield). MS (70 eV, EI): m/z 223 ($M^{\cdot+}$). ^{1}H-NMR ($CDCl_3$, TMS/ppm): δ 7.74 (d, *J* = 4.8 Hz, 1H), 7.30 (d, *J* = 4.8 Hz, 1H), 3.59 (t, 2H), 1.65 (m, 2H), 1.33 (m, 4H), 0.89 (t, 3H). ^{13}C-NMR ($CDCl_3$, TMS/ppm): δ 164.0, 162.8, 144.7, 140.9, 137.2, 121.1, 38.5, 28.9, 28.5, 22.3, 13.9.

General procedure for the synthesis of brominated compounds 28a-g

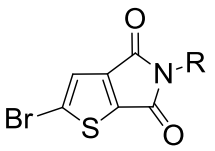

Thienoimide **27a-f** (1.41 mmol) was dissolved in TFA (6 ml). After cooling to 0 °C, 1 ml of concentrated H_2SO_4 was introduced into the reactor. NBS (1.37 mmol) was added to the mixture in small aliquots over 6 h. After stirring overnight at rt, the brown solution was diluted with 10 ml of water and extracted with CH_2Cl_2. The organic phase was dried over anhydrous Na_2SO_4 and evaporated under vacuum. The crude so obtained was purified by flash chromatography on silica gel to afford compounds **28a-f**.

2-Bromo-5-methyl-4H-thieno[2,3-c]pyrrole-4,6(5H)-dione, **28a**.

White solid (67% yield). MS (70 eV, EI): m/z 247 ($M^{\cdot+}$). ^{1}H-NMR ($CDCl_3$, TMS/ppm): δ 7.31 (s, 1H), 3.09 (s, 3H). ^{13}C-NMR ($CDCl_3$, TMS/ppm): δ 163.0, 162.0, 125.5, 123.8, 24.5.

2-Bromo-5-propyl-4H-thieno[2,3-c]pyrrole-4,6(5H)-dione, **28b**.

White solid (89% yield). MS (70 eV, EI): m/z 275 ($M^{\cdot+}$). ^{1}H-NMR ($CDCl_3$, TMS/ppm): δ 7.31 (s, 1H), 3.55 (t, 2H), 1.66 (m, 2H), 0.93 (t, 3H). ^{13}C-NMR ($CDCl_3$, TMS/ppm): δ 163.0, 162.0, 143.8, 140.4, 125.4, 123.8, 40.2, 22.0, 11.2.

2-Bromo-5-hexyl-4H-thieno[2,3-c]pyrrole-4,6(5H)-dione, **28c**.

Yellow oil (84% yield). MS (70 eV, EI): m/z 317 ($M^{\cdot+}$). ^{1}H-NMR ($CDCl_3$, TMS/ppm): δ 7.30 (s, 1H), 3.57 (t, 2H), 1.62 (m, 2H), 1.30 (m, 6H), 0.88 (t, 3H). ^{13}C-NMR ($CDCl_3$, TMS/ppm): δ 163.0, 162.0, 143.9, 140.5, 125.4, 123.8, 38.7, 31.3, 28.7, 26.4, 22.5, 14.0.

2-Bromo-5-cyclohexyl-4H-thieno[2,3-c]pyrrole-4,6(5H)-dione, **28d**.

Yellow oil (79% yield). MS (70 eV, EI): m/z 315 ($M^{\cdot+}$). ^{1}H-NMR ($CDCl_3$, TMS/ppm): δ 7.28 (s, 1H), 3.97 (m, 1H), 2.11 (m, 2H), 1.85 (m, 2H), 1.70 (m, 3H), 1.30 (m, 3H). ^{13}C-NMR ($CDCl_3$, TMS/ppm): δ 163.0, 162.0, 143.7, 140.5, 125.1, 123.7, 51.6, 30.0, 26.0, 25.0.

2-Bromo-5-ethylhexyl-4H-thieno[2,3-c]pyrrole-4,6(5H)-dione, **28e**.

White solid (78% yield). MS (70 eV, EI): m/z 345 ($M^{\cdot+}$). ^{1}H-NMR ($CDCl_3$, TMS/ppm): δ 7.31 (s, 1H), 3.48 (d, 3J = 7.2 Hz, 2H), 1.76 (m, 1H), 1.28 (m, 8H), 0.89 (m, 6H). ^{13}C-NMR ($CDCl_3$, TMS/ppm): δ 163.2, 162.2, 143.8, 125.4, 124.0, 123.6, 42.5, 38.3, 30.4, 28.4, 23.7, 22.9, 14.0, 10.4.

2-Bromo-5-octyl-4H-thieno[2,3-c]pyrrole-4,6(5H)-dione, **28f**.

White solid (88% yield). MS (70 eV, EI): m/z 345 ($M^{\cdot+}$). ^{1}H-NMR ($CDCl_3$, TMS/ppm): δ 7.30 (s, 1H), 3.57 (t, 2H), 1.62 (m, 2H), 1.27 (m, 10H), 0.87 (t, 3H). ^{13}C-NMR ($CDCl_3$, TMS/ppm): δ 163.0, 162.0, 143.9, 140.5, 125.4, 123.8, 38.7, 31.8, 29.2, 29.1, 28.7, 26.8, 22.6, 14.1.

2-bromo-5-pentyl-5H-thieno[2,3-c]pyrrole-4,6-dione, **28g**.

White solid (87% yield). MS (70 eV, EI): m/z 302 ($M^{\cdot+}$). ^{1}H-NMR ($CDCl_3$, TMS/ppm): δ 7.30 (s, 1H), 3.57 (t, 2H), 1.63 (m, 2H), 1.32 (m, 4H), 0.89 (t, 3H). ^{13}C-NMR ($CDCl_3$, TMS/ppm): δ 163.0, 162.0, 143.9, 140.5, 125.4, 123.8, 38.7, 28.9, 28.4, 22.2, 13.9.

5.2.5 Synthesis of compounds 30-48

Synthesis of compound 30 and precursors (34-35)

(E)-2,20-(5,50-(Ethene-1,2-diyl)bis(thiophene-5,2-diyl))bis(5-hexyl-4H-thieno[2,3-c]pyrrole-4,6(5H)-dione), **NTE**, **30**. Conventional Stille cross-coupling reaction between **28c** and **35**.

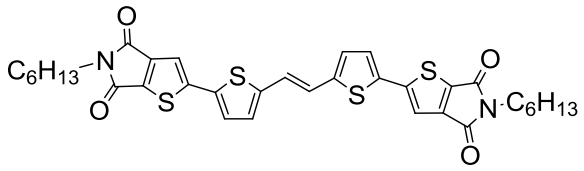

Dark red solid (57% yield). M.p. 255°C. MS (70 eV, EI): m/z 662 ($M^{\cdot+}$). ^{1}H-NMR ($CDCl_3$, TMS/ppm): δ 7.31 (s, 2H), 7.23 (d, *J* = 4.0 Hz, 2H), 7.04 (d, *J* = 4.0 Hz, 2H), 7.02 (s, 2H), 3.60 (t, 4H), 1.64 (m, 4H), 1.31 (m, 12H), 0.88 (m, 6H); ^{13}C-NMR ($CDCl_3$, TMS/ppm): δ 163.9, 162.7, 149.8, 145.3, 143.7, 137.3, 134.3, 128.0, 126.7, 122.1, 116.5, 38.6, 31.4, 28.8, 26.5, 22.5, 14.0. λ_{max} (CH_2Cl_2), 465 nm. λ_{em} (CH_2Cl_2), 588 nm.

(E)-1,2-Di(thiophen-2-yl)ethane, **34**.

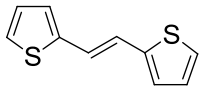

According to a method of Karminski-Zamola and co-workers,[2] titanium (IV) chloride (2.86 ml, 26 mmol) was added dropwise, over a period of 30 min, to a well-stirred suspension of commercial 2-thiophenecarboxaldehyde **33** (2.46 g, 22 mmol) in THF (40 ml) at -18 °C. After stirring at this temperature for 30 min, zinc powder (3.43 g, 53 mmol), previously carefully dried under vacuum, was added in small portions over a period of 30 min. The mixture was stirred at -18 °C for 30 min, warmed to rt, and finally refluxed for 3.5 h. The reaction was quenched by addition of ice water (40 ml) and the resulting solid was collected by filtration and dried. The solid was dissolved in CH_2Cl_2 (30 ml) and the insoluble inorganic material removed by filtration. The organic portions were dried over Na_2SO_4 followed by solvent evaporation under vacuum. The residue was purified by flash chromatography on silica gel to afford pure E isomer **34** (1.30 g, 31% yield).

M.p. 133-134 °C. MS (70 eV, EI): m/z 192 ($M^{\cdot+}$); ^{1}H-NMR ($CDCl_3$, TMS/ppm): δ 7.19-7.17 (dt, 2H), 7.05 (s, 2H), 7.04-7.03 (dd, 2H), 7.00-6.98 (dd, 2H); ^{13}C-NMR ($CDCl_3$, TMS/ppm): δ 142.4, 127.6, 126.0, 124.3, 121.4.

(E)-1,2-Bis(5-(tributylstannyl)thiophen-2-yl)ethane, **35**.

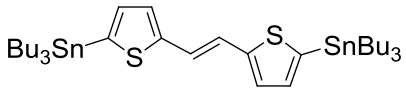

According to the method described by Sonar and co-workers,[3] to a solution of **34** (0.90 g, 4.69 mmol) in THF (25 ml), TMEDA (1.57 ml, 10.30 mmol) was added at -50 °C. After cooling to -78 °C, a 2.5 M solution of *n*-BuLi (4.31 ml, 10.80 mmol) was added dropwise. The mixture was then refluxed for 1 h. The reaction was cooled to -78 °C and Bu_3SnCl (2.76 ml, 9.80 mmol) was added. The solution was warmed to rt and stirred overnight. The solvent was removed in vacuo, then the crude was dissolved in CH_2Cl_2 and washed twice with H_2O. After drying over Na_2SO_4 and evaporating the solvent under vacuum, the TM was obtained as a light brown oil in 98% yield. The material, quite pure (^{1}H NMR), was used without purification in the subsequent step. MS (70 eV, EI): m/z 770 ($M^{\cdot+}$). ^{1}H-NMR ($CDCl_3$, TMS/ppm): δ 7.12 (d, *J* = 3.2 Hz, 2H), 7.10 (s, 2H), 7.04 (d, *J* = 3.2 Hz, 2H), 1.55 (m, 12H), 1.33 (m, 12H), 1.11 (m, 12H), 0.91 (m, 18H).

Synhesis of compound 31 and precursors (36-44)

(E)-5-Hexyl-2-(5-(((5-(5-hexyl-4,6-dioxo-5,6-dihydro-4H-thieno-[2,3-c]pyrrol-2-yl)thiophen-2-yl)imino)methyl)thiophen-2-yl)-4Hthieno[2,3-c]pyrrole-4,6(5H)-dione, **NTI**, **31**.

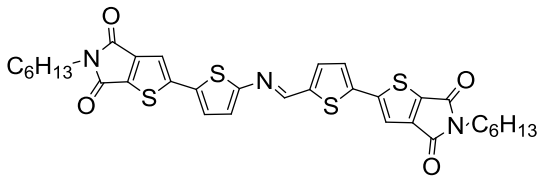

According to the method described by Skene and coworkers,[41] to a mixture of the aminothiophene derivative **41** (50 mg, 0.15 mmol) and carbaldehyde **44** (62 mg, 0.18 mmol) in *i*-PrOH (5 mL), a catalytic amount of TFA was added under stirring. The reaction mixture was then heated to reflux for 6 h under N_2 atmosphere, under stirring. Complete removal of the solvent led to a dark red solid, which was washed in *n*-pentane. After crystallization from toluene-pentane mixture the product was obtained as a red powder (89 mg, 90% yield).

M.p. 256 °C. MS (70 eV, EI): m/z 663 ($M^{\cdot+}$). ^{1}H-NMR ($CDCl_3$, TMS/ppm): δ 8.48 (s, 1H), 7.44 (d, *J* = 4.0 Hz, 1H), 7.43 (s, 1H), 7.35 (d, *J* = 4.0 Hz, 1H), 7.32 (s, 1H), 7.24 (d, *J* = 4.0 Hz, 1H), 7.10 (d, *J* = 4.0 Hz, 1H) 3.60 (m, 4H), 1.64 (m, 4H), 1.31 (m, 12H), 0.88 (m, 6H); ^{13}C-NMR ($CDCl_3$, TMS/ppm): δ 163.9, 163.7, 162.7, 162.5, 155.1, 150.3, 149.1, 145.2, 143.1, 140.0, 138.7, 137.4, 133.3, 131.2, 126.5, 125.8, 125.8, 117.7, 116.5, 38.7, 38.6, 31.4, 28.8, 28.7, 26.5, 22.5, 14.0.

Methyl thiophene-2-carboxylate, **36**.

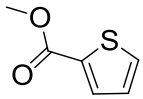

To a solution of commercial 2-thiophenecarboxylic acid, **35** (1.0 g, 7.8 mmol) in 50 ml of anhydrous MeOH under N_2 atmosphere, $SOCl_2$ (1.13 ml, 15.60 mmol) was added dropwise at 0 °C. The mixture was heated to reflux for 5 h. The solvent was removed, and the crude product purified by flash chromatography on silica gel to yield 890 mg (80%) of a colorless oil.

MS (70 eV, EI): m/z 142 ($M^{\cdot+}$). ^{1}H-NMR ($CDCl_3$, TMS/ppm): δ 7.80 (dd, *J* = 4.0, 1.6 Hz, 1H), 7.55 (dd, *J* = 5.2, 1.2 Hz, 1H), 7.10 (dd, *J* = 4.8, 4.0 Hz, 1H), 3.89 (s, 3H). ^{13}C-NMR ($CDCl_3$): δ 162.7, 133.6, 133.4, 132.3, 127.7, 52.1.

Methyl 5-(tributylstannyl)thiophene-2-carboxylate, **37**.

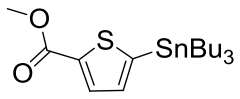

To a stirred 2 M solution of LDA (2.5 ml, 5.04 mmol) at -78 °C under N_2 atmosphere a solution of compound **36** (0.6 g, 4.2 mmol) in dry THF (3 ml) was added dropwise. After 1 hour, a solution of Bu_3SnCl (1.5 ml, 4.62 mmol) in dry THF (4 ml) was added dropwise. After being stirred at -78 °C for further 2 h, the mixture was allowed to warm to rt, and the reaction was kept under stirring overnight. The resulting mixture was evaporated under

reduced pressure, then diluted with CH_2Cl_2, and washed twice with H_2O. After drying over Na_2SO_4 and evaporation of the solvent, the residue was purified by distillation (142-150 °C, 0.1 mmHg) to give the TM (725 mg, 40% yield) as a pale yellow oil.

MS (70 eV, EI): m/z 142 ($M^{\cdot+}$). ^{1}H-NMR ($CDCl_3$, TMS/ppm): δ 7.88 (d, *J* = 3.6 Hz, 1H), 7.15 (d, *J* = 3.6Hz, 1H), 3.88 (s, 3H), 1.55 (m, 6H), 1.33 (m, 6H), 1.12 (m, 6H), 0.89 (t, 9H). ^{13}C-NMR ($CDCl_3$): δ 162.6, 147.3, 138.6, 135.7, 134.1, 52.0, 28.8, 27.2,13.6, 10.9.

Methyl 5-(5-hexyl-4,6-dioxo-5,6-dihydro-4H-thieno[2,3-c]pyrrol-2-yl)thiophene-2-carboxylate, **38**. Conventional Stille cross-coupling reaction between brominated thienoimide derivative **28c** and compound **37**.

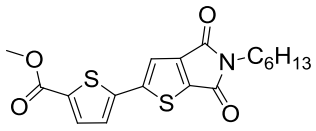

Pale yellow powder (80% yield). MS (70 eV, EI): m/z 377 ($M^{\cdot+}$). ^{1}H-NMR ($CDCl_3$, TMS/ppm): δ 7.74 (d, *J* = 4.0 Hz 1H), 7.41 (s, 1H), 7.29 (d, *J* = 4.0 Hz 1H), 3.92 (s, 3H), 3.61 (t, 2H), 1.64 (m, 2H), 1.31 (m, 6H), 0.88 (t, 3H). ^{13}C-NMR ($CDCl_3$): δ 163.7, 163.2, 161.9, 148.6, 145.1, 141.2, 134.2, 126.1, 117.9, 108.4, 52.5, 38.7, 31.3, 28.7, 26.4, 22.5, 14.0.

5-(5-Hexyl-4,6-dioxo-5,6-dihydro-4H-thieno[2,3-c]pyrrol-2-yl)thiophene-2-carboxylic acid, **39**.

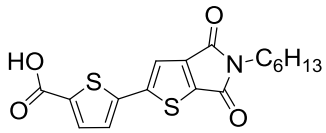

To a solution of **38** (180 mg, 0.48 mmol) in MeOH (4 ml), 1 N aq. NaOH (4 ml) was added dropwise at rt. The mixture was refluxed for 2 h. Methanol was removed under vacuum, then 4 ml of H_2O was added. The resulting mixture was brought to a pH below 2 with HCl, and the white solid formed was centrifuged, washed 2 times with H_2O and dried at 50 °C. The solid was refluxed for 3 h in $SOCl_2$ (10 ml), then the solvent was removed by distillation. H_2O (10 ml) was added dropwise, and the yellow solid formed was dissolved in CH_2Cl_2 (10 ml). The organic phase was extracted and then washed with H_2O, evaporated under vacuum and dried. The TM **39** was obtained as a yellow powder (170 mg, 98% yield). MS (70 eV, EI): m/z 363 ($M^{\cdot+}$). ^{1}H-NMR ($CDCl_3$, TMS/ppm): δ 7.92 (d, *J* = 4.0 Hz 1H), 7.49 (s, 1H), 7.36 (d, *J* = 4.4 Hz 1H), 3.61 (t, 2H), 1.63 (m, 2H), 1.30 (m, 6H), 0.87 (t, 3H). ^{13}C-NMR ($CDCl_3$): δ 163.3, 162.2, 159.2, 147.2, 146.1, 145.1, 140.3, 138.4, 137.3, 126.5, 119.0, 38.8, 31.3, 28.7, 26.4, 22.5, 14.0.

Tert-butyl (5-(5-hexyl-4,6-dioxo-5,6-dihydro-4H-thieno[2,3-c]pyrrol-2-yl)thiophen-2-yl)carbamate, **40**.

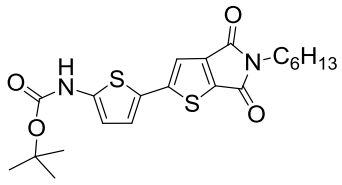

To a solution of compound **39** (176 mg, 0.48 mmol) and TEA (48 mg, 0.48 mmol) in *t*-BuOH (3 ml), DPPA (134 mg, 0.49 mmol) was added dropwise at rt. After refluxing for 6 h, the reaction was quenched with H_2O. The mixture was extracted with CH_2Cl_2 and the combined organic layers were washed three time with H_2O, dried over Na_2SO_4, filtered and concentrated under vacuum. The crude product was purified by flash chromatography on silica gel to give the TM as an orange-red solid (88 mg, 42% yield). MS (70 eV, EI): m/z 434 ($M^{\cdot+}$). ^{1}H-NMR ($CDCl_3$, TMS/ppm): δ 7.51 (bs, 1H), 7.16 (s, 1H), 7.04 (d, *J* = 4.0 Hz, 1H), 6.43 (d, *J* = 4.0 Hz, 1H), 3.56 (t, 2H), 1.61 (m, 2H), 1.52 (s, 9H), 1.30 (m, 6H), 0.88 (t, 3H). ^{13}C-NMR ($CDCl_3$): δ 164.1, 163.0, 152.0, 145.3, 142.5, 135.6, 129.8, 125.8, 123.8, 114.0, 38.4, 31.3, 29.6, 28.7, 28.2, 26.4, 22.5, 14.0.

2-(5-Aminothiophen-2-yl)-5-hexyl-4H-thieno[2,3-c]pyrrole-4,6(5H)-dione, **41**.

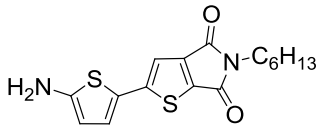

To a 10 ml CH_2Cl_2 solution of **40** (80 mg, 0.18 mmol), were added 10 ml of TFA under stirring. After 5 h at rt, the solution was brought to basic pH by adding 1N aq. NaOH. The organic phase was washed with H_2O until reaching neutral pH, dried over anhydrous Na_2SO_4, and evaporated in vacuo to give compound **41** in almost quantitative yield (60 mg) as a red solid. The product was stored at 4 °C under N_2 atmosphere, and used after short time for the subsequent reaction. MS (70 eV, EI): m/z 334 ($M^{\cdot+}$). ^{1}H-NMR ($CDCl_3$, TMS/ppm): δ 7.05 (s, 1H), 6.95 (d, *J* = 4.0 Hz, 1H), 6.11 (d, *J* = 4.0 Hz, 1H), 4.08 (bs, 2H), 3.57 (t, 2H), 1.60 (m, 2H), 1.28 (m, 6H), 0.87 (t, 3H).

2-(Thiophen-2-yl)-1,3-dioxolane, **42**.

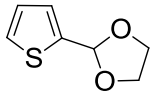

According to the method described by Johnson,[5] a mixture of commercial 2-thiophenecarboxaldehyde, **33** (1.00 g, 8.93 mmol), ethylene glycol (1.30 g, 21 mmol), and *p*-TsOH (22 mg) in fluorobenzene (9 ml), was stirred under reflux for 5 h. In the course of the reaction, water formed was removed by azeotropic distillation. After purification of the crude by distillation (55-58 °C, 0.1 mmHg) the TM was obtained as a pale yellow oil (1.06 g, 76% yield).

MS (70 eV, EI): m/z 156 ($M^{\cdot+}$). ^{1}H-NMR ($CDCl_3$, TMS/ppm): δ 7.31 (dd, *J* = 4.8, 1.2, 0.4 Hz, 1H), 7.15 (ddd, *J* = 3.6, 1.2, 0.4 Hz, 1H), 6.97 (dd, *J* = 4.8, 3.2 Hz, 1H), 6.12 (s, 1H), 4.08 (m, 4H).

(5-(1,3-Dioxolan-2-yl)thiophen-2-yl)tributylstannane, **43**.

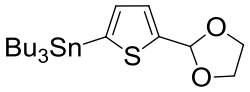

n-BuLi (2.5 M in hexanes, 3 ml, 7.44 mmol) was added dropwise to a solution of **42** (0.97 g, 6.20 mmol) in anhydrous THF (15 ml) at -78 °C. The mixture was stirred for 2 h at this temperature, then Bu_3SnCl (1.68 ml, 6.20 mmol) was added, and the reaction was left under stirringfor 16 h at rt. The solvent was removed in vacuo then the mixture was dissolved in Et_2O and washed with H_2O. the organic layer was dried over Na_2SO_4, and the solvent evaporated to afford the product as a brown oil (2.70 g; yield 98%). MS (70 eV, EI): m/z 446 ($M^{\cdot+}$). ^{1}H-NMR ($CDCl_3$, TMS/ppm): δ 7.28 (d, *J* = 3.0 Hz, 1H), 7.05 (d, *J* = 3.2 Hz, 1H), 6.15 (s, 1H), 4.09 (m, 4H), 1.55 (m, 6H), 1.32 (m, 12H), 1.08 (m, 6H), 0.89 (t, 9H).

5-(5-Hexyl-4,6-dioxo-5,6-dihydro-4H-thieno[2,3-c]pyrrol-2-yl)thiophene-2-carbaldehyde, **44**.

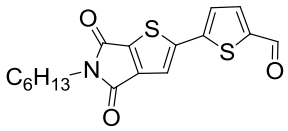

Conventional Stille cross-coupling reaction between brominated thienoimide derivative **28c** and compound **43**.

Yellow powder (98% yield). MS (70 eV, EI): m/z 347 ($M^{\cdot+}$). ^{1}H-NMR ($CDCl_3$, TMS/ppm): δ 9.90 (s, 1H), 7.72 (d, *J* = 4.4 Hz 1H), 7.46 (s, 1H), 7.39 (d, *J* = 4.0 Hz 1H) 3.59 (m, 2H), 1.62 (m, 2H), 1.29 (m, 6H), 0.88 (t, 3H); ^{13}C-NMR ($CDCl_3$): δ 182.3, 163.4, 162.2, 148.0, 145.0, 144.0, 143.8, 139.8, 136.7, 126.3, 118.6, 38.7, 31.3, 28.6, 26.4, 22.5, 13.9.

Synhesis of compound 32 and precursors (47-48)

2,20-(5,50-(Ethyne-1,2-diyl)bis(thiophene-5,2-diyl))bis(5-hexyl-4H-thieno[2,3-c]pyrrole-4,6(5H)-dione), **NTA**, **32**.

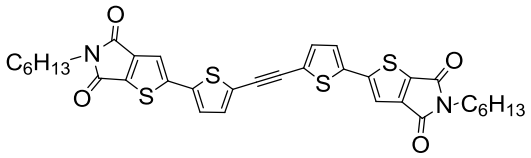

To a refluxing toluene solution (15 mL) of bromo thienoimide **28c** (348 mg, 1.10 mmol) and in situ prepared catalyst $Pd(AsPh_3)_4$ (10 mol%, i.e. 52 mg of Pd_2dba_3 and 122 mg of $AsPh_3$) under N_2 atmosphere, bistannane derivative **48** (384 mg, 0.50 mmol) was added dropwise. The solution was refluxed for 24 h, then the solvent was removed under vacuum, and the crude product was washed in pentane. The residue was purified by flash chromatography. Due to its strong retention on silica gel, the title compound was finally eluted with hot toluene. The fractions containing the TM **32** were combined, the solvent evaporated, and the residue crystallized from toluene giving an orange powder (225 mg, 68% yield).

M.p. 228 °C. MS (70 eV, EI): m/z 660 ($M^{\cdot+}$). ^{1}H-NMR ($CDCl_3$, TMS/ppm): δ 7.34 (s, 2H), 7.25 (d, *J* = 4.0 Hz, 2H), 7.24 (d, *J* = 4.0 Hz, 2H), 3.60 (t, 4H), 1.62 (m, 4H), 1.31 (m, 12H), 0.88 (m, 6H). ^{13}C-NMR

($CDCl_3$, TMS/ppm): δ 163.8, 162.6, 148.9, 145.2, 138.1, 137.1, 133.5, 125.9, 124.0, 117.1, 88.1, 38.7, 31.4, 28.7, 26.5, 22.5, 14.0. λ_{max} (CH_2Cl_2), 433 nm. λ_{em} (CH_2Cl_2), 547 nm.

1,2-Di(thiophen-2-yl)ethyne, **47**.

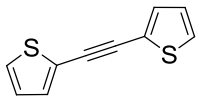

According to the method described by *Brisbois* and coworkers,[6] a dry round-bottom flask was charged with $PdCl_2(PPh_3)_2$ (210 mg, 6 mol%), CuI (190 mg, 10 mol%), and 2-iodothiophene (1.02 ml, 10 mmol). While stirring, dry benzene (50 ml) was added by syringe. DBU (8.97 ml, 60 mmol) was then added under argon atmosphere. Ice-chilled trimethylsilylacetilene (0.69 ml, 5 mmol) was added, immediately followed by H_2O (73 µL, 4 mmol). The reaction was carried out in absence of light for 18 h at rt, then the mixture was partitioned in Et_2O and H_2O. The organic layer was washed three times with aqueous HCl (10% v/v), once with saturated NaCl, and then dried over Na_2SO_4. Removal of the solvent under vacuum yielded a crude product that was purified by flash chromatography on silica gel. 984 mg (72% yield) of a white crystalline solid were obtained. M.p. 101 °C (lit. 96 °C). MS (70 eV, EI): m/z 190 ($M\cdot^+$). ^{1}H-NMR ($CDCl_3$, TMS/ppm): δ 7.31 (dd, *J* = 5.2, 1.2 Hz, 2H), 7.28 (dd, *J*= 3.6, 1.2 Hz, 2H), 7.02 (dd, *J*= 5.2, 3.6 Hz, 2H); ^{13}C-NMR ($CDCl_3$): δ 132.1, 127.6, 127.1, 122.9, 86.2.

1,2-Bis(5-(tributylstannyl)thiophen-2-yl)ethyne, **48**.

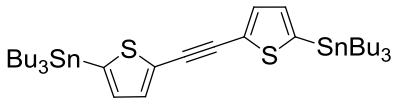

To a solution of compound **47** (190 mg, 1 mmol) in dry Et_2O (12 ml) *n*-BuLi (0.92 ml, 2.30 mmol) was added at rt. After 1 h, Bu_3SnCl (0.57 ml, 2.10 mmol) was added dropwise. The reaction mixture was left under stirring at rt for 4h, then quenched with H_2O and extracted with EtOAc. The organic layer was washed twice with saturated NaCl and dried over Na_2SO_4. After removal of the solvent in vacuo the title compound was obtained in semi-quantitative yield, and used without further purification for the final synthetic step.

Yellow-amber oil. MS (70 eV, EI): m/z 768 ($M\cdot^+$). ^{1}H-NMR ($CDCl_3$, TMS/ppm): δ 7.36 (d, ^3J= 3.2 Hz, 2H), 7.05 (d, ^3J= 3.2 Hz, 2H), 1.55 (m, 12H), 1.33 (m, 12H), 1.12 (m, 12H), 0.91 (m, 18H).

5.2.6 Synthesis of compounds 50-62

Direct arylation reaction for the synthesis of compound 50

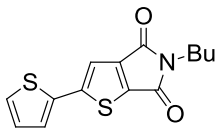

K_2CO_3 (1.5 mmol), $Pd(OAc)_2$ (6 mol%), PCy_3HBF_4 (12 mol%) and pivOH (30 mol%) were added in the reaction flask under N_2 atmosphere. Compound **27h** (1.2 mmol) was added dissolved into dry toluene (0.1 M). 2-Bromothiophene **49** (1 mmol) was added and the reaction mixture was stirred at reflux for 24 h. The reaction mixture was then cooled to rt and diluted with H_2O. The organic layers were extracted with CH_2Cl_2, dried over Na_2SO_4 and then evaporated under reduced pressure. The crude product was purified by flash chromatography on silica gel followed by crystallization to get the TM **50** as a yellow powder[7] (70% yield).

General direct arylation reaction for the synthesis of compounds 19-20 (NT3N-NT5N) of section 3.3

K_2CO_3 (1.5 mmol), $Pd(OAc)_2$ (6 mol%), PCy_3HBF_4 (12 mol%) and pivOH (30 mol%) were added in the reaction flask under N_2 atmosphere. The SM **27h** or **50** (2.4 mmol) was added dissolved into dry toluene (0.1 M). 2,5-Dibromothiophene **51** (1 mmol) was added and the reaction mixture was stirred at reflux for 24 h. The reaction mixture was then cooled to rt and diluted with H_2O. The organic layers were extracted with CH_2Cl_2, dried over Na_2SO_4 and then evaporated under reduced pressure. The crude product was purified by flash chromatography on silica gel followed by crystallization to get the TM **19**-**20** as a powder (NT3N, **19**, 30% yield; NT5N, **20**, 25% yield). Characterization in section 5.2.3.

Direct arylation reaction for the synthesis of compounds 52a-c

K_2CO_3 (3 mmol), $Pd(OAc)_2$ (6 mol%) and PCy_3HBF_4 (12 mol%) were added in the reaction flask under N_2 atmosphere. 3,4-thienoimide (1 mmol) was added dissolved into dry toluene (0.1 M). Brominated derivatives **53a-c** (2.1 mmol) were added and the reaction mixture was stirred at reflux for 24 h. The reaction mixture was then cooled to rt and diluted with H_2O. The organic layers were extracted with CH_2Cl_2, dried over Na_2SO_4 and then evaporated under reduced pressure. The crude product was purified by flash chromatography on silica gel followed by crystallization to get the target materials **52a-c** as powders.

1,3-di(biphenyl-4-yl)-5-butyl-5H-thieno[3,4-c]pyrrole-4,6-dione, **52a**.

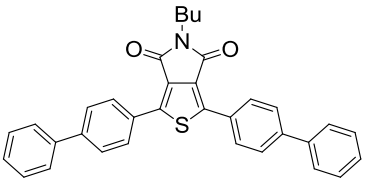

Yellow solid (65% yield). M.p. 178 °C. MS (70 eV, EI): m/z 513 ($M\cdot^+$). ^{1}H-NMR ($CDCl_3$, TMS/ppm): δ 8.24 (d, *J* = 8.4 Hz, 4H), 7.72 (d, *J* = 8.4 Hz, 4H), 7.65 (d, *J* = 7.2 Hz, 4H), 7.48 (t, *J* = 7.2 Hz, 4H), 7.40 (t, *J* = 7.2 Hz, 2H), 3.72 (t, *J* = 7.2 Hz, 2H), 1.70 (m, 2H), 1.41 (m, 2H), 0.97 (m, 3H). ^{13}C-NMR ($CDCl_3$, TMS/ppm): δ 163.1, 144.6, 142.9, 140.1, 130.5, 129.5, 128.9, 128.6, 127.9, 127.6, 127.1, 38.4, 30.5, 20.2, 13.7. λ_{max} (CH_2Cl_2), 366 nm. λ_{em} (CH_2Cl_2), 432, 447 nm.

5-butyl-1,3-bis(5'-hexyl-2,2'-bithiophen-5-yl)-5H-thieno[3,4-c]pyrrole-4,6-dione, **52b**.

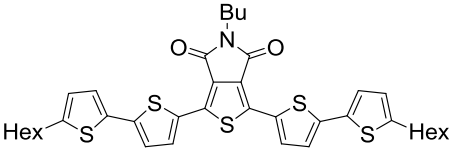

Orange solid (63% yield). M.p. 93 °C. MS (70 eV, EI): m/z 705 ($M\cdot^+$). ^{1}H-NMR ($CDCl_3$, TMS/ppm): δ 7.90 (d, *J* = 4.0 Hz, 2H), 7.09 (d, *J* = 3.6 Hz, 2H), 7.08 (d, *J* = 4.0 Hz, 2H), 6.71 (d, *J* = 3.2 Hz, 2H), 3.68 (t, *J* = 7.2 Hz, 2H), 2.81 (t, *J* = 7.2 Hz, 4H), 1.69 (m, 6H), 1.35 (m, 14H), 0.96 (t, *J* = 7.2 Hz, 3H), 0.90 (t, *J* = 7.2 Hz, 6H). ^{13}C-NMR ($CDCl_3$, TMS/ppm): δ 162.6, 147.0, 141.4, 135.9, 133.7, 130.8, 130.3, 128.0, 125.1, 124.6, 123.8, 38.3, 31.5, 31.4, 30.6, 30.2, 28.7, 22.6, 20.2, 14.1, 13.7. λ_{max} (CH_2Cl_2), 461 nm. λ_{em} (CH_2Cl_2), 536 nm.

2,2'-(5,5'-(5-butyl-4,6-dioxo-5,6-dihydro-4H-thieno[3,4-c]pyrrole-1,3-diyl)bis(thiophene-5,2-diyl))bis(5-hexyl-5H-thieno[2,3-c]pyrrole-4,6-dione), **52c**.

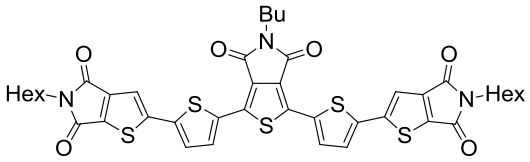

Red solid (67% yield). M.p. 267 °C. MS (70 eV, EI): m/z 843 ($M\cdot^+$). ^{1}H-NMR ($CDCl_3$, TMS/ppm): δ 7.97 (d, *J* = 4.0 Hz, 2H), 7.42 (s, 2H), 7.34 (d, *J* = 4.0 Hz, 2H), 3.70 (t, *J* = 7.2 Hz, 2H), 3.61 (t, *J* = 6.8 Hz, 4H), 1.67 (m, 6H), 1.36 (m, 14H), 0.97 (t, *J* = 6.8 Hz, 3H), 0.89 (m, 6H). ^{13}C-NMR ($CDCl_3$, TMS/ppm): δ 163.7, 162.6, 162.4, 148.7, 145.2, 138.5, 138.2, 135.4, 133.5, 131.0, 129.8, 126.9, 117.5, 38.7, 38.5, 31.4, 30.5, 28.7, 26.5, 22.5, 20.2, 14.0, 13.7. λ_{max} (CH_2Cl_2), 464 nm. λ_{em} (CH_2Cl_2), 538 nm.

General MW assisted direct arylation reaction for the synthesis of compounds 54a-f

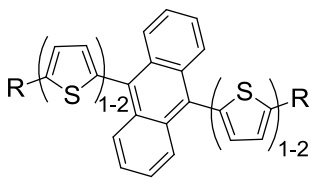

The MW vessel was charged with 9,10-dibromoanthracene **55** (1 mmol), DMF (0.1 M), $Pd(OAc)_2$ (6 mol%), PCy_3HBF_4 (12 mol%), PivOH (30 mol%), K_2CO_3 (1.5 mmol) and the proper thienyl derivative **56**-**61** (2.2 mmol for **57**,**58** and **60**,**61**; 5 mmol for **56** and **59**). The vessel was capped and the mixture was irradiated with MW fixing the temperature at 150°C for 5 minutes. Then the solvent

was removed under vacuum and the crude was dissolved in CH_2Cl_2, washed with water and extracted. The combined organic phases were dried over Na_2SO_4, the solvent evaporated under vacuum and the so obtained crude purified by flash chromatography on silica gel.

9,10-Bis(thiophen-2-yl)anthracene, **DTA**, **54a**.

Pale yellow solid (31% yield). M.p. 259 °C. MS (70 eV, EI): m/z 342 ($M^{\cdot+}$). ^{1}H-NMR ($CDCl_3$, TMS/ppm): δ 7.90-7.88 (m, 4H), 7.64 (dd, *J* = 5.2, 1.2 Hz, 2H), 7.43-7.41 (m, 4H), 7.33 (dd, *J* = 5.2, 3.6 Hz, 2H), 7.23 (dd, *J* = 3.6, 1.2 Hz, 2H). ^{13}C-NMR ($CDCl_3$, TMS/ppm): δ 139.2, 131.7, 130.5, 129.8, 127.4, 127.0, 126.9, 125.9. λ_{max} (CH_2Cl_2), 399 nm. λ_{em} (CH_2Cl_2), 446 nm.

9,10-Bis(5-hexylthiophen-2-yl)anthracene, **H-DTA**, **54b**.

Light yellow solid (81% yield). M.p. 115 °C.; MS (70 eV, EI): m/z 510 ($M^{\cdot+}$). ^{1}H-NMR ($CDCl_3$, TMS/ppm): δ 7.98-7.95 (m, 4H), 7.43-7.40 (m, 4H), 7.00 (d, *J* = 3.2 Hz, 2H), 6.97 (d, *J* = 3.2 Hz, 2H), 2.97 (t, 4H), 1.83 (m, 4H), 1.49 (m, 4H), 1.39 (m, 8H), 0.94 (m, 6H). ^{13}C-NMR ($CDCl_3$, TMS/ppm): δ 147.4, 136.1, 131.5, 130.6, 129.1, 126.8, 125.5, 123.9, 31.7, 31.6, 30.3, 28.9, 22.6, 14.1. λ_{max} (CH_2Cl_2), 400 nm. λ_{em} (CH_2Cl_2), 455 nm.

9,10-Bis(5-(perfluorohexyl)thiophen-2-yl)anthracene, **F-DTA**, **54c**.

Pale yellow solid (70% yield). M.p. 141 °C. MS (70 eV, EI): m/z 978 ($M^{\cdot+}$). ^{1}H-NMR ($CDCl_3$, TMS/ppm): δ 7.81-7.79 (m, 4H), 7.67 (m, 2H) 7.50-7.47 (m, 4H), 7.25 (m, 2H). ^{19}F-NMR ($CDCl_3$, $CFCl_3$/ppm) δ -80.8 (m, 6F), -101.0 (m, 4F), -121.4 (m, 8F), -122.7 (m, 4F), -126.0 (m, 4F). ^{13}C-NMR ($CDCl_3$, TMS/ppm): δ 144.4, 131.1, 130.8, 130.6, 129.9, 128.7, 126.5, 126.1. λ_{max} (CH_2Cl_2), 399 nm. λ_{em} (CH_2Cl_2), 446 nm.

9,10-Bis([2,2'-bithiophen]-5-yl)anthracene, **DTTA**, **54d**.

Yellow-green solid (74% yield). M.p. 318 °C. MS (70 eV, EI): m/z 506 ($M^{\cdot+}$). ^{1}H-NMR ($CDCl_3$, TMS/ppm): δ 8.04-8.01 (m, 4H), 7.47-7.44 (m, 4H), 7.40 (d, *J* = 3.6 Hz, 2H), 7.29 (m, 2H), 7.27 (s, 2H), 7.13 (d, *J* = 3.6 Hz, 2H), 7.07 (dd, *J* = 4.8, 4.0 Hz, 2H); ^{13}C-NMR ($CDCl_3$, TMS/ppm): δ 138.9, 137.8, 137.2, 131.4, 130.4, 129.8, 126.6, 125.9, 124.5, 123.9, 123.8. λ_{max} (CH_2Cl_2), 402 nm. λ_{em} (CH_2Cl_2), 487 nm.

9,10-Bis(5'-hexyl-[2,2'-bithiophen]-5-yl)anthracene, **H-DTTA**, **54e**.

Yellow solid (76% yield). M.p. 212 °C MS (70 eV, EI): m/z 674 ($M^{\cdot+}$). ^{1}H-NMR ($CDCl_3$, TMS/ppm): δ 8.04-8.01 (m, 4H), 7.45-7.42 (m, 4H), 7.31 (d, *J* = 3.6 Hz, 2H), 7.09 (d, *J* = 3.6 Hz, 2H), 7.08 (d, *J* = 3.6 Hz, 2H), 6.73 (d, *J* = 3.6 Hz, 2H), 2.84 (t, 4H), 1.72 (m, 4H), 1.41 (m, 4H), 1.34 (m, 8H), 0.91 (m, 6H).

^{13}C-NMR ($CDCl_3$, TMS/ppm): δ 145.6, 139.5, 137.1, 134.5, 131.4, 130.3, 129.9, 126.7, 125.8, 124.8, 123.5, 123.0, 31.62, 31.59, 30.2, 28.7, 22.6, 14.1. λ_{max} (CH_2Cl_2), 403 nm. λ_{em} (CH_2Cl_2), 492 nm.

9,10-Bis(5'-(perfluorohexyl)-[2,2'-bithiophen]-5-yl)anthracene, **F-DTTA**, **54f**.

Light yellow solid (60% yield). M.p. 248 °C. MS (70 eV, EI): m/z 873 ($M^{\cdot+}$-269). Note: because the molecular weight exceeds the operating limit of the spectrometer, no peak can be detected at m/z 1142, which would correspond to the mass of the target compound. However the observed fragmentation pattern appears to arise from the ion at m/z 1142 by sequential loss of two $(CF_2)_4CF_3$ chains. ^{1}H-NMR ($CDCl_3$, TMS/ppm): δ 7.80-7.97 (m, 4H), 7.48 (d, *J* = 3.6 Hz, 2H), 7.49-7.46 (m, 4H), 7.40 (d, *J* = 4.0 Hz, 2H), 7.26 (d, *J* = 4.0 Hz, 2H), 7.17 (d, *J* = 3.6 Hz, 2H). ^{19}F-NMR ($CDCl_3$, $CFCl_3$/ppm) δ -80.8 (m, 6F), -101.3 (m, 4F), -121.4 (m, 4F), -121.6 (m, 4F), -122.8 (m, 4F), -126.1 (m, 4F). ^{13}C-NMR ($CDCl_3$, TMS/ppm) δ 142.4, 139.8, 137.0, 131.3, 131.1, 130.7, 129.5, 126.5, 126.1, 125.4, 123.6. λ_{max} (CH_2Cl_2), 402 nm. λ_{em} (CH_2Cl_2), 487 nm.

9,10-Bis(5-bromothiophen-2-yl)anthracene, **62**.

Conventional bromination reaction.

Pale yellow solid (92% yield). M.p. 294 °C. MS (70 eV, EI): m/z 500 ($M^{\cdot+}$). ^{1}H-NMR ($CDCl_3$, TMS/ppm): δ 7.94-7.92 (m, 4H), 7.47-7.44 (m, 4H), 7.28 (d, *J* = 3.6 Hz, 2H), 6.97 (d, *J* = 3.6 Hz, 2H). ^{13}C-NMR ($CDCl_3$, TMS/ppm): δ 140.5, 131.3, 130.1, 130.0, 129.5, 126.4, 126.1, 113.1.

References

[1] a) M. M. M. Raposo, A. M. C. Fonseca and G. Kirsch, *Tetrahedron* **2004**, *60*, 4071-4078; b) A. Facchetti, M. Mushrush, H. E. Katz and T. J. Marks, *J. Adv. Mater.* **2003**, *15*, 33-38..
[2] K. Starcevic, D. W. Boykin and G. Karminski-Zamola, *Heteroatom Chemistry* **2003**, *14*, 218-222.
[3] P. Sonar, J. M. Zhuo, L.H. Zhao, K. M. Lim, J. Chen, A. J. Rondinone, S. P. Singh, L. L. Chua, P. K. H. Ho and A. Dodabalapur, *J. Mater, Chem.* **2012**, *22*, 17284-17292.
[4] S. Dufresne, M. Bourgeaux and W. G. Skene, *J. Mater. Chem.* **2007**, *17*, 1166.
[5] A. L. Johnson, *J. Org. Chem.* **1976**, *41*, 1320-1324.
[6] M. J. Mio, L. C. Kopel, J. B. Braun, T. L. Gadzikwa, K. L. Hull, R. G. Brisbois, C. J. Markworth and P. A. Grieco, *Org. Lett.* **2002**, *4*, 3199-3202.
[7] M. Melucci, M. Zambianchi, L. Favaretto, M. Gazzano, A. Zanelli, M. Monari, R. Capelli, S. Troisi, S. Toffanin and M. Muccini, *Chem. Commun.* **2011**, *47*, 11840-11842.

Chapter 6

List of publications

1. L. Maini, F. Gallino, M. Zambianchi, M. Durso, M. Gazzano, K. Rubini, D. Gentili, I. Manet, M. Muccini, S. Toffanin, M. Cavallini, M. Melucci, Chemical design enables the control of conformational polymorphism in functional 2,3-thieno(bis)imide-ended materials, *Chem. Commun.* **2015**, *51*, 2033-2035.

2. M. Zambianchi, L. Favaretto, M. Durso, C. Bettini, A. Zanelli, I. Manet, M. Gazzano, L. Maini, D. Gentili, S. Toffanin, F. Gallino, M. Muccini, M. Cavallini, M. Melucci, Synergic effect of unsaturated inner bridges and polymorphism for tuning the optoelectronic properties of 2,3-thieno(bis)imide based materials, *J. Mater. Chem. C* **2015**, *3*, 121-131.

3. M. Melucci, M. Durso, C. Bettini, M. Gazzano, L. Maini, S. Toffanin, S. Cavallini, M. Cavallini, D. Gentili, V. Biondo, G. Generali, F. Gallino, R. Capelli, M. Muccini, Structure–property relationships in multifunctional thieno(bis)imide-based semiconductors with different sized and shaped N-alkyl ends, *J. Mater. Chem. C* **2014**, *2*, 3448-3456.

4. M. Durso, M. Zambianchi, A. Zanelli, M. G. Lobello, F. De Angelis, S. Toffanin, S. Cavallini, D. Gentili, F. Tinti, M. Cavallini, N. Camaioni, M. Melucci, Synthesis by MW-assisted direct arylation, side-arms driven self-assembly and functional properties of 9,10-dithienylanthracene orthogonal materials, *Tetrahedron* **2014**, *70*, 6222-6228 (Special Issue on: Nanotek for organic synthesis, and organic synthesis for nanotek).

5. T. Posati, M. Melucci, V. Benfenati, M. Durso, M. Nocchetti, S. Cavallini, S. Toffanin, A. Sagnella, A. Pistone, M. Muccini, G. Ruani, R. Zamboni, Selective MW-assisted surface chemical tailoring of hydrotalcites for fluorescent and biocompatibile nanocomposites, *RSC Adv.* **2014**, *4*, 11840-11847.

6. M. Durso,C. Bettini, A. Zanelli, M. Gazzano, M. G. Lobello, F. De Angelis, V. Biondo, D. Gentili, R. Capelli, M. Cavallini, S. Toffanin, M. Muccini, M., Melucci, Synthesis, size-

dependent optoelectronic and charge transport properties of thieno(bis)imide end-substituted molecular semiconductors, *Org. Electron.* **2013**, *14*, 3089-3097.

7. D. Gentili, M. Durso, C. Bettini, I. Manet, M. Gazzano, R. Capelli, M. Muccini, M. Melucci, M. Cavallini, A time-temperature integrator based on fluorescent and polymorphic compounds, *Sci. Rep.* **2013**, 3 : 2581.

8. M. Durso, D. Gentili, C. Bettini, A. Zanelli, M. Cavallini, F. De Angelis, M. G. Lobello, V. Biondo, M. Muccini, R. Capelli, M. Melucci, π-Core tailoring for new high performance thieno(bis)imide based n-type molecular semiconductors, *Chem. Commun.* **2013**, *49*, 4298-4300.

9. M. Melucci, L. Favaretto, M. Zambianchi, M. Durso, M. Gazzano, A. Zanelli, M. Monari, M. G. Lobello, F. De Angelis, V. Biondo, G. Generali, S. Troisi, W. Koopman, S. Toffanin, R. Capelli, M. Muccini, Molecular tailoring of new thieno(bis)imide-based semiconductors for single layer ambipolar light emitting transistors, *Chem. Mater.* **2013**, *25*, 668-676.

10. M. Melucci, M. Durso, M. Zambianchi, E. Treossi, Z.-Y. Xia, I. Manet, G. Giambastiani, L. Ortolani, V. Morandi, F. De Angelis, V. Palermo, Graphene-organic hybrids as processable, tunable platforms for pH-dependent photoemission, obtained by a new modular approach, *J. Mater. Chem.* **2012**, *22*, 18237-18243.

11. M. Melucci, M. Durso, L. Favaretto, M. Capobianco, V. Benfenati, A. Sagnella, G. Ruani, M. Muccini, R. Zamboni, V. Fattori, N. Camaioni, Silk doped with a bio-modified dye as a viable platform for eco-friendly luminescent solar concentrators, *RSC Adv.* **2012**, *2*, 8610-8613.

Acknowledgments

I think I could never stop thanking my tutor at ISOF-CNR institute, dr. M. Melucci, who introduced me into the field of organic materials. I owe what I have learned just to her professional skills and to her deep love for research. Thank you for being my teacher showing your strong reliability and competence, and at the same time being a pleasant person with whom talking about science and everyday life.
A special thank to my research group of LAB 505: Laura & Max and (bazinga!) Cristian, for their expertise, their patience and their precious teachings, as well as for the good lab time spent together among chats, music and funny (!) experiments.
A thank to my PhD supervisor, prof. M. Bandini (UniBO), for his availability and kindness, to dr. R. Zamboni and dr. V. Palermo (ISOF-CNR), for their support and fruitful discussions, to E.T.C. S.r.l., 'ItalNanoNet' and 'Graphene Flagship' projects for funding.

To my parents, for everything: thanks mom, for your passion for science and for your taking care of people, and thanks dad, for your being a dreamer and for your teaching of living 'in direzione ostinata e contraria'.
A deep thank to my grandmothers, to Chiara (plus all her crew!) and Francesco, because they are with me every day in my life.

Thanks to Giulia and Matteo, because I won another sister and another brother. To my home friends, the 'Thursday Women', because they have a piece of me, forever. To the 7Fighters, because as we use to say, we didn't choose the team, the Team chose us.
Thanks to Karamoja and its people, because I always feel the warm of this land with me, alakara!

‘Once upon a time, when the world was just a pancake
Fears would arise, that if you went too far, you'd fall.
But with the passage of time, it all became more of a ball.
…Why would you play by the rules?’
-‘Dodo’, Dave Matthews-